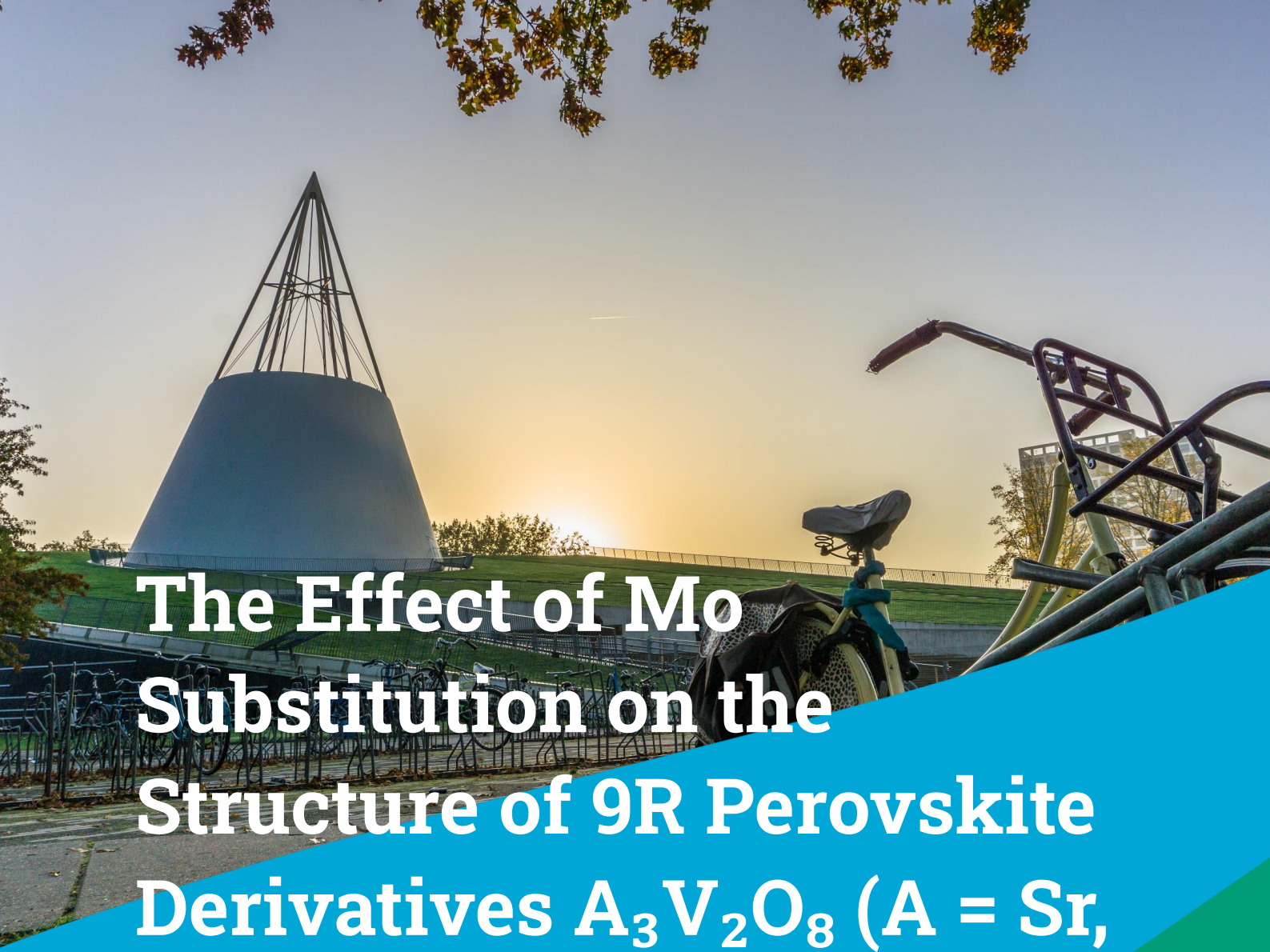

The Effect of Mo Substitution on the Structure of 9R Perovskite Derivatives $A_3V_2O_8$ (A = Sr, Ba)

Author: Hailin Ma
Date: 2025/8/19

TU Delft

The Effect of Mo-substitution on the Structure of 9R Perovskite Derivatives $A_3V_2O_8$ (A = Sr, Ba)

By

H. Ma

In partial fulfilment of the requirements for the degree of:

Master of Science
in Material Science and Engineering

at the Delft University of Technology,
to be defended publicly on [Tuesday August 19, 2025 at 13:30 PM.]

Supervisor:	Dr. Pedro B. Groszewicz	
	Dr. Yan Ma	
	Mr. Abdulkadir Olatunbosun Biffo	
Thesis committee:	Dr. A.J. Bottger,	TU Delft
	Dr. Pedro B. Groszewicz,	TU Delft
	Dr. Yan Ma,	TU Delft
	Mr. Abdulkadir Olatunbosun Biffo,	TU Delft

This thesis is confidential and cannot be made public until December 31, 2025.

An electronic version of this thesis is available at http://repository.tudelft.nl/.

Contents

Abstract **5**

1 Introduction **6**
1.1 Solid Oxide Fuel Cells (SOFCs) 6
1.2 Research of Perovskites for SOFCs 8
1.2.1 Perovskites 8
1.2.2 Research of Perovskites for SOFCs 9

2 Theory **12**
2.1 Crystal Structure 12
2.2 X-ray Diffraction (XRD) and Neutron Diffraction (ND) 15
2.3 Inductively coupled plasma-Mass Spectrometry (ICP-MS) 16

3 Experiment **17**
3.1 Solid-State Synthesis 17
3.2 Diffraction and Refinement 20
3.3 Fabrication of Pellets 21

4 Results and Discussion **24**
4.1 Solid-State Synthesis 24
4.1.1 Reproduction of Fop’s Work 24
4.1.2 Molybdenum substitution 26
4.2 Refinement Results 33
4.2.1 Le Bail Refinement 34
4.2.2 Rietveld Refinement 37
4.3 Fabrication of the pellets 47

5 Conclusion **52**

6 Outlook **53**

Acknowledgments **55**

Bibliography **56**

Appendix A **62**

Appendix B **76**

Abstract

The structural effects of substituting Mo^{6+} for V^{5+} in palmierite-type $A_3V_2O_8$ (A = Sr, Ba), a derivative of the 9R hexagonal perovskite, were systematically investigated. Polycrystalline samples with varying Mo contents (x = 0–0.2 for Sr series; x = 0–0.3 for Ba series) were synthesized via solid-state reaction and characterized using X-ray diffraction (XRD), neutron powder diffraction (NPD), and inductively coupled plasma mass spectrometry (ICP-MS). Refinement analysis shows that introducing Mo into the lattice slightly enlarges the a-axis while compressing the c-axis. Such changes can be understood from several factors: the size difference between Mo^{6+} and V^{5+} ions, the extra oxygen atoms brought in by substitution, and the influence of stronger Mo–O bonds on the surrounding structure. NPD analysis indicates average distortions, including partial replacement of VO_4 tetrahedra to MoO_6 octahedra, and secondary B-site occupation in Ba-based compounds at higher substitution levels. High-temperature NPD further demonstrates tetrahedral coordination favored upon heating. The results suggest that Mo substitution is able to tune lattice parameters and average transition metal cation coordination environments in palmierite-type oxides, offering pathways to optimize ionic conductivity for solid oxide fuel cell applications.

1 Introduction

1.1 Solid Oxide Fuel Cells (SOFCs)

As the global energy structure transforms towards cleaner and lower-carbon energy, solid oxide fuel cells (SOFCs) are becoming a shining pearl in fuel cell technology due to their high efficiency, low emissions, and wide fuel adaptability. The SOFC power generation system is centered on the battery stack, which can efficiently convert the chemical energy of the fuel directly into electrical energy. It is widely used in portable power supplies, household combined heat and power (CHP), automotive auxiliary power units (APU), range extenders, distributed power generation, and fixed power stations [1; 2; 3]. SOFCs are recognized as third-generation batteries, holding immense developmental potential [4; 5]. It is a device that converts the chemical energy of fuel directly into electrical energy through electrochemical reactions. Unlike other types of fuel cells, SOFC does not rely on precious metal catalysts to promote electrochemical reactions, which reduces dependence on rare metals to a certain extent and also reduces costs. Its principle and structure are shown in Figure 1.

Its principle looks more like a "reverse engineering" of water electrolysis: during water electrolysis, water is decomposed into hydrogen and oxygen; while in SOFC, fuel oxidation reaction occurs at the anode, oxidant reduction reaction occurs at the cathode, and ions are conducted through the electrolyte to generate electrical energy and heat energy [1; 6]. Specifically, the fuel (such as hydrogen) is oxidized at the anode, releasing electrons and protons (or ions); oxygen is reduced to oxygen ions at the cathode, and the oxygen ions migrate to the anode through the solid oxide electrolyte, reacting with the fuel to generate water or other products, while electrons flow through the external circuit to form an electric current to achieve electrical energy output [7].

The single cell structure of SOFC consists of three parts. The anode is where fuel oxidation occurs, so it must maintain good catalytic activity to effectively promote the oxidation process of the fuel. At the same time, as an electrode, it must have high ion/electron conductivity to ensure the smooth transmission of the two. In addition, since hydrocarbon fuel is one of the main fuels for humans at present, anti-carbon deposition is also a necessary property of anode materials. Common anode materials include Ni/YSZ metal ceramics and perovskite materials [8; 9]. To achieve efficient oxygen reduction reaction (ORR), the cathode material needs to have high oxygen reduction activity [10]. Common anode materials include perovskite structures (such as LSCF, i.e. $La_{0.6}Sr_{0.4}Co_{0.2}Fe_{0.8}O_3$) and double perovskites [11; 12]. These materials have special crystal structures and electronic properties, which can effectively promote the adsorption, dissociation and reduction processes of oxygen; solid oxide electrolyte is one of the core components of SOFC, and its main function is to conduct ions while isolating electrons. The electrolyte needs to have high ionic conductivity to ensure that ions can pass quickly and reduce the internal resistance of the battery; at the same time, it must have low electronic conductivity to prevent electron leakage and ensure the normal electrochemical reaction [13; 14; 15]. In addition, the electrolyte also needs to have good high-temperature oxidation resistance and be able to operate stably for a long time in a high-temperature environment due to the working temperature of SOFCs (800℃- 1000℃) [16; 17]. Common electrolyte materials include yttria-stabilized zirconia (YSZ) and CeO_2-based materials [18; 19]. Meanwhile, the complete SOFC system also has a set of auxiliary systems,

such as a fuel supply system and a gas supply system, which deliver fuel to the anode and oxygen to the cathode respectively; the control system is used for voltage regulation and inverter, etc.

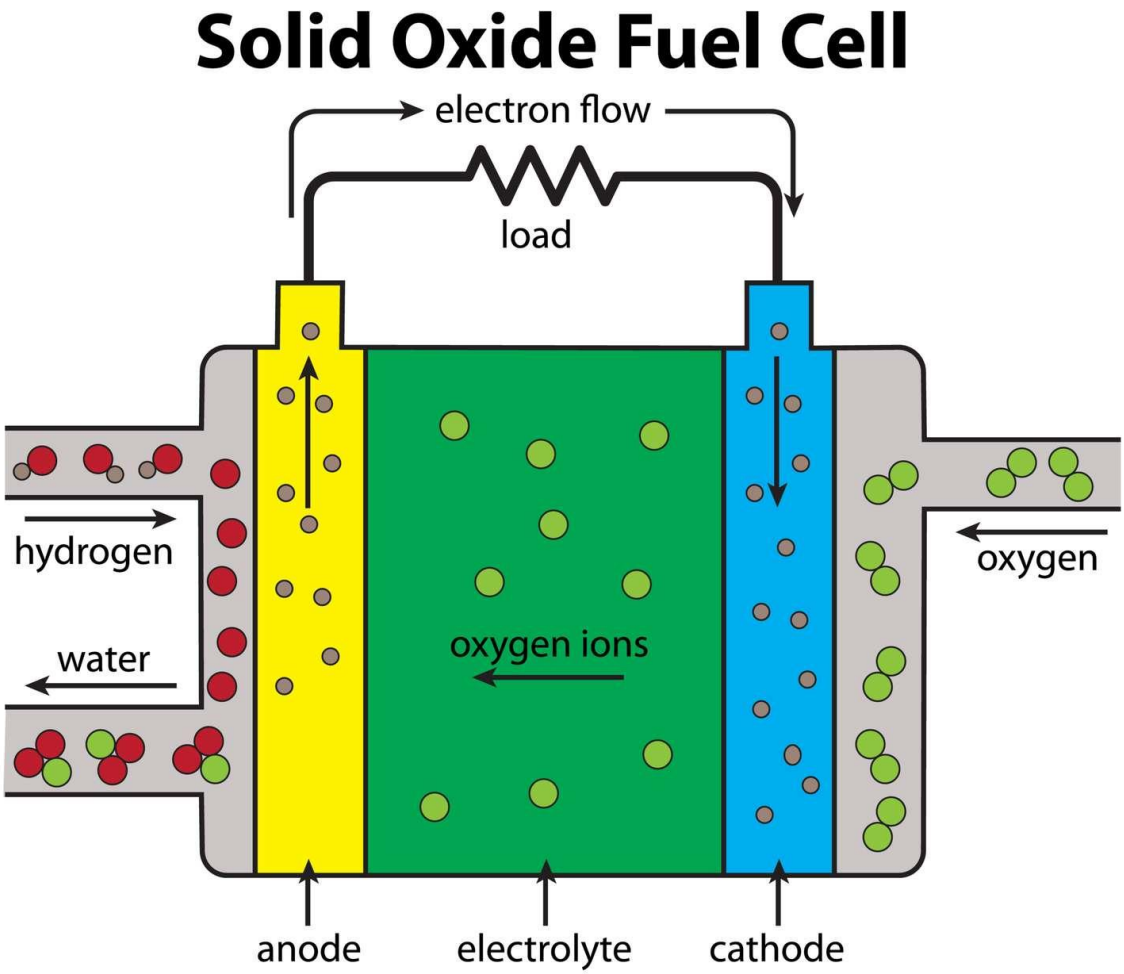

Figure 1 Diagram of a typical SOFC [20].

SOFCs have many advantages, making them gradually popular. It is an electrochemical conversion equipment that skips the combustion and mechanical processes of the traditional power generation mode and directly converts the fuel into electrical energy, significantly improving the energy conversion efficiency with high energy conversion efficiency, which can reach about 60%, this number can be even extended to 85% with CHP [2; 21]. However, developing and optimizing their material availability presents significant challenges in materials engineering. Unlike other fuel cell types, SOFCs do not rely on precious metal catalysts to drive electrochemical reactions, reducing dependence on rare metals and lowering costs. SOFC has several key benefits for energy storage. First, it can use many different fuels. These include hydrogen, natural gas, biogas, and hydrocarbons [22]. Due to their high operating temperatures, SOFCs generate high-grade waste heat during power generation, making them suitable for combined heat and power applications [23]. The high operating temperatures of the SOFC system accelerate the chemical reactions inside, which means the fuel cells produce electricity more efficiently. The high heat also means many fuels can be used directly without special treatment. However, high operating temperatures

also present challenges, such as stringent material requirements for thermal stability and the need to optimize material stability and durability under such conditions [24].

1.2 Research of Perovskites for SOFCs

1.2.1 Perovskites

The term "perovskite" originally referred to the natural mineral calcium titanate ($CaTiO_3$) discovered in 1839 and named after mineralogist Lev Perovski. Today, this term has evolved to encompass a broad category of materials with ABX_3 crystal structures and their derivatives [25]. The ideal perovskite exhibits cubic symmetry with space group Pm-3m. This cubic perovskite structure can be viewed as a framework composed of BO_6 octahedra connected through shared vertices, with A ions filling the interstitial spaces between eight BO_6 octahedra. Alternatively, when the A ion radius is sufficiently large to support the entire cubic perovskite framework, the structure can also be described as BO_6 octahedra occupying the interstitial spaces within a cubic framework formed by A ions. It is generally believed that the BO_6 octahedra form the skeletal structure of cubic perovskites, and their stability determines the overall stability of the perovskite structure [26; 27; 28].

The tolerance factor determines the structural stability of perovskite materials. The tolerance factor was first proposed by Goldschmidt in 1926 and is defined as:

$$t = \frac{r_A + r_X}{\sqrt{2}(r_B + r_X)} \qquad (1)$$

where r_A represents the radius of the A-site ion, r_X represents the radius of the X-site ion, and r_B represents the radius of the B-site ion. Different ranges of the tolerance factor correspond to different unit cell structures [29].

Perovskite has become a focus of attention in the field of materials research in recent years [30; 31]. The broad appeal of perovskites in diverse research areas stems mainly from three key attributes. First, their bandgap can be precisely tuned by varying the halide composition—for example, by mixing iodine and bromine—allowing absorption across the visible and near-infrared regions [32; 33]. Iodine-based perovskites such as $MAPbI_3$ exhibit a bandgap of about 1.5 eV, which is close to the ideal value for solar energy harvesting. The hybridization of lead's $6s^2$ orbitals with halide p orbitals further enhances light absorption efficiency [34]. Consequently, perovskite films can achieve strong light absorption with thicknesses of only a few hundred nanometers, much thinner than conventional silicon-based absorbers. Second, unlike many semiconductors in which electron and hole mobilities differ substantially, perovskites display an unusually balanced charge transport. Their continuous network of BO_6 octahedra forms efficient pathways for rapid carrier migration, while defect states are mostly shallow and unlikely to trap carriers significantly [35; 36; 37]. This property is critical for photovoltaic devices, as it facilitates efficient charge separation and reduces recombination losses, ultimately improving power conversion efficiency [38; 39; 40]. Third, perovskites demonstrate remarkable defect tolerance compared to traditional semiconductors like silicon, which are highly sensitive to lattice imperfections. In perovskites, defect energy levels typically lie close to the valence band maximum or conduction band minimum [39; 41], enabling trapped carriers to escape via thermal activation. This minimizes performance degradation and relaxes the precision required for material processing, making large-scale, low-cost production more achievable.

1.2.2 Research of Perovskites for SOFCs

For SOFCs, the latter two characteristics undoubtedly make perovskite and its derivative materials ideal materials for making SOFCs electrodes [42]. More specifically, as an electrode material for SOFCs, perovskite materials provide three characteristics that make them promising for use in SOFCs. First, the excellent defect tolerance of perovskite makes its structure have high oxygen vacancy adjustability. Through reasonable A-site or B-site metal ion substitution, the generation and migration rate of oxygen vacancies can be effectively improved, thereby significantly enhancing the ion conductivity of the electrode [43]. The second point is that this defect tolerance also brings excellent structural and chemical stability to perovskite materials and their derivatives. The working environment of SOFCs requires extremely high temperatures (800-1000℃). The BO_6 octahedral skeleton in the perovskite structure takes into account both rigidity and flexibility, which can effectively ensure the long-term stable operation of the battery without significant phase change or structural degradation [44]. This structural flexibility can also form a continuous three-dimensional oxygen ion migration channel inside the perovskite material, thereby increasing the diffusion rate of oxygen ions in the lattice [45]. Research on optimizing the conductivity of perovskites has made great progress. Many researchers have proposed different solutions for oxygen ions, protons and electrons. Among them, metal ion substitution at the A and B sites is the most common [46].

Yashima *et al.* investigated the potential of $Ba_7Nb_4MoO_{20}$-based hexagonal perovskite-related oxides as high-performance oxide ion conductors, focusing on their conductivity, structural features, and ion transport mechanisms [47]. By tuning the Mo/Nb ratio and introducing interstitial oxygen, two compounds—$Ba_7Nb_{3.9}Mo_{1.1}O_{20.05}$ (BNM1.1) and $Ba_7Nb_{3.95}Mo_{1.05}O_{20.025}$ (BNM1.05)—were synthesized via solid-state reaction, with BNM1.1 exhibiting higher ionic conductivity. Neutron diffraction (ND) and maximum entropy method (MEM) analyses revealed partially occupied interstitial oxygen sites (O5) in BNM1.1, as shown in Figure 2 located within the oxygen-deficient c′ layers. Oxide ions diffuse within the *ab* plane via a two-dimensional pathway involving lattice oxygen sites (O1) and interstitial sites (O5), forming a (tetrahedral O1)–(octahedral O5) interstitial diffusion mechanism. The high conductivity of BNM1.1 is attributed to its unique structure, which enables oxide ions to migrate preferentially within the *ab* plane, where the activation energy is much lower (0.19 eV) than along the *c*-axis (1.54 eV), confirming a two-dimensional diffusion mechanism. Furthermore, XRD analysis demonstrated that the structure remains stable under operating conditions, providing important guidance for developing next-generation oxide ion conductors.

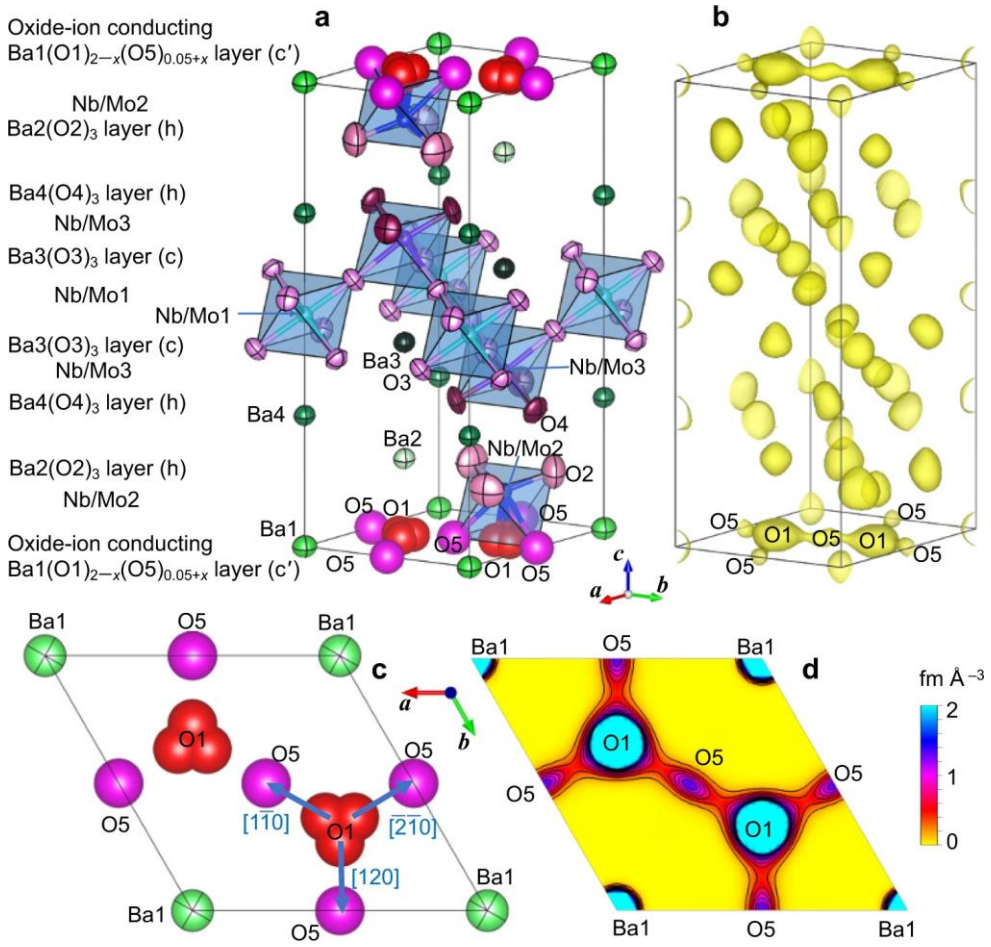

Figure 2. Refined Crystal Structure and MEM NSLD Analysis of $Ba_7Nb_{3.9}Mo_{1.1}O_{20.05}$ at 800 °C: (a) 3D Structure with Thermal Ellipsoids (90% Probability), (b) Yellow Isosurface of MEM NSLDs (0.36 fm Å⁻³), (c) ab-Plane Projection (z = 0), and (d) Contour Map of NSLD Distribution (0–2 fm Å⁻³, Step 0.2 fm Å⁻³). Arrows in (c) Indicate O1→O5 Oxide-Ion Migration Paths [47].

Andreev *et al.* investigated a series of hexagonal perovskite-type proton conductors, $Ba_7In_{6-x}Y_xAl_2O_{19}$ ($0 \leq x \leq 0.25$), to elucidate the relationship between their hydration behavior and structural as well as chemical properties [48]. The study focused on how yttrium substitution affects hydration capacity and thermodynamic characteristics and sought to establish correlations between crystal structure, basicity, and hydration enthalpy. Dehydration behavior was studied using thermogravimetric analysis coupled with mass spectrometry (TG-MS). Hydration enthalpy (ΔH_{hydr}) was derived by fitting the TG data. A defect chemistry model was constructed based on the TG curves and fitted using the hydration equilibrium constant equation (K_{hydr}) to extract the samples' standard hydration enthalpies ($\Delta H°_{hydr}$). The results showed that $\Delta H°_{hydr}$ decreased linearly from −56 kJ/mol for x = 0 to −110 kJ/mol for x = 0.25. This enhanced exothermicity was attributed to increased ionicity of the M–O bonds induced by Y substitution, which raised the electron density on oxygen and thus improved the material's hydrophilicity. These findings support Kreuer's theory linking oxygen electron density, hydrophilicity, and hydration enthalpy and provide insight into designing improved proton-conducting materials through structural and electronic tuning.

As mentioned above, in order to achieve high oxygen ion conductivity (~0.1S/cm), the operating temperature of SOFCs often needs to reach high temperatures to ensure sufficient oxygen vacancy concentration and migration rate [49]. However, the disadvantages of high temperature are also obvious: heating requires a lot of energy consumption and startup time; the use of high temperature and corrosion-resistant materials leads to high costs; high temperature causes reduced electrode life: such as Ni-YSZ anode is prone to carbon deposition, and Sr migration/phase change occurs at the cathode. Therefore, researchers hope to reduce the operating temperature of SOFC from the traditional 800-1000 °C to 500-700 °C (called IT-SOFC, medium-temperature SOFC), or even lower (LT-SOFC, low-temperature SOFC), to alleviate the above problems [50]. Fop et al. investigated the coexistence of proton and oxide ion conductivity in palmierite-type oxides $A_3V_2O_8$ (A = Sr, Ba), expanding the scope of ionic conductor research beyond conventional octahedral-based structures [51]. AC impedance spectroscopy showed that $Sr_3V_2O_8$ exhibits a proton conductivity of 1.0×10^{-4} S/cm at 600 °C under humid air, while $Ba_3V_2O_8$ achieves approximately 1.6×10^{-6} S/cm. The use of D_2O confirmed the proton conduction mechanism. Proton transport number (t_h) analysis indicated that proton conduction dominates under humidified conditions, with values ranging from 0.6 to 0.8 for both materials. $A_3V_2O_8$ represents the first palmierite-type oxide to simultaneously exhibit proton and oxide ion conduction without substitution, with $Sr_3V_2O_8$ showing auspicious performance. In this study, we will adopt the method of B-site metal ion substitution to try to explore the effect of B-site Mo substitution on the conductivity of $A_3V_2O_8$ materials.

2 Theory

In this article, the various theoretical foundations used to support this research will be introduced, including the crystal structure of $A_3V_2O_8$, and the various techniques used to characterize its composition, structure, and conductivity.

2.1 Crystal Structure

The perovskites can be generally divided into two types， cubic and hexagonal [52]. Cubic perovskites usually form into the Pm-3m space group, which is the most ideal structure of perovskites. $SrTiO_3$, $BaZrO_3$, and $LaMnO_3$ are widely studied cubic perovskite materials, which have shown exemplary performance in the fields of ferroelectricity, proton conduction, and electrocatalysis, respectively [53]. Figure 3 presents the crystal structure of $Sr(Mo,Ga)O_{3-\delta}$ refined in the cubic space group *Pm*-3*m* (No. 221), with one formula unit per unit cell (Z = 1). In this structure, Sr atoms occupy the 1b Wyckoff position at coordinates (½, ½, ½), while Mo and Ga atoms are randomly distributed over the 1a site at (0, 0, 0). Oxygen atoms are at the 3d sites with fractional coordinates (½, 0, 0) [54]. The hexagonal structure is generally formed when the A-site cation is excessively large or the B-site cation is relatively small, causing the Goldschmidt tolerance factor to typically drop below 0.8 or exceed 1 [55; 56]. Such a structure often appears as a phase transformation product under high-temperature or high-pressure conditions. In this situation, the conventional arrangement of BO_6 octahedra in the cubic structure is hindered, promoting the formation of the hexagonal perovskite phase. Its most distinctive feature is that part of the BO_6 octahedra are arranged in a face-sharing manner along the c-axis, forming chain-like or columnar structures that result in pronounced crystallographic anisotropy [57; 58]. This anisotropy significantly influences the physical properties of the material, especially ion migration behavior, which shows strong directionality. For example, in typical oxygen ion or proton conductors such as $Ba_5In_2Al_2ZrO_{13}$, ion diffusion predominantly occurs along specific crystallographic directions, exhibiting excellent directional conductivity [59; 60]. In addition, the face-sharing chains easily form layered structural units, which are conducive to rapid one-dimensional ion migration.

However, compared with the cubic perovskite structure, the hexagonal phase is often thermodynamically less stable, mainly due to stress concentration and lattice distortion introduced by the face-sharing arrangement [61]. Nevertheless, this structural diversity provides a broader space for the design of functional materials. Many hexagonal perovskite-type materials, such as $Ba_5In_2Al_2ZrO_{13}$ and $YMnO_3$, have been extensively studied and applied in cutting-edge fields including ion conduction, nonlinear optics, and magnetoelectric coupling, demonstrating great potential for multifunctional integration [62; 63].

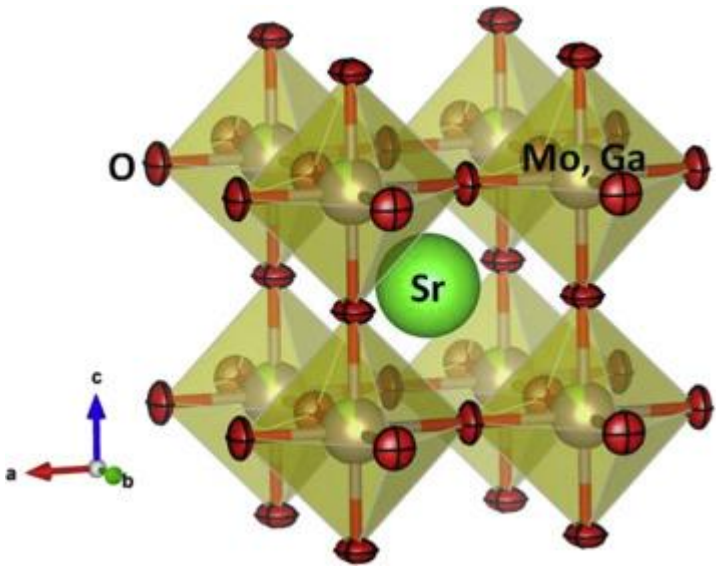

Figure 3. Cubic perovskite unit cell of Sr(Mo,Ga)O3-d [54].

Figure 4 illustrates a schematic comparison of the 9R hexagonal perovskite and its derivative, the palmierite structure. The 9R perovskite ($A_3B_3O_9$) generally follows the stoichiometry of the typical perovskite formula ABX_3 and is a representative example of a perovskite structure. It belongs to the hexagonal perovskite family, typically formed by repeating ABO_3 layers stacked along the c-axis. The stacking sequence can be described as $(hhc)_3$, where h denotes a hexagonal AO_3 layer and c stands for a cubically packed AO_3 layer. In an ideal 9R hexagonal perovskite, the BO_6 octahedra are corner-sharing, forming a continuous three-dimensional octahedral framework. This continuous network is a key feature of many perovskite-type oxide ion conductors (such as $LaGaO_3$ and $BaZrO_3$), where ionic transport typically relies on the migration of oxygen vacancies within and between the octahedral units [64; 65].

The palmierite structure ($A_3B_2O_8$) can be regarded as a cation- and oxygen-deficient derivative of the 9R hexagonal perovskite. Its main difference from the 9R perovskites is that the oxygen ions in the cubically packed AO_3 layer are partially removed, converting it into an AO_2 layer, which is denoted as a c' layer. This oxygen deficiency has a significant structural impact: it introduces ordered octahedral vacancies into the framework, disrupting the continuous BO_6 network and resulting in isolated BO_4 tetrahedra, such as VO_4. In other words, the palmierite structure can be seen as a special derivative of the 9R polytype generated through ordered defect engineering. In this derivative, the octahedral sites within the central metal triplets are often unoccupied, creating regularly arranged voids along the interlayer direction and forming isolated tetrahedral units.

According to the experimental results and Rietveld/ND refinements by Fop et al., $A_3V_2O_8$ crystallizes in the R-3m space group [51]. The A-site cations are distributed over two Wyckoff positions: 3a (A1) and 6c (A2). The V atoms exclusively occupy the Wyckoff 6c sites, forming isolated VO_4 tetrahedra, while the oxygen atoms are located at the 6c (O1) and 18h (O2) positions.

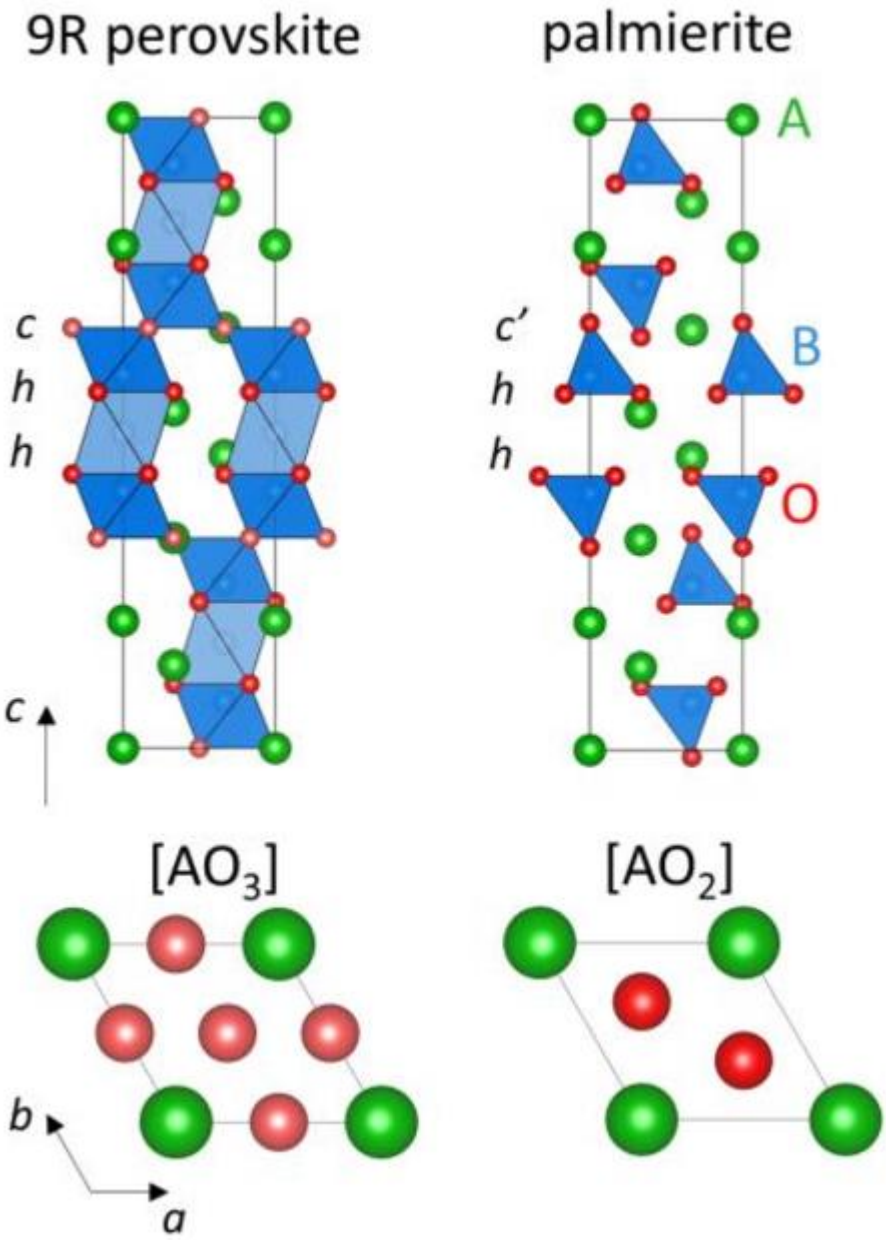

Figure 4. Comparison between the 9R hexagonal perovskite and palmierite structures[51].

Unlike the 9R perovskite, the palmierite structure features VO_4 tetrahedra with significant rotational freedom, which is essential for both proton and oxide ion migration. Fop et al. demonstrated through AIMD simulations that oxide ions migrate via the rotation of VO_4 units, forming transient V_2O_7 dimers that enable oxygen to hop between sites (O1–O1, O1–O2, O2–O2). The preferred proton sites were identified using BVSE calculations and DFT, which showed that protons tend to reside near the apical O1 positions and can form a two-dimensional or even three-dimensional exchange network within the ab plane. Compared with conventional octahedral-based conductors, this mechanism highlights the unique multidimensional transport potential of materials based on isolated tetrahedral units.

2.2 X-ray Diffraction (XRD) and Neutron Diffraction (ND)

To analyze the crystal structure of the synthesized materials, X-ray diffraction (XRD) is undoubtedly the most fundamental and widely used characterization technique. When incident X-rays interact with the regularly arranged atomic planes in a crystal, they are elastically scattered by the electron clouds surrounding the atomic nucleus. Constructive interference occurs when the reflected X-rays from adjacent planes satisfy the condition described by Bragg's Law:

$$n\lambda = 2dsin\theta \quad (2)$$

where n is the diffraction order (integer), λ is the X-ray wavelength, d is the interplanar spacing, and θ is the Bragg angle. By measuring the 2θ positions and relative intensities of the diffraction peaks in the sample's pattern, the interplanar spacings and lattice parameters can be accurately calculated, which in turn makes it possible to deduce the crystal symmetry, space group, and atomic arrangement within the unit cell. Furthermore, the number, position, and intensity distribution of the diffraction peaks can be used to identify the types of phases present, their relative amounts, and whether any impurity or amorphous phases exist. Modern powder XRD experiments typically employ monochromatic Cu Kα radiation (wavelength ≈ 1.54 Å), and the resulting diffraction pattern provides the essential data basis for phase analysis, determination of lattice parameters, and subsequent Le Bail and Rietveld refinements.

After acquiring the XRD patterns, the data are refined sequentially using the Le Bail and Rietveld methods. The primary purpose of the Le Bail method is to confirm the lattice parameters of the sample. A key feature and limitation of this method is that the fitting does not consider the specific atomic positions or occupancies; thus, at this stage, the peak intensities are used only for fitting the peak shapes. The working principle is to adjust the unit cell parameters, zero-point error, and peak shape and width parameters to achieve the best fit to the experimental pattern. As a starting point, a specific instruction file and a .cif file containing the space group information of a known, similar compound are provided to the software to prevent ineffective searching. Then, full-pattern profile fitting is performed to resolve overlapping peaks, and a least-squares method is used iteratively to optimize the fit until the calculated peaks align with the experimental ones and the fitting converges. Because the structure factor is not considered in this stage, the calculated peak intensities may deviate from the true values. The main parameters refined at this stage include the instrumental parameters (which determine the peak width, asymmetry, and the position) and the unit cell parameters (which determine the peak positions).

After that, the Rietveld method is applied for further refinement. It is performed based on the lattice parameters and space group determined by the Le Bail fitting. The Rietveld method refines the detailed atomic positions, occupancies, and isotropic atomic displacement parameters within the unit cell. This method also employs full pattern fitting by comparing the theoretical model, which includes atomic coordinates and occupancies, with the experimental XRD pattern. During refinement, a Hessian matrix is automatically calculated and converted into a covariance matrix to indicate any strong correlations between refined parameters, which helps optimize the refinement constraints. The main parameters refined in this step include the overall histogram factor (which determines the intensity of the fitted peaks), the atomic positions, occupancies, and the isotropic displacement parameters.

In addition to XRD, neutron diffraction (ND) is also an important part of the structural analysis.

One similarity with XRD is that neutron diffraction (ND) also obeys Bragg's Law, which describes the condition for constructive interference between incident beams and the regularly arranged atomic planes in a crystal. However, the fundamental difference is that the incident particles in ND are neutrons, which interact directly with the atomic nuclei rather than with the electron clouds surrounding them. As a result, the scattering sensitivity of neutrons does not show a simple linear relationship with atomic number but instead depends on the nuclear scattering length of each element. In addition, ND allows measurements to be performed at different temperatures, which is particularly important for investigating the crystal structure of materials under high-temperature conditions. Here we use ND to supplement to the research of crystal structure, because XRD mainly relies on the interaction between X-rays and electron clouds, making it more sensitive to heavier elements in the structure (such as Sr and Ba), but less effective for probing the distribution of light elements such as oxygen. In contrast, ND probes atomic distributions through the interaction between neutrons and atomic nuclei, which allows us to more effectively identify oxygen vacancies as well as ordered or disordered oxygen arrangements, thus a more comprehensive understanding of the sample structure can be provided. Therefore, ND was employed for additional measurements.

2.3 Inductively coupled plasma-Mass Spectrometry (ICP-MS)

Inductively Coupled Plasma Mass Spectrometry (ICP-MS) is a highly sensitive and high-resolution elemental analysis technique that is mainly used for quantitative and qualitative determination of multiple elements in samples at trace (ppb level) to ultra-trace (ppt level) concentrations. Its principle is to use a high-temperature plasma (typically an argon plasma) to atomize and ionize the elements in the sample, after which the resulting ions are separated and detected according to their mass-to-charge ratio (m/z) by a mass spectrometer. Solid samples are first dissolved and then nebulized into fine droplets by a nebulizer, which are carried by a carrier gas (usually argon) into the plasma torch. Argon gas is partially ionized at high temperatures (6,000–10,000 K) to form a high-temperature plasma, which is sustained by a high-frequency alternating electromagnetic field generated by a radio frequency (RF) generator through a coil wound around the outside of a quartz torch. This provides sufficient energy for the atomization and ionization of the sample. The liquid droplets are rapidly vaporized in the plasma to form dry particles, which are then further broken down into atoms and ionized into positive ions in the high-temperature environment. At the end of the torch, the resulting ion stream passes through a sampler cone and a skimmer cone into a low-pressure mass spectrometer chamber, where the ion beam is focused and accelerated by an ion lens system, while most neutral particles and excess gas are removed. The focused ions then enter the mass analyzer, which is typically a time-of-flight (TOF) analyzer. There, the ions are separated according to their mass-to-charge ratio (m/z), pass sequentially into the detector (such as an ion multiplier), and are counted or converted into electrical signals. Finally, the data system outputs the relative abundance and concentration of each element or isotope in the sample.

3 Experiment

This chapter will introduce the experimental steps of the entire research, including the solid-state synthesis of the material, its structural analysis (including XRD, ND), and its conductivity test (EIS)

3.1 Solid-State Synthesis

In general, the solid-state synthesis of materials can be divided into two parts: for $A_3V_2O_8$, that is, the reproduction of the research results of Fop et al., and the synthesis of new substituted powders. This study uses Mo to substitute $A_3V_2O_8$ to generate two series: $Sr_3V_2Mo_xO_{8+x/2}$ and $Ba_3V_2Mo_xO_{8+x/2}$.

Figure 5. Process of Solid-State Reaction for Perovskite Materials [66].

The first step is the calcination of $Sr_3V_2O_8$ and $Ba_3V_2O_8$. The synthesis method is based on the work of Fop et al. The whole synthesis steps are shown in Figure 5. The fabrication of the pellets will be discussed in section 3.3 since we need the refinement of the powders to identify the chemicals that have been calcinated. These two materials are marked as H001 and H002 respectively. The calcination procedure for both samples is essentially the same; $Sr_3V_2O_8$ is described here as an example. To synthesize 2 g of $Sr_3V_2O_8$, the corresponding amounts of strontium carbonate powder ($SrCO_3$) and vanadium pentoxide powder (V_2O_5) were weighed out and placed in a mortar, then thoroughly mixed using a pestle. The masses of the required precursors are listed in Table 1. Next, the uniformly mixed powder was placed into a 10 mm diameter mold and pressed into a cylindrical pellet under a pressure of 1000–1200 lbs. using a hydraulic press. The pellet was then placed in a reaction dish and transferred to a furnace shown in Figure 6. During calcination, the crucibles were stacked as shown in Figure 6 to take advantage of the fact that the temperature field near the center of the furnace chamber was usually the most stable and uniform. This vertical arrangement allows multiple samples to be positioned closer to the central axis, thereby improving temperature control consistency and ensuring reproducibility and comparability of the calcination results. The sample was heated from room temperature to

1100 °C with the rate of 150 °C per hour and was held at this temperature for 10 hours. Then it was cooled to room temperature at a rate of 300 °C per hour. The reaction of the precursors at high temperature is shown in Formula:

$$3SrCO_3 + V_2O_5 \rightarrow Sr_3V_2O_8 + 3CO_2 \quad (3)$$

	Principle Required Mass(g)	Actual Mass(g)
$SrCO_3$	1.7977	1.7987
V_2O_5	0.7382	0.7390

Table 1. Mass of Precursors for H001($Sr_3V_2O_8$)

For $Ba_3V_2O_8$, the $SrCO_3$ was replaced by barium carbonate ($BaCO_3$), and its reaction is shown in Formula:

$$3BaCO_3 + V_2O_5 \rightarrow Ba_3V_2O_8 + 3CO_2 \quad (4)$$

	Principle Required Mass(g)	Actual Mass(g)
$BaCO_3$	1.8447	1.8447
V_2O_5	0.5667	0.5672

Table 2. Mass of Precursors for H002($Ba_3V_2O_8$)

Figure 6. Set up for The Calcination

After the first calcination of H001 and H002 was completed and XRD analysis was carried out, it was confirmed that H002 ($Ba_3V_2O_8$) had been successfully synthesized, whereas H001 still contained some side phases. The specific testing procedures and results will be presented in the later section. Subsequently, H001 underwent a second calcination under the same conditions, and the XRD results confirmed that $Sr_3V_2O_8$ had been successfully synthesized. For these two samples, Mo substitution was carried out in two series: $Sr_3V_{2-x}Mo_xO_{8+x/2}$ and $Ba_3V_{2-x}Mo_xO_{8+x/2}$. For each series, four samples were prepared with different substitution levels (x = 0.1, 0.2, 0.3, 0.4), as shown in Table 3. In addition to the strontium/barium carbonate and V_2O_5 mentioned earlier, Mo substitution was achieved by adding molybdenum trioxide (MoO_3) as a precursor during the calcination step. The sample designations and the required masses of precursors are listed in Table 4.

$Sr_3V_{2-x}Mo_xO_{8+x/2}$		$Ba_3V_{2-x}Mo_xO_{8+x/2}$	
Sample number	**Expected chemical**	**Sample number**	**Expected chemical**
H003	$Sr_3V_{1.9}Mo_{0.1}O_{8.05}$	**H009**	$Ba_3V_{1.9}Mo_{0.1}O_{8.05}$
H004	$Sr_3V_{1.8}Mo_{0.2}O_{8.1}$	**H010**	$Ba_3V_{1.8}Mo_{0.2}O_{8.1}$
H005	$Sr_3V_{1.7}Mo_{0.3}O_{8.15}$	**H011**	$Ba_3V_{1.7}Mo_{0.3}O_{8.15}$
H006	$Sr_3V_{1.6}Mo_{0.4}O_{8.2}$	**H012**	$Ba_3V_{1.6}Mo_{0.4}O_{8.2}$

Table 3. Name of the Samples and Their Corresponding Chemicals

	Principle Required Mass(g)				Actual Mass(g)			
	H003	H004	H005	H006	H003	H004	H005	H006
$SrCO_3$	1.7785	1.7598	1.7416	1.7235	1.7788	1.7597	1.7416	1.7234
V_2O_5	0.6939	0.6504	0.6079	0.5662	0.6939	0.6504	0.6080	0.5661
MoO_3	0.0578	0.1144	0.1698	0.2241	0.0579	0.1144	0.1689	0.2242

Table 4(1). Mass of Precursors for $Sr_3V_2Mo_xO_{8+x/2}$

	Principle Required Mass(g)				Actual Mass(g)			
	H009	H0010	H0011	H0012	H009	H010	H011	H012
$BaCO_3$	1.8296	1.8147	1.8001	1.7857	1.8296	1.8147	1.8001	1.7856
V_2O_5	0.5340	0.5018	0.4701	0.4389	0.5340	0.5018	0.4701	0.4387
MoO_3	0.0445	0.0882	0.1311	0.1737	0.0444	0.0883	0.1313	0.1737

Table 4(1). Mass of Precursors for $Ba_3V_2Mo_xO_{8+x/2}$

The reactions of these 2 series are shown in formula 5 and 6 respectively:

$$3SrCO_3 + V_2O_5 + xMoO_3 \rightarrow Sr_3V_{2-x}Mo_xO_{8+x/2} + 3CO_2 \quad (5)$$

$$3BaCO_3 + V_2O_5 + xMoO_3 \rightarrow Ba_3V_{2-x}Mo_xO_{8+x/2} + 3CO_2 \quad (6)$$

It should be noted that the missing sample numbers are not named sequentially, because H007 and H008 are chemically identical to H003 and H004 in terms of the intended synthesized phases. They were prepared separately to verify whether drying the precursors at 200 °C for one hour would affect the purity of the target samples. The comparative results will be presented in the next section.

3.2 Diffraction and Refinement

After all the samples were successfully synthesized, XRD and ND were employed to verify whether the desired phases were obtained. XRD measurements were carried out using a PANalytical X'Pert Pro X-ray diffractometer with a Cu Kα source (1.54 Å) operated at 45 kV and 40 mA, over a recording range of $10° < 2\theta < 100°$. The XRD procedure was divided into two parts: an 8-minute quick scan was used to estimate the approximate proportion of impurities in the samples. The resulting patterns were analyzed using the Match! software. During this step, samples H005, H006 and H012 were discarded because the intensity of side phases could not be sufficiently reduced, even after repeated calcination, and the results will be shown in the next chapter. Once the intensity of side phases in the remaining samples was confirmed to meet the required criteria, a 32-minute-long scan was performed to ensure that the patterns would be clear enough for refinement.

The XRD patterns obtained from the 32-minute-long scan was refined using two methods in sequence: the Le Bail and Rietveld methods. The refinements were performed using the GSAS-II software. After fitting the background, Le Bail refinement was first employed to adjust the lattice parameters and instrument parameters so that the calculated peak positions, widths, and symmetries matched the measured patterns. Subsequently, the Le Bail refinement was deactivated, and the Rietveld method was used for further refinement to ensure that the calculated peak intensities closely matched the measured pattern. During the refinement process, the weighted R-factor (wR) quantitatively indicates the degree of agreement between the calculated and experimental data: when the wR value is below 10%, the refinement is generally considered sufficient to represent the actual crystal structure. Additionally, the covariance matrix can be used to check whether there are strong correlations between refinement parameters, allowing appropriate constraints to be set to improve the accuracy of the refinement. It should be noted that although the wR value quantitatively reflects the accuracy of the refinement, it is not the sole criterion for evaluating the goodness of fit; the difference profile is also an important indicator for assessing the quality of the refinement.

For the ND measurements, each sample was analyzed at two temperatures: room temperature and 780 K, using the same angular range as the XRD scans. The room-temperature ND data were refined together with the corresponding XRD patterns in a combined approach, while the ND patterns collected at 780 K were refined independently. Through this approach, we aimed to gain deeper insight into how the oxygen ion sublattice evolves, from an average structural perspective, as the Mo substitution level changes within the moderate working temperature range (around 500 °C). This systematic study provides important experimental evidence and theoretical support for understanding the relationship between the structure and ionic conductivity of the Sr/Ba series materials. The experimental plan is shown in Table 5. PEARL diffractometer of the TU Delft Reactor Institute (the Netherlands) was used to conduct the experiments. For each sample, 2.0g was taken out and placed in a V-Ni null-scattering alloy can with 6mm diameter. The sealed sample can was then mounted inside a neutron-transparent vacuum chamber, which was evacuated to a primary vacuum of about 10^{-3} mbar to prevent unwanted gas scattering during data acquisition. Neutron diffraction patterns were recorded over a total measurement time of approximately 4-5 hours, employing a neutron wavelength of 1.667 Å. This wavelength was selected through the (533) reflection of a single-crystal Ge[533] monochromator to ensure high resolution and optimal

intensity. For high-temperature diffraction experiments, the sample temperature was precisely controlled and maintained using a resistive heating system.

• Sample	• Mass (g)	• Measurement time at RT (hr)	• Measurement time at 780 K (hr)
• $Sr_3V_2O_8$	• *2-4*	• *4-5*	• *4-5*
• $Sr_3V_{1.9}Mo_{0.1}O_{8.05}$	• *2-4*	• *4-5*	• *4-5*
• $Sr_3V_{1.8}M_{0.2}O_{8.1}$	• *2-4*	• *4-5*	• *4-5*
• $Ba_3V_2O_8$	• *2-4*	• *4-5*	• *4-5*
• $Ba_3V_{1.9}Mo_{0.1}O_{8.05}$	• *2-4*	• *4-5*	• *4-5*
• $Ba_3V_{1.8}Mo_{0.2}O_{8.1}$	• *2-4*	• *4-5*	• *4-5*
• $Ba_3V_{1.7}Mo_{0.3}O_{8.15}$	• *2-4*	• *4-5*	• *4-5*

Table 5. Experimental Plan on Pearl Diffractometer

3.3 Fabrication of Pellets

To perform EIS, a hydraulic press was used to form the powder samples into pellets with a diameter of 6.35 mm and a thickness of approximately 2 mm. The pressed pellets were then placed in the furnace for sintering to obtain the final pellets for testing. Two key points must be ensured during pellet preparation: the pellets must not have visible cracks, and the density must meet the required condition (greater than 90%) to ensure that no macroscopic structural defects lead to increased resistance, thereby ensuring that the EIS results are accurate and reliable. The Archimedes method is applied to determine the density of the pellets. The measurement setup is shown in Figure 7. The samples were weighed at the dry state in the upper tray, then fully immersed in distilled water by placing on the metal net. Since the density of distilled water can be approximated as 1 g/cm^3 the difference between the two weights represents the sample's volume. The measured volume and the theoretical density from the combined refinement at room temperature were then used to calculate the pellet's relative density, as shown in the following formula:

$$\boldsymbol{Densification} = \frac{\boldsymbol{Dry\ weight}}{(\boldsymbol{Dry\ weight - Wet\ weight})} \times \frac{\mathbf{1}}{\boldsymbol{principle\ density}} \times \mathbf{100\%} \quad (7)$$

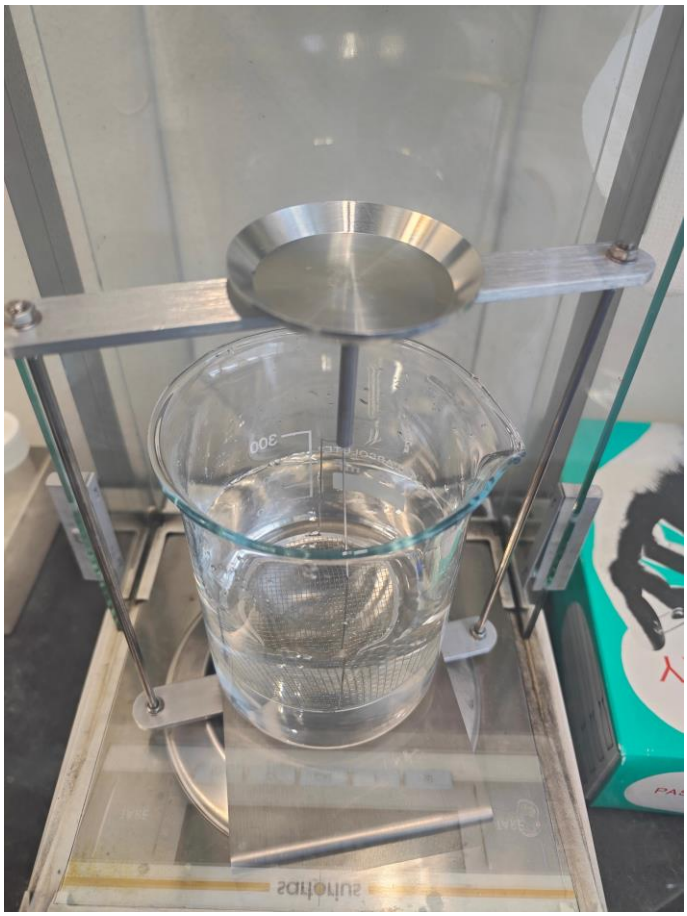

Figure 7. Set up for The Densification Measurement

Meanwhile, due to a series of earlier characterization tests, the quantity and quality of the first batch of synthesized samples were no longer sufficient for pellet preparation attempts. To carry out the subsequent experiments and ensure the reproducibility of the earlier results, a new batch of samples, as shown in Table 6, was synthesized after discarding the compositions that could not be successfully prepared in the first batch. Le Bail refinement was performed on this new batch to confirm whether the unit cell parameters were close to those of the first batch, thereby ensuring that they could be used for the preparation of corresponding pellets.

$Sr_3V_{2-x}Mo_xO_{8+x/2}$		$Ba_3V_{2-x}Mo_xO_{8+x/2}$	
Sample number	Expected chemical	Sample number	Expected chemical
H015	$Ba_3V_2O_8$	H019	$Sr_3V_2O_8$
H016	$Ba_3V_{1.9}Mo_{0.1}O_{8.05}$	H020	$Sr_3V_{1.9}Mo_{0.1}O_{8.05}$
H017	$Ba_3V_{1.8}Mo_{0.2}O_{8.1}$	H021	$Sr_3V_{1.8}Mo_{0.2}O_{8.1}$
H018	$Ba_3V_{1.7}Mo_{0.3}O_{8.15}$		

Table 6. Name of the Samples and Their Corresponding Chemicals

4 Results and Discussion

4.1 Solid-State Synthesis

4.1.1 Reproduction of Fop's Work

We first conducted a reproducibility verification of the work by Fop et al., namely the synthesis results of the sample without substitution (X=0). Since the original paper did not provide explanation for calcination temperature, duration, and number of cycles, multiple calcination cycles was carried out based on the reported process (calcination at 1100°C for 10 hours). After each calcination, an 8-minute quick XRD scan was performed to confirm whether the product was formed. If side phases were present, the crashed powder was re-pressed into pellets and calcined again. The results of the first calcination's quick XRD scan for the $Sr_3V_2O_8$ and $Ba_3V_2O_8$ samples are shown in Figure 8. By analyzing the patterns from Software Match!, it can be seen that for $Sr_3V_2O_8$, after the first calcination, some side phases (V_2O_5) still appear around 30° for the H001 sample ($Sr_3V_2O_8$), while no such side phases are present for the H002 sample ($Ba_3V_2O_8$). Therefore, $Sr_3V_2O_8$ underwent a second calcination. The comparison of the XRD quick scans between the first and second calcinations is shown in Figure 9. At this point, the side phases have disappeared. This phenomenon can be explained by the following reason: Since the ionic radius of Sr^{2+} (1.18 Å) is smaller than that of Ba^{2+} (1.42 Å), the larger Ba^{2+} can promote lattice expansion, making it easier for V_2O_5. to diffuse into the lattice, thereby accelerating the reaction. Sr^{2+}, on the other hand, requires more precise diffusion and reaction conditions, and the first calcination time might be insufficient, or diffusion might be limited [67; 68]. In addition, in the Sr-V-O system, intermediate phases such as SrV_2O_7 and SrV_2O_6 are relatively stable at intermediate temperatures, making it more difficult for them to convert into the target phase [69; 70]. In contrast, such intermediate phases are observed during the calcination of Ba series, it might be because they are less commonly formed in the Ba-V-O system or tend to convert more readily into the final product. This conjecture can be further verified through TGA-DSC testing.

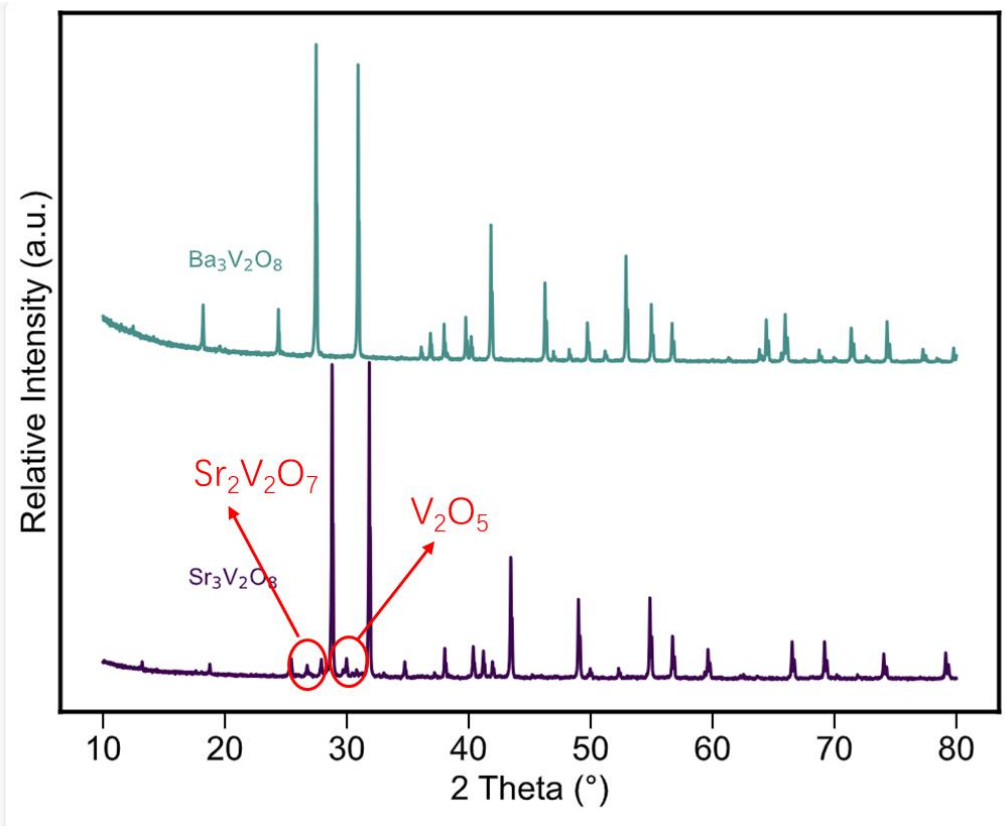

Figure 8. XRD Patterns for The First Calcination of $Sr_3V_2O_8$ and $Ba_3V_2O_8$

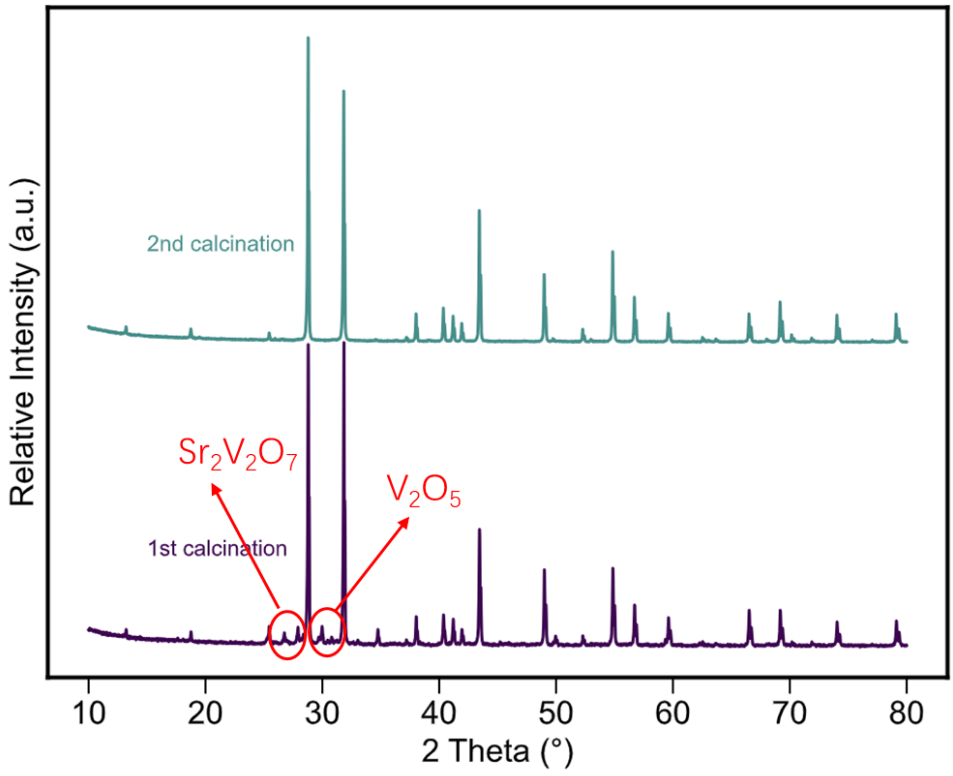

Figure 9. XRD Patterns for The First and Second Calcination of $Sr_3V_2O_8$

4.1.2 Molybdenum substitution

After the reproduction step, we investigated the Mo-substituted samples. Based on the synthesis experience of $Sr_3V_2O_8$, the same method of multiple calcination cycles combined with quick XRD scans after each calcination was used to verify the sample purity. Taking sample H003 ($Sr_3V_{1.9}Mo_{0.1}O_{8.05}$) as an example, as shown in the Figure 10, after the first calcination, the fitting results from the Match! software indicated that $Sr_3V_{1.9}Mo_{0.1}O_{8.05}$ still contained side phases such as V_2O_5, MoO_3, and $SrMoO_4$. Therefore, further calcination was carried out to confirm whether the sample purity could be improved. The Figure 11 shows the XRD quick scan patterns of the $Sr_3V_{1.9}Mo_{0.1}O_{8.05}$ sample after three calcination cycles. It can be clearly seen that with the increase of calcination times, the intensity of side phases at 26.2°, 27.4°, and 31.3° gradually decreased. Compared to H003, the sample H009, namely $Ba_3V_{1.9}Mo_{0.1}O_{8.05}$, required only two calcination cycles to remove the side phase (as shown in the Figure 12). Overall, the Sr series samples all required three calcination cycles, while the Ba series samples all underwent two, which is similar to the previous results of Sr/$Ba_3V_2O_8$: the Ba series required fewer calcination cycles than the Sr series, but compared to the unsubstituted samples, still needed more calcination. This phenomenon may be caused by the following reasons: during the mixing of precursor powders, MoO_3 powder was observed to be prone to agglomeration, making it difficult to mix evenly with other precursors, leading to incomplete reactions and thus requiring multiple calcination steps; at the same time, MoO_3 has high volatility at high temperatures, and since calcination was conducted in air, MoO_3 tends to sublimate in air, resulting in partial evaporation during the first calcination and thus reducing the actual Mo content participating in the reaction, affecting the formation of the target phase [71; 72]. These two points have already been confirmed in the first XRD scan of $Sr_3V_{1.9}Mo_{0.1}O_{8.05}$. In addition, the substitution of Mo may also alter the diffusion rate, affecting the cation diffusion rate and thereby delaying the formation of the main phase.

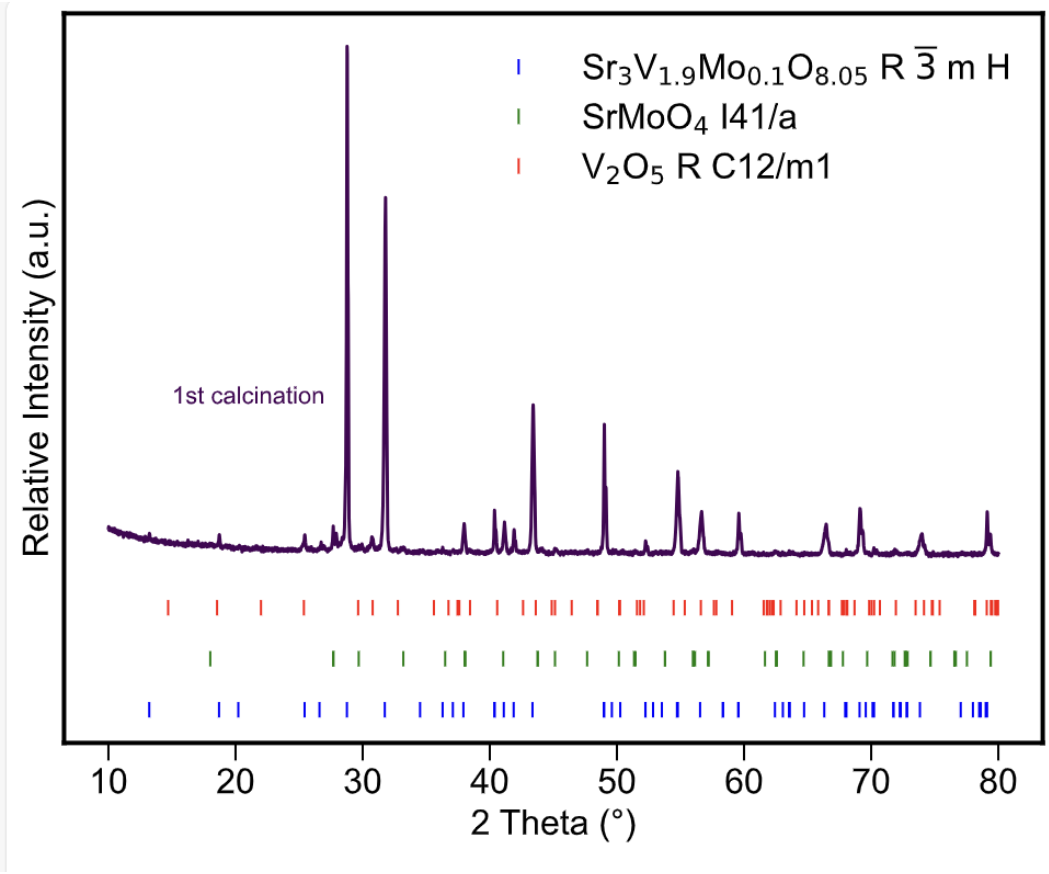

Figure 10. XRD Patterns of $Sr_3V_{1.9}Mo_{0.1}O_{8.05}$ after The First Calcination with Fitting in the Match!

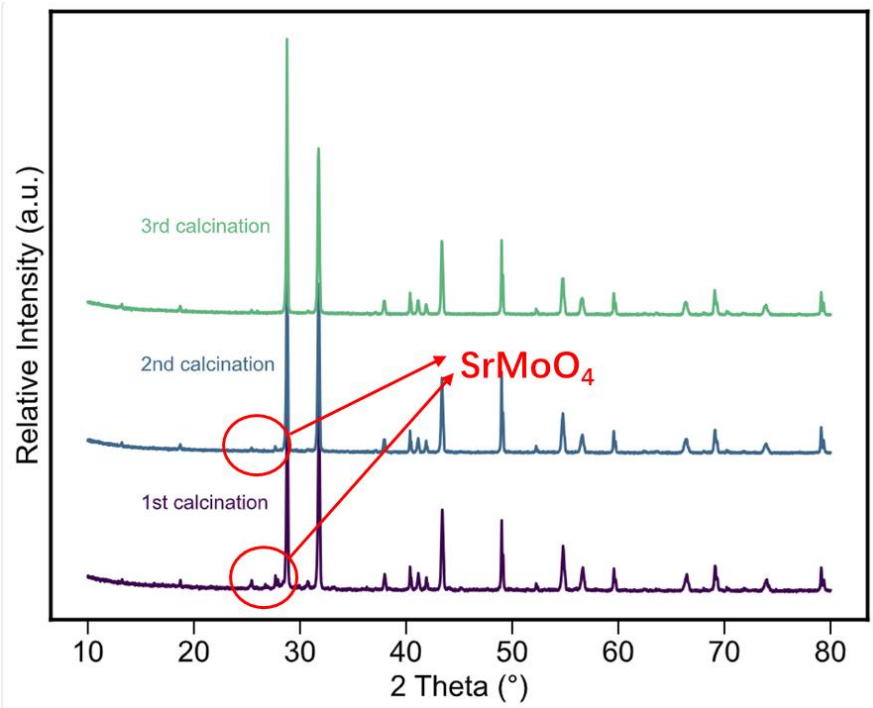

Figure 11. Comparison of The XRD Patterns of $Sr_3V_{1.9}Mo_{0.1}O_{8.05}$ from The First to The Third Calcination

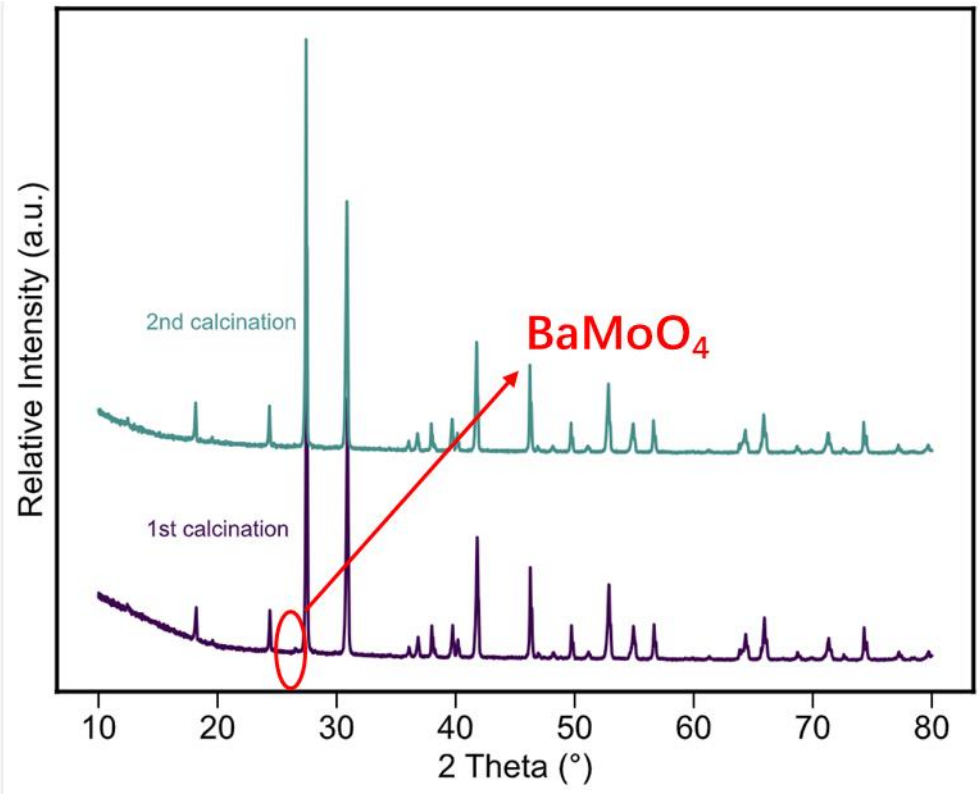

Figure 12. Comparison of The XRD Patterns of $Ba_3V_{1.9}Mo_{0.1}O_{8.05}$ between The First and Second Calcination

Subsequently, we compared the XRD results of samples synthesized from pre-dried precursors (H007 and H008) with those from undried precursors (H003 and H004). Figure 13 and Figure 14 respectively show the comparison results of $Sr_3V_{1.9}Mo_{0.1}O_{8.05}$ and $Sr_3V_{1.8}Mo_{0.2}O_{8.1}$ after three calcination cycles. It is clearly observed that for $Sr_3V_{1.9}Mo_{0.1}O_{8.05}$, the sample synthesized from pre-dried precursors (H007) exhibited a side phase of V_2O_5. For $Sr_3V_{1.8}Mo_{0.2}O_{8.1}$, the dried sample showed a clear side phase of $SrMoO_4$. The reason for this phenomenon is that the drying temperature (200 °C) caused some precursors, such as V_2O_5, to form large primary particles, reducing the surface reactivity and leading to incomplete reaction during subsequent high-temperature treatment. These crystallized phases are difficult to fully react with other components, resulting in the retention of side phases even after three calcination cycles [73; 74]. In addition, during the drying process at 200 °C, some metal salts (such as carbonates, MoO_3, V_2O_5, etc.) may have already undergone partial low-temperature reactions or interactions, forming metastable intermediate phases or oxide clusters [71; 75]. These intermediate structures are difficult to break during the subsequent high-temperature sintering, thus hindering the uniform formation of the target phase and leading to increased side phases. Meanwhile, during drying at 200 °C, possible hydrates or trace liquid phases in the system may have evaporated too quickly, causing ions such as Mo^{6+} or V^{5+} to migrate and enrich in local regions [76; 77]. Since no stirring or mechanical dispersion was performed on the precursor powders during drying, the “layering effect” or “film formation effect” could have caused uneven elemental distribution [78; 79]. MoO_3 is prone to recrystallize during heating, forming flaky or blocky particles, and its intrinsic reactivity is limited.

The drying process can promote its agglomeration, reducing the contact interface with V_2O_5, $SrCO_3$, etc., during subsequent reaction [75]. As a result, the dried solid exhibits compositional inhomogeneity, making it difficult to form a single-phase product during sintering, which explains the formation of the $SrMoO_4$ side phase.

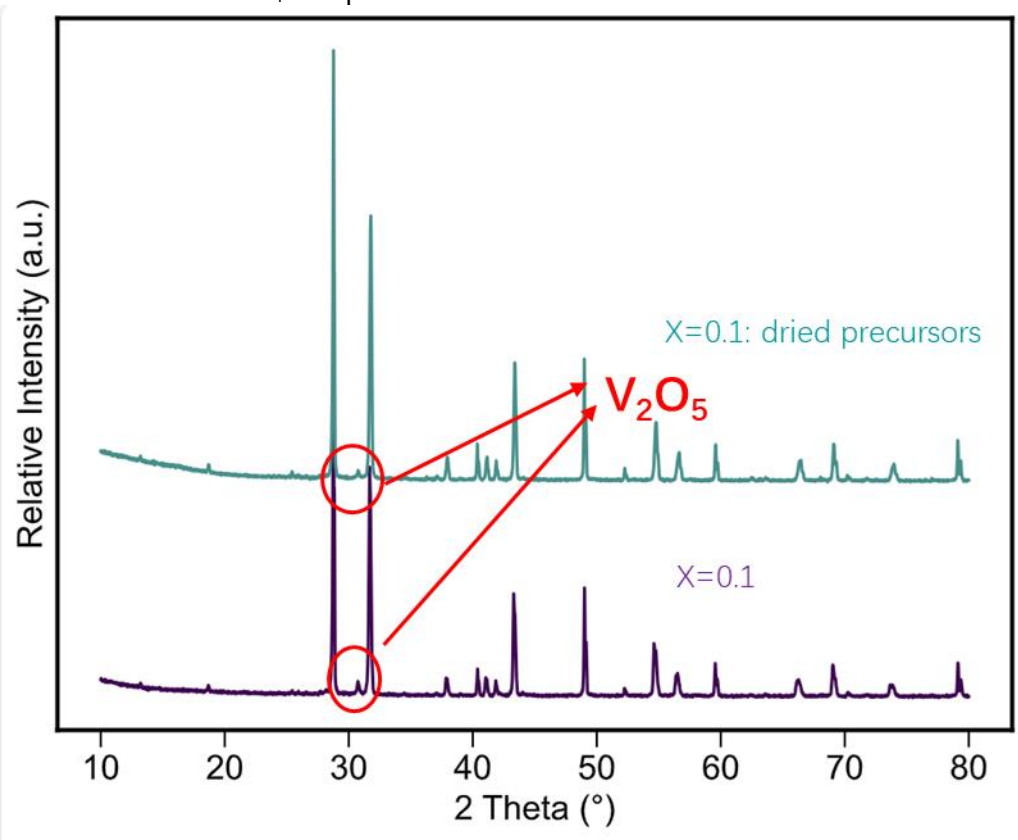

Figure 13. Comparison of The XRD Patterns of $Sr_3V_{1.9}Mo_{0.1}O_{8.05}$ between Dried Precursors and Normal ones

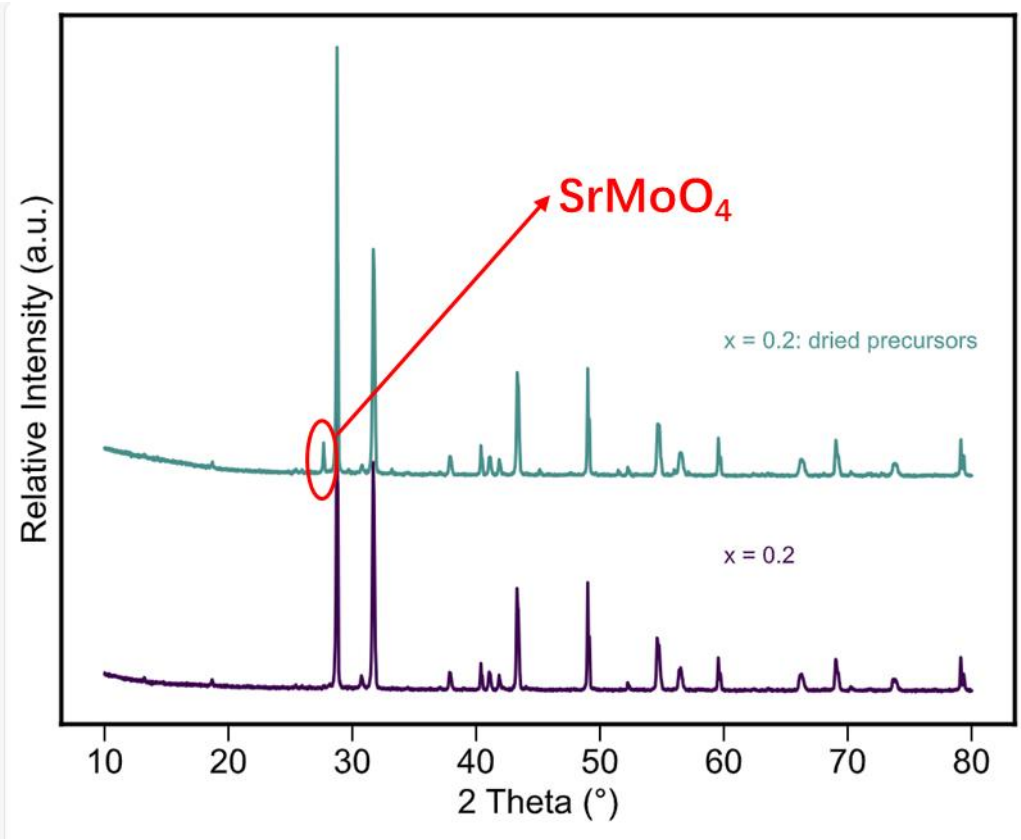

Figure 14. Comparison of The XRD Patterns of $Sr_3V_{1.8}Mo_{0.2}O_{8.1}$ between Dried Precursors and Normal ones

The reasons we chose not going for further studies for x=0.3 and 0.4 in the Sr series and x=0.4 in the Ba series in the subsequent experiments are analyzed from the Figure 15. Here are the quick XRD scan patterns after the second calcination for the Ba series. For H012 (x=0.4), even after two calcination cycles, there are still obvious $BaMoO_4$ side phases. Since significant $BaMoO_4$ side phases were observed after the first calcination, a further comparison was made by placing the first and second calcination XRD results of H010 (x=0.2) and H012 (x=0.4) together, as shown in the Figure 16. It can be seen that for $Ba_3V_{1.8}Mo_{0.2}O_{8.1}$ (Figure 16a), after the second calcination, the intensity of the side phases was significantly reduced, indicating that the side phases could continue to participate in the reaction to form the primary phase. However, for x=0.4, the intensity of the side phases did not decrease significantly after the second calcination, suggesting that there might be a solubility limit at x=0.4, where Mo^{6+} could no longer be uniformly incorporated into the V sites of the lattice, and the excess Mo^{6+} was expelled to form stable side phases. Alternatively, at high substitution levels, part of the Mo^{6+} might tend to form more thermodynamically stable side phases with Ba^{2+} and V^{5+}, such as $BaMoO_4$, which are thermodynamically stable at high temperatures and difficult to reincorporate into the main phase lattice even after the second calcination, resulting in almost unchanged side phase content. In addition, if Mo is unevenly distributed at high substituting concentration, the local Mo content in some areas may far exceed the local capacity, leading to Mo-rich side phases, and the second calcination cannot improve such macroscopic segregation. The same phenomenon was observed in the Sr series samples with x=0.3 and x=0.4 (shown in the Figure 17); therefore, these three samples were also abandoned and not further characterized.

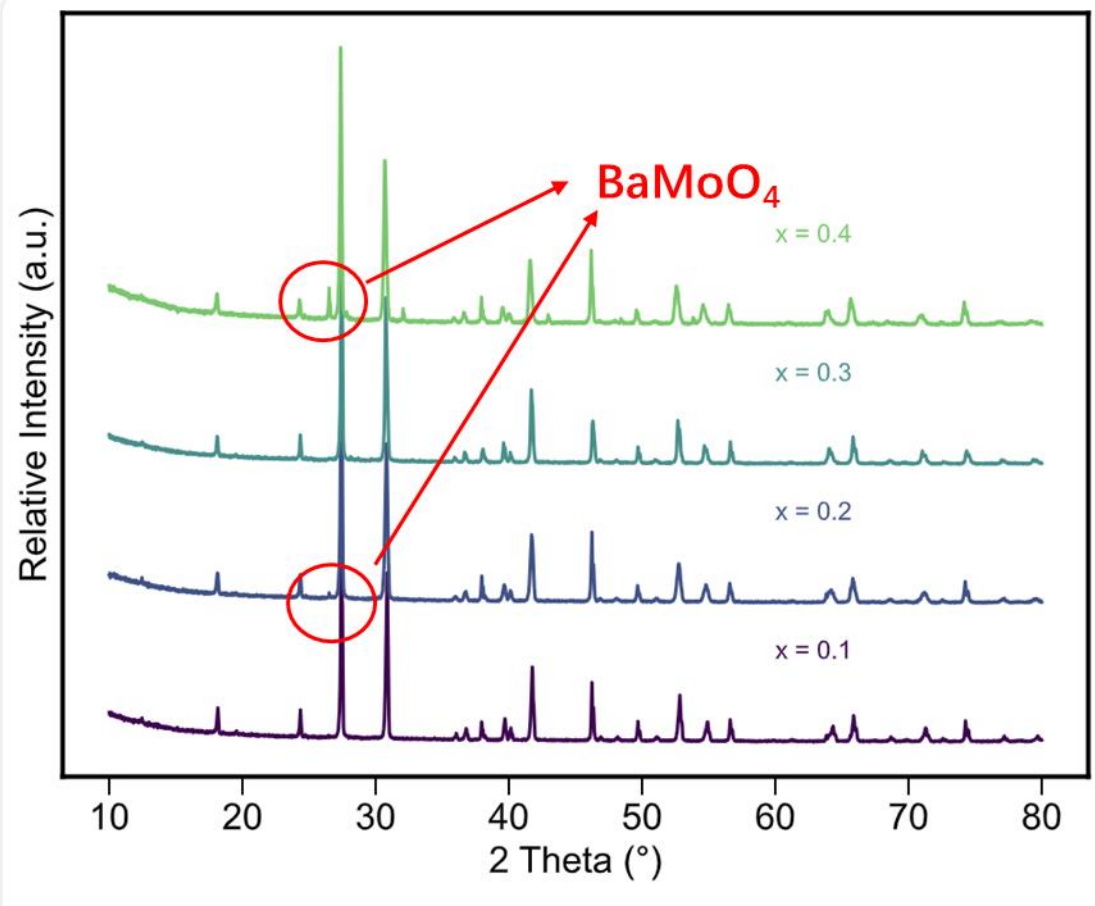

Figure 15. The XRD Patterns of Ba Series Samples after The Second Calcination

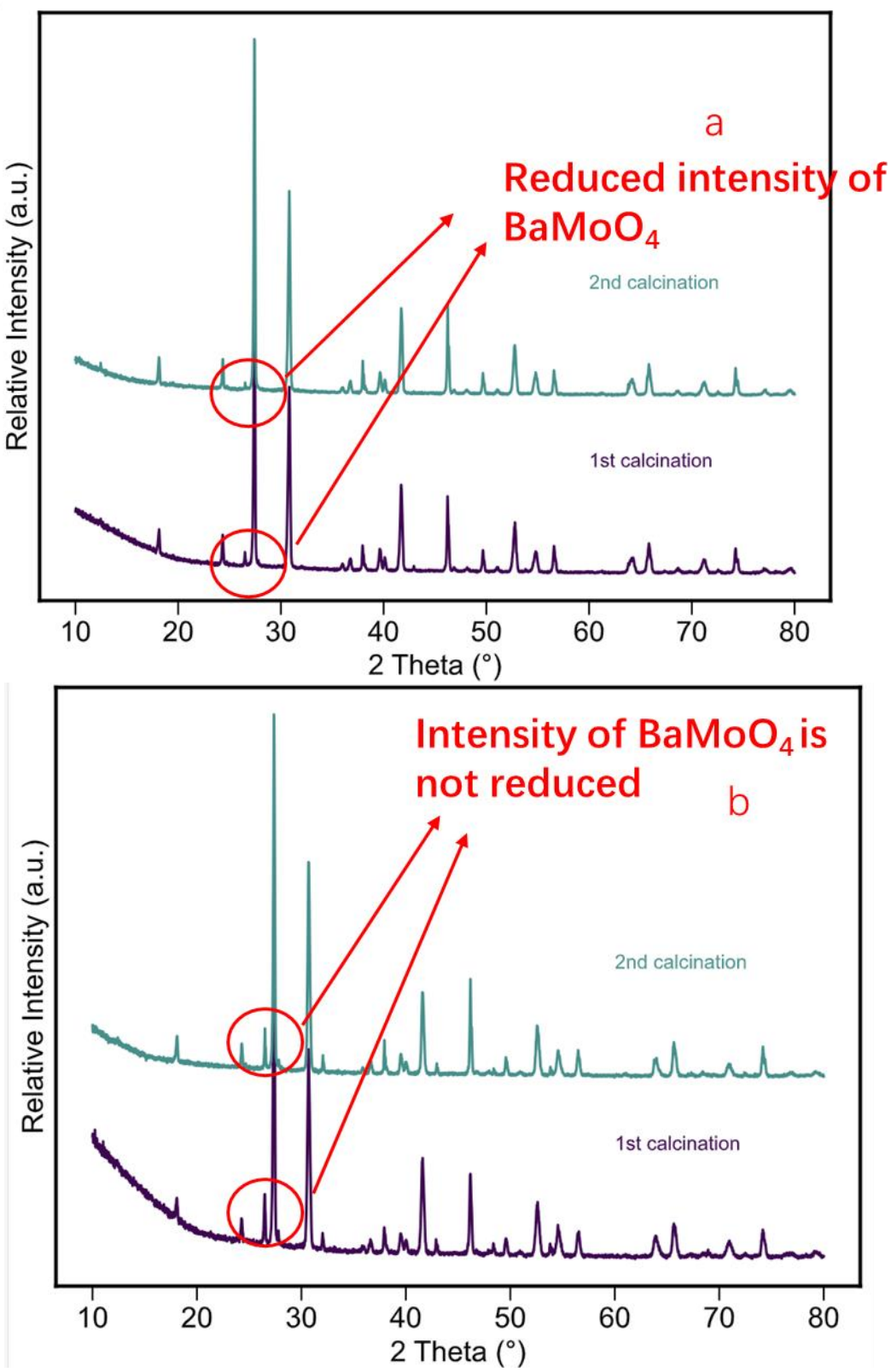

Figure 16. The First and Second Calcination XRD Patterns of $Ba_3V_{1.8}Mo_{0.2}O_{8.1}$(a) and $Ba_{1.6}Mo_{0.4}O_{8.2}$(b)

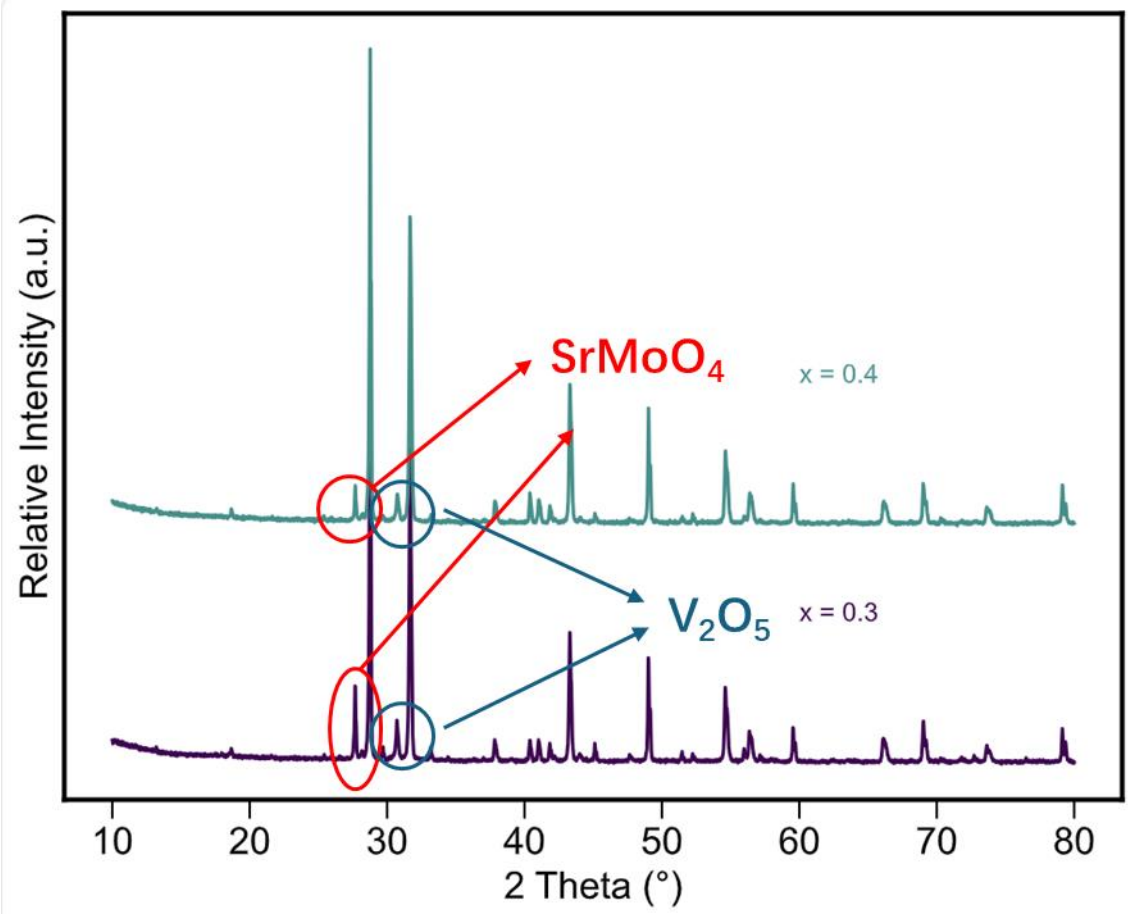

Figure 17. The Third Calcination XRD Patterns of $Sr_3V_{1.7}Mo_{0.3}O_{8.15}$ and $Sr_{1.6}Mo_{0.4}O_{8.2}$

4.2 Refinement Results

Before the discussion, the ICP-MS results are worth mentioning. Table 7 shows the ICP-MS test results of 7 selected samples after the solid-state synthesis steps. It can be noted that except for $Sr_3V_2O_8$, all samples show a significant deficiency of A-site elements. Several mechanisms can be used to explain this phenomenon. The most likely explanation is that during the calcination process, oxides or carbonates of Sr and Ba may partially sublimate or decompose at high temperatures. Especially for $BaCO_3$, it tends to decompose into BaO and CO_2 above 1000°C, and under certain conditions, BaO may volatilize [80]. Meanwhile, if acidic components (such as V_2O_5 or MoO_3) are present in the atmosphere or system, they may promote the loss of Ba^{2+} or Sr^{2+} [81]. During high-temperature reactions, A-site elements may combine side phases to form volatile or undetectable intermediate products [82]. This is especially likely in the presence of Mo substitution, which may induce locally non-ideal reaction pathways, ultimately resulting in a decrease in the actual content of A-site ions with increasing Mo content. Another possibility is that MoO_3 and V_2O_5 may form a low-melting eutectic phase (around 500–600°C) at high temperatures, forming a localized molten liquid phase. This liquid phase may "trap" a portion of A-site elements (Ba^{2+} or Sr^{2+}) but later separate from the main phase and fail to be uniformly sampled during grinding, resulting in a measured deficiency [83; 84]. Additionally, under Mo^{6+} substituting conditions, to maintain charge neutrality, the structure may spontaneously generate

A-site vacancies, for example forming a structure like $Ba_{3-y}V_{2-x}Mo_xO_{8+x/2}$, as a reasonable chemical compensation mechanism. This may require charge balance modeling for further verification [85].

$Sr_3V_{2-x}Mo_xO_{8+x/2}$			
X	*Sr*	*V*	*Mo*
$Sr_3V_2O_8$	2.935	2	
$Sr_3V_{1.9}Mo_{0.1}O_{8.05}$	2.854	1.875	0.124
$Sr_3V_{1.8}Mo_{0.2}O_{8.1}$	2.837	1.813	0.187

$Ba_3V_{2-x}Mo_xO_{8+x/2}$			
X	*Ba*	*V*	*Mo*
$Ba_3V_2O_8$	2.799	2	
$Ba_3V_{1.9}Mo_{0.1}O_{8.05}$	2.795	1.901	0.099
$Ba_3V_{1.8}Mo_{0.2}O_{8.1}$	2.578	1.822	0.178
$Ba_3V_{1.7}Mo_{0.3}O_{8.15}$	2.702	1.736	0.264

Table 7. ICP-MS Results of the Selected Samples

4.2.1 Le Bail Refinement

After obtaining powders with sufficiently high purity, a 30-minute long-time XRD scan was applied to each sample powder respectively, for use in XRD refinement. The Le Bail method was first used. The unit cell parameters obtained from the Le Bail refinement of the room temperature XRD data are shown in the Figure 18. It can be clearly observed that as the degree of Mo^{6+} substitution for V^{5+} increases, all seven samples exhibit a gradual increase in a and a gradual decrease in c. The increase in a can mainly be explained by two reasons: the ionic radius of Mo^{6+} is larger than that of V^{5+} (0.59 Å > 0.54 Å), which to some extent causes stretching of the crystal in the ab-plane [67; 68]. At the same time, as Mo^{6+} substitutes for V^{5+} in the structure, it brings stronger Mo–O bonds due to its higher charge. Although Mo–O bonds are shorter, their strong bonding introduces local distortions in the surrounding tetrahedral units [86]. These distortions

are easier to accommodate in the a-axis, which lies in the plane of the structure. This causes in-plane tension, leading to the expansion of the a-axis. In other words, the lattice stretches more easily sideways because the hexagonal framework is more flexible in that direction.

For the c-axis, although the larger ionic radius would theoretically lead to an increase in the unit cell parameter, other factors cause the crystal to shrink along the c-axis. With the increasing substitution of Mo, it also increases the oxygen content in the structure — from O_8 to $O_{8+x/2}$ — which fills existing oxygen vacancies. These additional oxygens enhance connectivity between polyhedral units along the c-axis, effectively tightening the structure in that direction [87]. Moreover, Mo–O bonds are shorter and stronger, so when Mo occupies the tetrahedral site, it pulls the connected oxygen atoms closer [86]. This causes the layers to pack more tightly along the stacking direction, leading to a contraction of the c-axis. It is a kind of axial compression driven by chemical pressure and charge compensation.

In addition, since no high-temperature XRD was performed, only the high-temperature neutron diffraction data were subjected to Le Bail refinement, and the results are shown in the Figure 19. Compared with the refinement results at room temperature, it can be seen that the unit cell parameters have increased significantly. This is because atoms in the crystal are confined in potential wells. As the temperature rises, their thermal vibrations become stronger, which increases the average interatomic distances and leads to lattice expansion (in both a and c). The thermal expansion coefficients of a and c are often different in hexagonal or layered structures. Typically, the c-axis shows more obvious expansion because it corresponds to the interlayer distance or octahedral stacking, which is structurally "looser." This agrees with the observation in the Figure 19, where the increase along the c-axis is more pronounced.

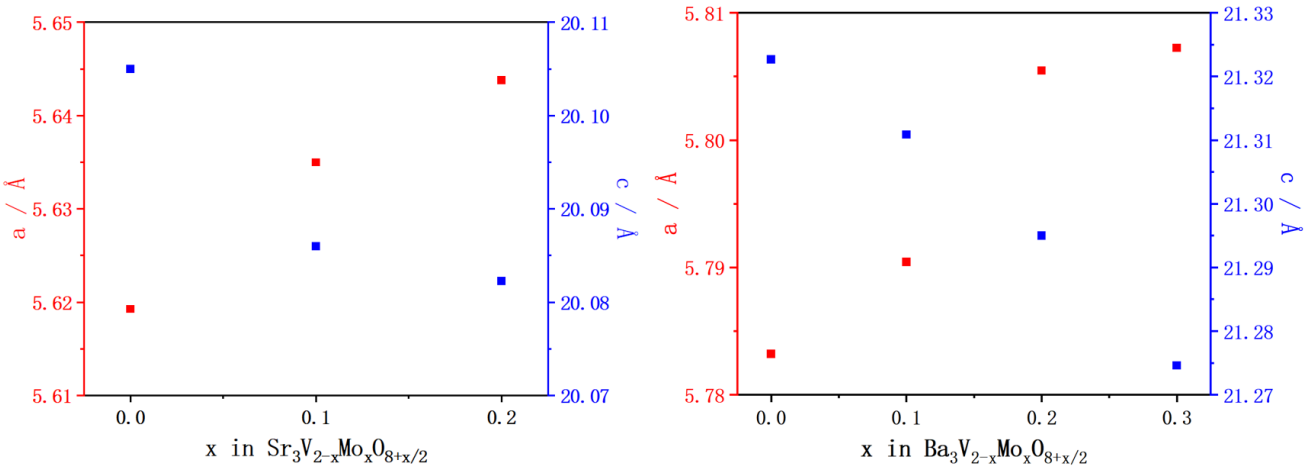

Figure 18. The Unit Cell Parameters of the Selected Samples in Room Temperature Done by the Le Bail Refinement of XRD Patterns

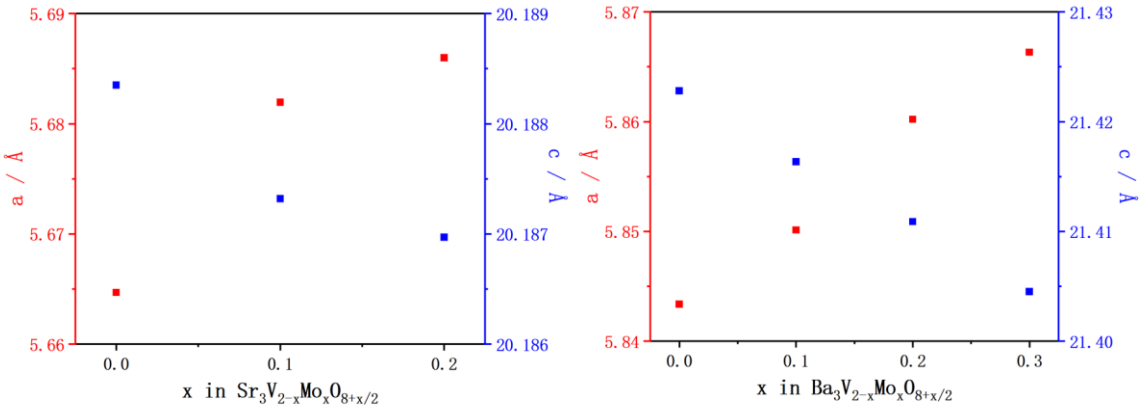

Figure 19. The Unit Cell Parameters of the Selected Samples in 780K Done by the the Le Bail Refinement of ND Patterns

To make sure the production of the powders is reproduceable, and more powders can be used to produce the pellets, Le Bail method was used again on the second batch to verify their structure, the results are shown in the Appendix B. The comparison of the results is shown in the Figure 20 and Figure 21: it can be clearly seen that the second batch shows the same trend in the unit cell parameters in the first batch, showing that the substitution of Mo into the $A_3V_2O_8$ is reproduceable.

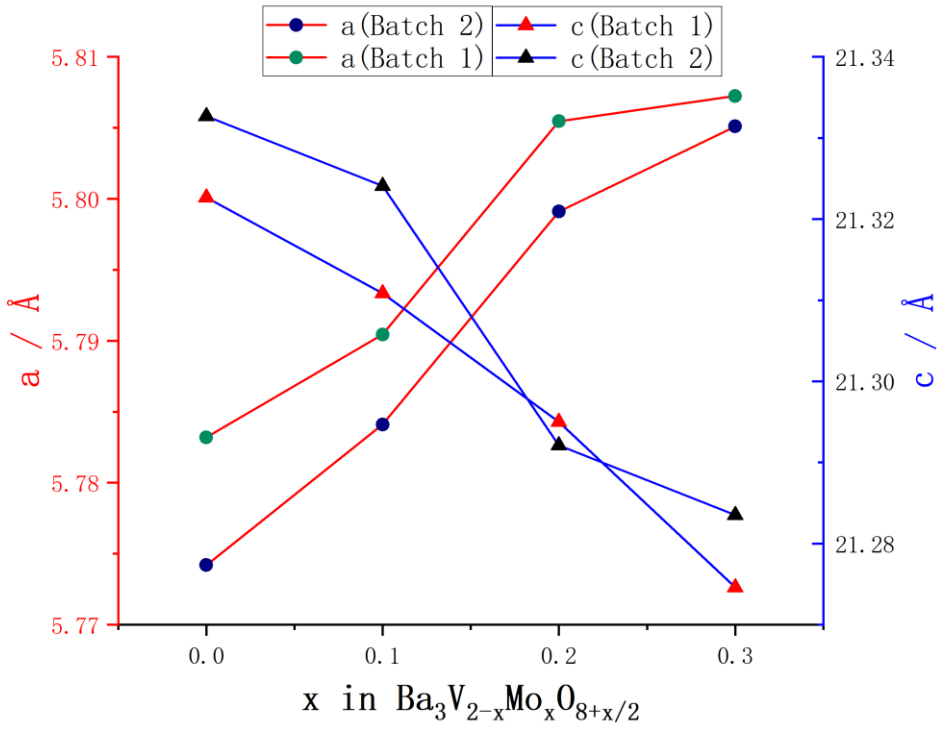

Figure 20. The Comparison of The Unit Cell Parameters of the Ba Series Samples between The First and Second Batch in Room Temperature

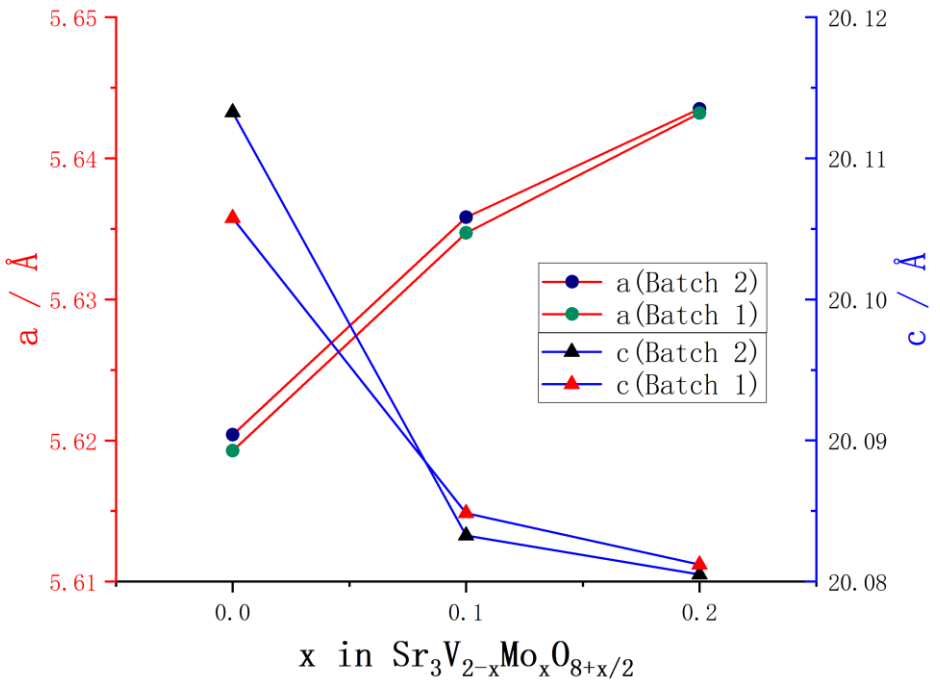

Figure 21. The Comparison of The Unit Cell Parameters of the Sr Series Samples between The First and Second Batch in Room Temperature

4.2.2 Rietveld Refinement

After completing the Le Bail refinement, the lattice parameters of the samples were obtained, and the crystal structure was well understood. However, the Le Bail refinement does not provide information on atomic positions, occupancies, or thermal vibrations. Therefore, we proceeded with Rietveld refinement to analyze the structure in more detail. The refinement results are presented in the Appendix A. Figure 22 shows the structural models obtained from the combined refinement of $Sr_3V_2O_8$ (H001) and $Ba_3V_2O_8$ (H002) at room temperature. It is clearly observed that the refined structural models are generally consistent with the results reported by Fop et al.: the A-site atoms occupy two positions, A1(marked with orange) and A2(marked with green), corresponding to Wyckoff sites 3a and 6c, respectively here the green one is the A1 while the blue one represents A2. V occupies a single position marked with red in the red tetrahedral, Wyckoff site 6c, while O atoms occupy two positions, Wyckoff sites 36i(in pink) and 18h(in blue) [51]. This further demonstrates that the reproduction of the work by Fop et al. was successful [51]. What needs to be mentioned is that here Oxygen is split because of the scattered density shown in the Fourier map (Figure 23).

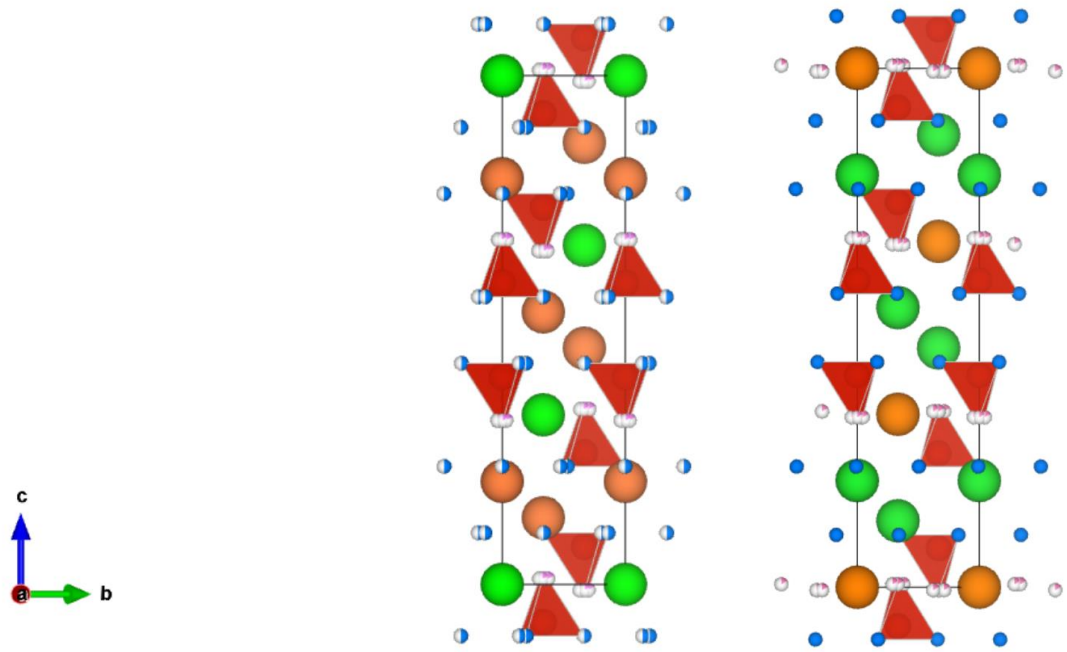

Figure 22. The Structure Model of $Sr_3V_2O_8$ (H001) and $Ba_3V_2O_8$ (H002) in Room Temperature

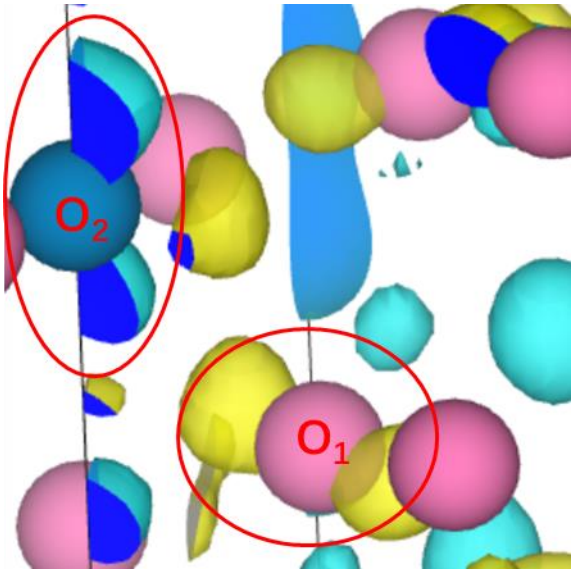

Figure 23. Fourier Map of $Sr_3V_2O_8$ (H001), it can be clearly shown that before split there is obvious scattering density(in red circle) around the O1 and O2.

In the $A_3V_2O_8$ structure, the B-site cations may occupy two different metal positions, M1 and M2. M1 is typically tetrahedrally coordinated but may also appear in distorted octahedral or five-fold coordination geometries. M2 generally exhibits octahedral coordination. According to the results reported by Fop et al, in Figure 4, V^{5+} usually occupies the M1 site, forming VO_4 tetrahedra or distorted units [51]. Upon substituting the $A_3V_2O_8$ structure with Mo, Mo^{6+} ions are expected to primarily occupy the M1 site, due to their similar ionic radii and oxidation states, as they belong to the same group of elements. Mo^{6+} is more likely to replace V^{5+} at the M1 site, resulting in a combination of tetrahedral and octahedral units [88]. Also because M1 site is tetrahedrally

coordinated, it might lead to MoO_4^{2-}-like structural units [89]. However, it is also possible for Mo to enter the M2 site (octahedral coordination), particularly under conditions of high Mo substitution levels or when structural distortions occur due to temperature, atmosphere, or other factors.

Before performing the Rietveld refinement, several constraints were applied in GSAS-II to ensure that the refinement would not produce unphysical results (such as atomic occupancies greater than 1 or negative Uiso values). The sample H010 ($Ba_3V_{1.8}Mo_{0.2}O_{8.1}$) is used here as an example to discuss the structural effects induced by Mo substitution. Figure 24 presents the refinement results for $Ba_3V_{1.8}Mo_{0.2}O_{8.1}$. First, Mo substitution does not guarantee that a single lattice site is occupied by a specific atom; instead, Mo and V are randomly distributed according to a certain ratio. In $Ba_3V_2O_8$, V usually exists in the form of V^{5+} (d0), which leads to a more symmetric and uniform coordination environment, without significant displacements or local defects. Moreover, in the refinement of $Ba_3V_{1.8}Mo_{0.2}O_{8.1}$ samples, the scattering density was observed in the Fourier diagram (shown in Figure 25). Therefore, in addition to substituting V at the Wyckoff site 6c with Mo1, an additional Mo2 atom was introduced at the Wyckoff site 3b. These two Mo positions were assigned different occupancies to improve the realism of the fit. Mo substitution also causes positional shifts or distortions of oxygen atoms. These effects were modeled by splitting the oxygen positions and assigning them different coordinates and occupancies. After several trials, it was found that splitting O into six closely related positions led to better fitting results. As a result, O1 was split to achieve improved refinement. However, even after the splitting, O1 could not adequately reproduce the neutron diffraction electron density (shown in Figure 25b). Therefore, the coordinates of O1 were duplicated to create a new oxygen atom, O3 (Wyckoff site 18f), and further adjusted to improve fitness. In Figure 24, the cyan spheres represent O1, blue represents O2, orange represents O3, green and black represents the A1 and A2 site cation (Ba^{2+}) respectively, the red represents the V at M1 site, yellow represents the Mo at M1 site, and pink represents the Mo at M2 site. The red polyhedral corresponds to those formed around V^{5+} and Mo^{6+} at M1 site, while the pink polyhedral corresponds to those surrounding Mo^{6+} at M2 site. It was guessed that at M1 site, V^{5+} is still VO_4 tetrahedral unit, while the substituted Mo forms the MO_6 Octahedral unit. Detailed explanations will be presented as follows.

a

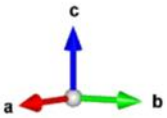

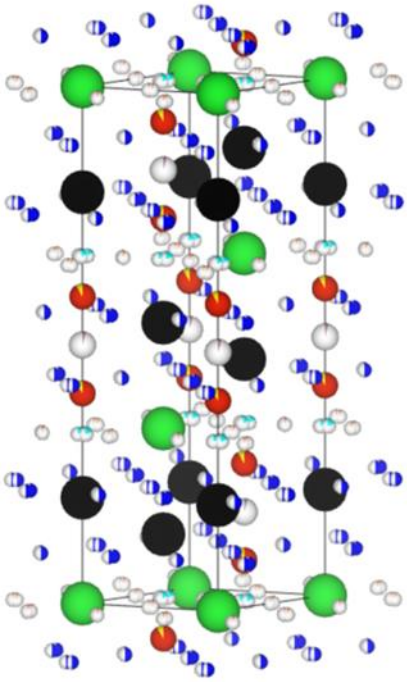

b

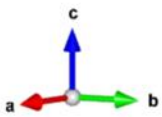

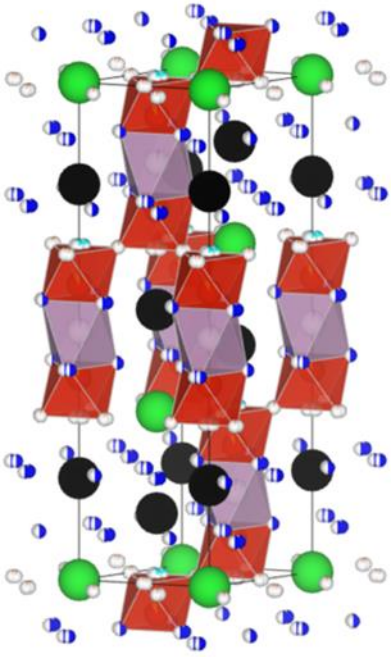

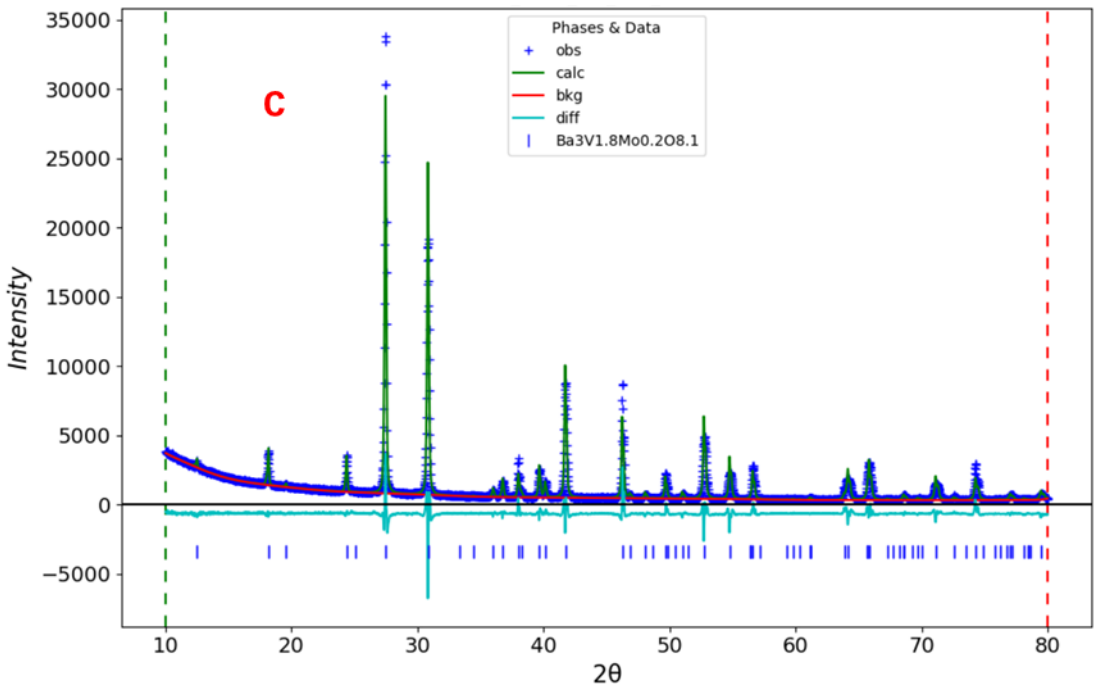

Figure 24. The Structure Model of H010($Ba_3V_{1.8}Mo_{0.2}O_{8.1}$) in Room Temperature, without the polyhedral(a), with polyhedral(b) and the Refinement Fit Result(c)

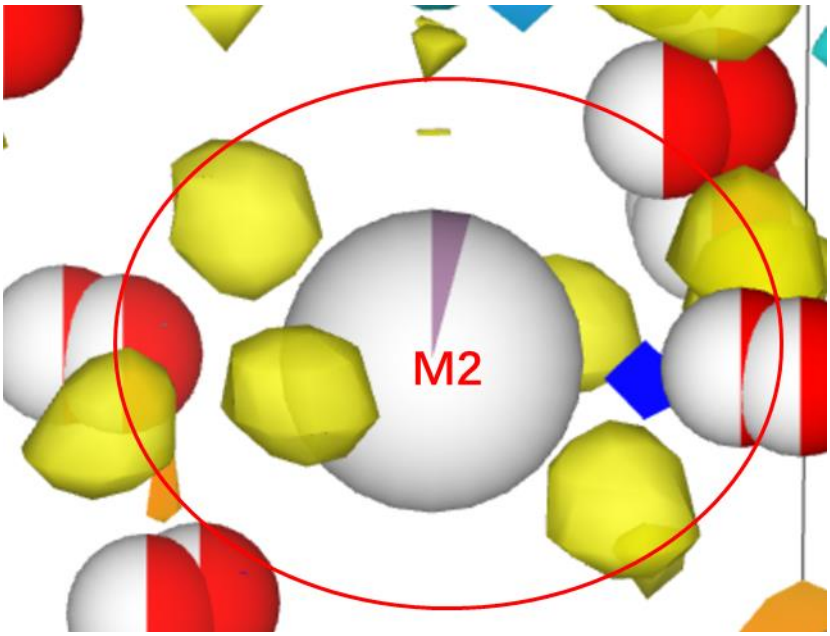

Figure 25. Fourier Map of $Ba_3V_{1.8}Mo_{0.2}O_{8.1}$(H010), it can be clearly see that there is scattering density(in red circle) around M2 site.

When setting the constraints, it was first assumed that Mo1 primarily substitutes for V in the original structure, and thus their coordinates along the Z-axis were constrained to be the same. Additionally, since both are B-site cations, their thermal vibration parameters were considered equivalent. Therefore, the Uiso values of V, Mo1, and Mo2 were set to be equal. In order to maintain the overall stoichiometry in the refined model, constraints were also applied to the

fractions of Mo and O. After the split, Mo1 was assigned to the Wyckoff site 6c and Mo2 to the Wyckoff site 3b. Accordingly, the occupancy of Mo was constrained as follows:

$$\boldsymbol{fMo1 * 6 + fMo2 * 3 = 0.6} \quad (\mathbf{8})$$

Here, $fMo1$ and $fMo2$ represent the fractional occupancies of Mo on the two respective sites. Since the palmierite structure is based on the c'hh stacking sequence, where three structural units combine to form the unit cell, the total Mo content in the unit cell should be three times that in the formula unit—i.e., 0.6 in this case. For the same reason, similar constraints were applied to the oxygen atoms to ensure that their total occupancy also reflects the stoichiometry of the full unit cell.

$$\boldsymbol{fO1 * 36 + fO2 * 36 + fO3 * 18 = 24.3} \quad (\mathbf{9})$$

Here, $fO1$, $fO2$, and $fO3$ represent the fractions of O1, O2, and O3, respectively. During the refinement process, the Uiso of O3 frequently tended to be negative, which was physically unreasonable. Therefore, the Uiso values of all three oxygen sites were constrained to be equal to ensure a physically meaningful refinement result. The structure parameters of the refinement results are shown in Figure 26

Structure parameters

			x	y	z	Occ.	U	Site	Sym.
1	Ba	Ba1	0.00000	0.00000	0.00000	1.000	0.014	3a	-3m
2	Ba	Ba2	0.00000	0.00000	0.20459	1.000	0.012	6c	3m
3	V	V	0.00000	0.00000	0.40630	0.900	0.004	6c	3m
4	O	O1	0.02500	0.03980	0.32773	0.163	0.009	36i	1
5	O	O2	0.18100	-0.13940	0.56596	0.510	0.009	36i	1
6	O	O3	0.33333	0.18000	0.66667	0.004	0.009	18f	.2
7	Mo	Mo1	0.00000	0.00000	0.40629	0.095	0.004	6c	3m
8	Mo	Mo2	0.00000	0.00000	0.50000	0.011	0.004	3b	-3m

Figure 26. Structure Parameters of H010($Ba_3V_{1.8}Mo_{0.2}O_{8.1}$) in Room Temperature

Based on the structural model presented in Figure 24, the refined occupancies of Mo1 and Mo2 are 0.095 and 0.011, respectively, summing to 0.106. This results in an approximate Mo-to-V ratio of 1:9, consistent with the expected substitution level. Furthermore, in contrast to the VO_4 tetrahedra observed in the structure without substitution, Figure 24 shows that Mo^{6+} form MoO_6 octahedra in the substituted sample. This indicates that Mo substitution induces structural transformation rather than simple site substitutions.

This structural change is likely a result of the higher valence state of Mo^{6+}, which tends to attract more oxygen to stabilize its local environment. Due to the natural preference of Mo^{6+} for octahedral MoO_6, which occurs because Mo^{6+} has a d^0 configuration and exhibits a significant second-order Jahn–Teller (SOJT) effect, it can lower the electronic energy through slight distortion in an octahedral environment [90]. Furthermore, the strong covalency of the Mo–O bond and the high charge density allow for more effective distribution of electrostatic repulsion and optimization of bond length matching in octahedral coordination [91]. This coordination tendency can be observed in various structural types such as α-MoO_3, Bi_2MoO_6, and $SrMoO_3$ in oxide crystal chemistry [92]. The octahedral structure observed at the M1 site can be explained easily: as shown in Figure 25a, the Rietveld refinement results treat the same crystallographic position as one location. The local structure (the actual polyhedron) depends on whether V or Mo is located there—when V is present, it is tetrahedral; when Mo is present, the two surrounding oxygens come closer/occupy the site, increasing the coordination number to 6. Oxygen may come from movable oxygen sites or interstitial positions in adjacent layers or result from valence state adjustments of

nearby V to achieve charge and geometric stability. This is evidenced by the removal of the extra O3 shown in Figure 27: after O3 was removed and the structure was refined, the M1 site only exhibited tetrahedral structure, while the Mo at the M2 site still displayed octahedral structure with six coordination. This result indicates that the occupancy of the O3 site is closely related to the presence of Mo, with the additional coordinating oxygen providing the average structural conditions required for a stable octahedral configuration for Mo, whereas V tends to maintain a tetrahedral structure without extra oxygen coordination. This verifies the inherent preference of Mo^{6+} for octahedral environments in this system and the resultant oxygen rearrangement effect. This conclusion can be further verified through the ^{51}V MAS NMR, since there is a significant difference between the chemical shift of tetrahedral and octahedral.

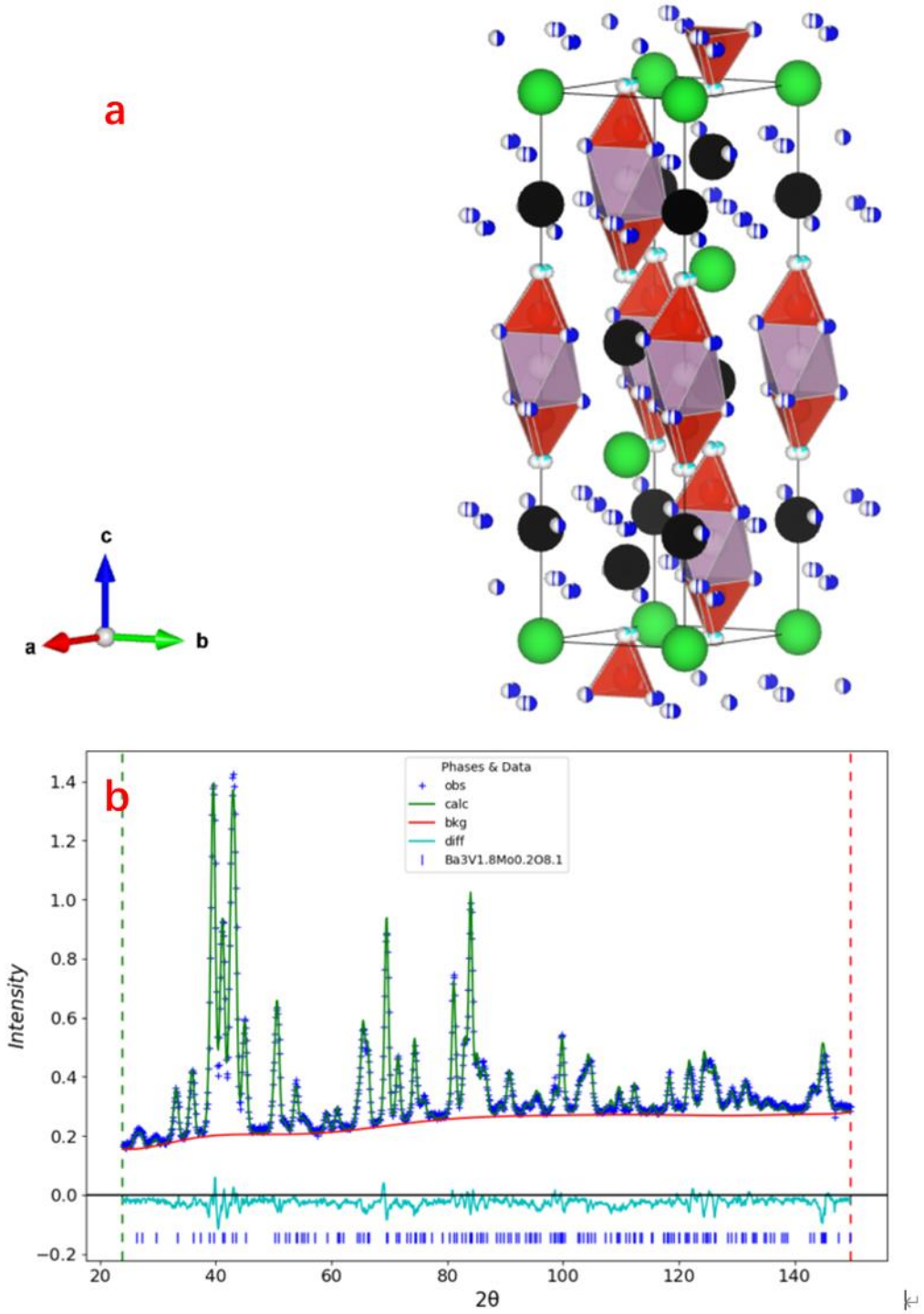

Figure 27. The Structure Model of H010($Ba_3V_{1.8}Mo_{0.2}O_{8.1}$) in Room Temperature, without O3(a) and Refinement Fir Result(b)

This average structural reconstruction also indicates the material is evolving toward a framework that may be more favorable for ionic migration. Octahedra serve as fundamental building blocks for conducting pathways in many ion-conducting materials. These octahedra may form corner- or edge-sharing networks that support ion migration, which could help improve the material's conductivity and structural stability.

Notably, as shown in Figure 28, which presents the Rietveld refinement of the neutron diffraction pattern for $Ba_3V_2O_8$ at 780 K, the MoO_6 octahedral units observed at room temperature disappear. Instead, tetrahedral MoO_4 (marked as pink) and VO_4 (marked as red) environments appear. Moreover, the refinement at high temperature no longer requires the inclusion of additional Mo and O sites (in the figure, O1 is shown in cyan, and O2—at Wyckoff site 18f—is shown in blue).

This suggests that the material undergoes a thermally driven structural simplification and reconstruction at elevated temperatures. Several explanations are plausible: first, octahedral units may lose coordinating oxygen atoms at high temperature, due oxygen migration (O3 migrates into O2), resulting in a reversion to tetrahedral geometry. Same things happen on the M1 and M2 site: thermal expansion and enhanced ionic motion at high temperatures tend to drive the structure toward a more symmetric and stress-relieved state, where the M1 becomes fully occupied and M2 becomes empty because of the migration of Mo at M2 site into M1 site. The octahedral motifs induced by Mo^{6+} may thus collapse into the MoO_4 framework.

The complete conversion to tetrahedral coordination also implies that Mo^{6+} fully substitutes for V^{5+} at high temperatures, and that the disordered or dual-site occupancy behavior disappears. This indicates a certain degree of thermal stability and reversible structural response in the material.

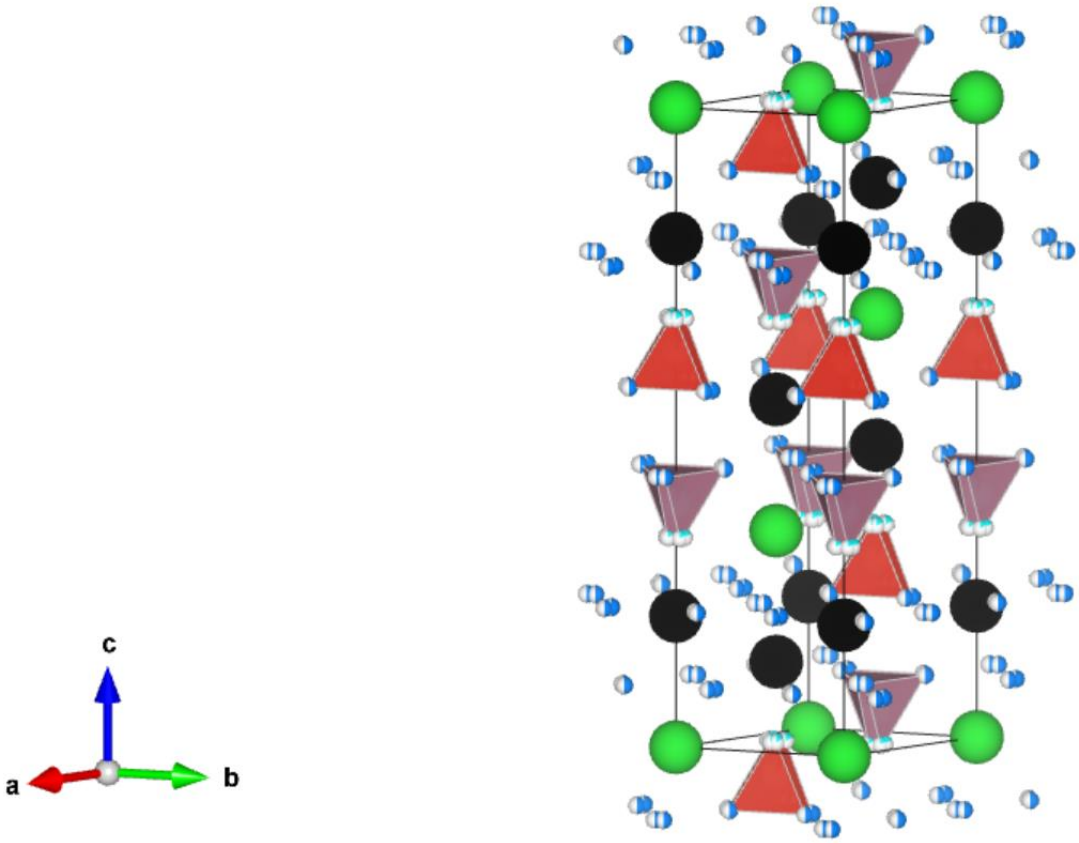

Figure 28. The Structure Model of H010($Ba_3V_{1.8}Mo_{0.2}O_{8.1}$) in 780K

It should be noted that this structural behavior is only observed in the Ba series. In the Sr series, Mo substitution does not lead to any detectable occupancy at the M2 site. This can be explained by the fact that compared to $Ba_3V_2O_8$, $Sr_3V_2O_8$ shows smaller lattice parameters (shown in Appendix A), which results in higher formation energy of interstitial oxygen. That is why MoO_6 octahedral cannot be observed in the Sr series samples. Figure 29 presents the relative occupancy ratios of M1 and M2 sites at room temperature in the Ba samples. For the Ba series, when x = 0.2 and 0.3, a portion of Mo starts to occupy the M2 site, and the occupancy increases with higher substitution levels. This indicates that the site preference of Mo may be directly influenced by the size of the A-site cation and the surrounding crystal chemical environment. Specifically, the larger ionic radius of Ba compared to Sr results in lattice expansion, as already confirmed by the Le Bail refinements in Figures 19 and 20. As a result, the M2 site in Ba-based samples offers more spatial freedom, making it easier for Mo to occupy. In contrast, the smaller Sr ion provides a more constrained environment, making it difficult for Mo to form stable octahedral coordination. Even at higher substitution levels, Mo in the Sr series remains confined to the M1 site, where it adopts a tetrahedral configuration.

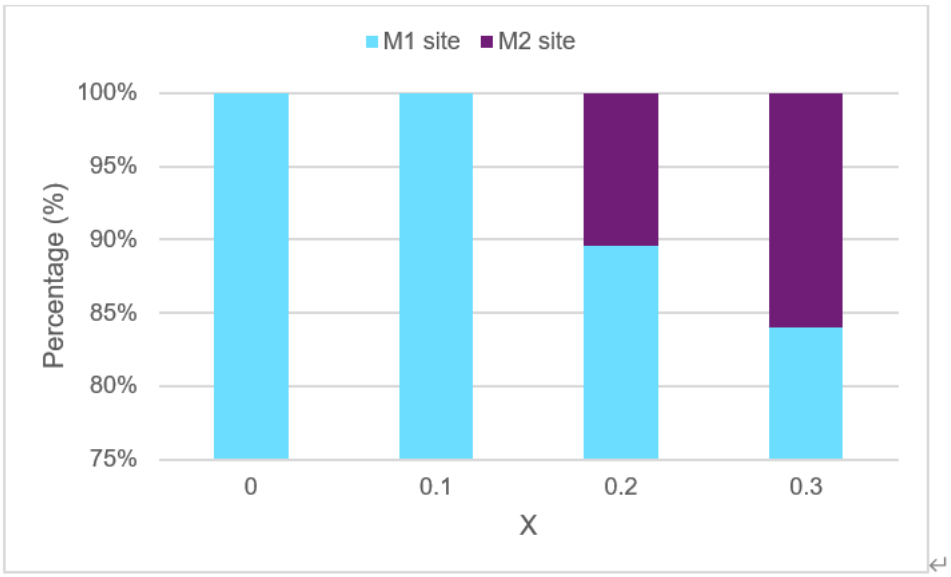

Figure 29. Relative Occupancy Ratios of M1 and M2 sites at Room Temperature in The Ba-Series

Figure 30 shows the variation in the average Z-coordinate of the M1 site with increasing Mo content in both Sr and Ba samples. With the increase of Mo substitution, both the z coordinates of Mo and V in M1 site show a significant decrease, which means a slight shift of the transition metal ions along the c-axis. This displacement is likely due to structural changes introduced by Mo substitution. Compared to V, Mo has a higher charge and slightly larger ionic radius, which may affect the coordination and lead to distortions along the c-direction. Mo also shows a preference for forming octahedral rather than tetrahedral coordination, which may further influence the lattice geometry. While most B-site cations still form VO_4 tetrahedra, the presence of some MoO_6 octahedra is enough to induce changes in the local stress field and electrostatic potential. The larger size and rigidity of MoO_6 units may cause distortion to propagate into neighboring regions, leading to a slight shift of the M1 position to accommodate overall geometric continuity and

charge balance. This substituting-induced adjustment results in the observed reduction of the M1 Z-coordinate with increasing Mo content, reflecting a weakly coupled structural response.

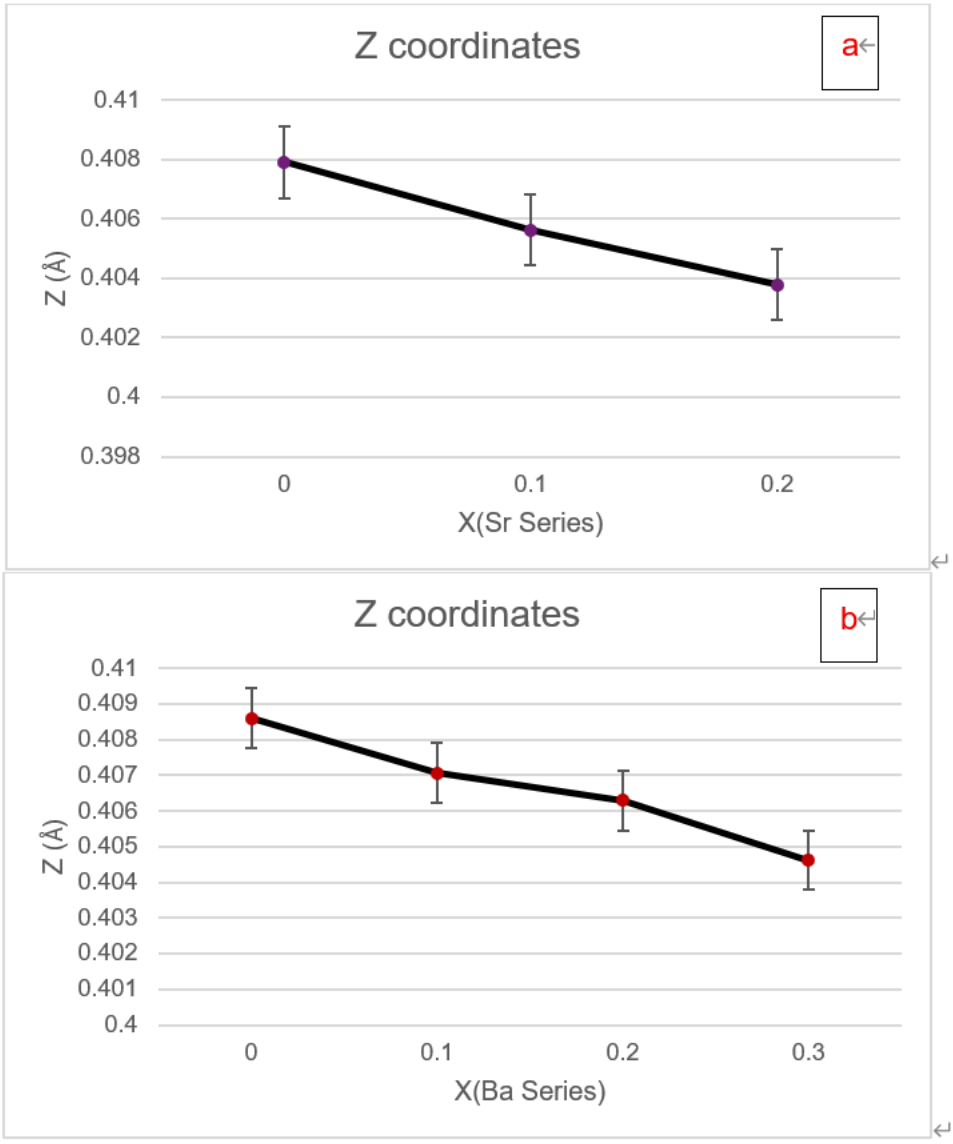

Figure 30. Average Z-coordinate of The M1 Site with Increasing Mo Content in Sr(a) and Ba(b) Samples

4.3 Fabrication of the pellets

As ceramic powders, the pressed pellets are extremely fragile. To avoid wasting valuable material, a larger quantity of $Sr_3V_2O_8$ and $Ba_3V_2O_8$, designated as H013 and H014 was synthesized first, to serve as test samples for determining the optimal pressing pressure. Table 6 presents the density results of the samples sintered under different pressures. For these tests, the pellets were heated at a rate of 150 °C per hour up to 1250 °C, held for 10 hours, and then cooled to room temperature at a rate of 300 °C per hour. It should be noted that, compared to the calcination step where the samples were held at 1100 °C for 7 hours, this increase in temperature and dwell time was intended to produce pellets with higher density.

Pressure	H013	Pressure	H014
3000lbs	85%	2250lbs	98%
4000lbs	90%	2500lbs	Cracked after the measurement of densification
4500lbs	87%	2750lbs	Cracked before sintering

Table 6. Test of The Densification of H013 and H014 with Different Pressure

After the test fabrication of the H013 and H014 pellets， as mentioned in the section 3.3, samples H015-H021 are prepared for the fabrication of the pellets. The Le Bail refinement was applied to the new powders again to check the unit cell parameters, and the Figures 20 and Figure 21 have shown the results. Similar parameters mean that the Mo substitution is reproduceable, and the new powders can be used to test the fabrication of the pellets.

Finally, a pressure of 4000 lbs was selected for preparing the Sr-series pellets, while 2250 lbs was chosen for the Ba-series pellets. For each pellet, 0.3 g of powder was used. The initial preparation conditions and the corresponding results are shown in the Figure 31.

$Sr_3V_{2-x}Mo_xO_{8+x/2}$ (0.3g, 4000lbs, 150℃/h to 1250℃ and 1250℃for 10h)		
X=0	$Sr_3V_2O_8$	90%
X=0.1	$Sr_3V_{1.9}Mo_{0.1}O_{8.05}$	88%
X=0.2	$Sr_3V_{1.8}Mo_{0.2}O_{8.1}$	94%
$Ba_3V_{2-x}Mo_xO_{8+x/2}$ (0.3g, 2250lbs, 150℃/h to 1250℃ and 1250℃ for 10h)		
X=0	$Ba_3V_2O_8$	99%
X=0.1	$Ba_3V_{1.9}Mo_{0.1}O_{8.05}$	98%
X=0.2	$Ba_3V_{1.8}Mo_{0.2}O_{8.1}$	92%
X=0.3	$Ba_3V_{1.7}Mo_{0.3}O_{8.15}$	98%

Figure 31. Densification of The First Sintering for All Selected Samples

While most of the pellets achieved the expected density, the $Sr_3V_{1.9}Mo_{0.1}O_{8.05}$ pellets did not reach the target, and the Ba-series pellets proved to be very fragile, frequently cracking when taken out of the water during the Archimedes measurement. To improve both the density and mechanical strength, PEG-400 was added as a binder. After pressing, one drop of PEG-400 was applied to each pellet using a dropper. To ensure that the PEG-400 fully penetrated the pellets and did not decompose explosively during rapid heating— which might create ‘stomata’ (pores) in the pellet

structure— the heating schedule was adjusted [93]. First, the pellets were held at 30 °C for one hour to allow complete infiltration of the PEG-400. Then, the heating rate was reduced to 30 °C per hour to ensure that the PEG decomposed slowly and thoroughly. The densities of the pellets prepared with this modified sintering procedure are shown in the Figure 32.

$Sr_3V_{2-x}Mo_xO_{8+x/2}$ (0.3g, 4000lbs, 30℃/h to 1250℃ and 1250℃for 10h)		
X=0	$Sr_3V_2O_8$	95%
X=0.1	$Sr_3V_{1.9}Mo_{0.1}O_{8.05}$	94%
X=0.2	$Sr_3V_{1.8}Mo_{0.2}O_{8.1}$	93%
$Ba_3V_{2-x}Mo_xO_{8+x/2}$ (0.3g, 2250lbs, 30℃/h to 1250℃ and 1250℃ for 10h)		
X=0	$Ba_3V_2O_8$	99%
X=0.1	$Ba_3V_{1.9}Mo_{0.1}O_{8.05}$	98%
X=0.2	$Ba_3V_{1.8}Mo_{0.2}O_{8.1}$	92%
X=0.3	$Ba_3V_{1.7}Mo_{0.3}O_{8.15}$	98%

Figure 32. Densification of The Final Sintering for All Selected Samples

In addition, it is worth mentioning that, as shown in the figure, for the pellets prepared from the Ba series powders, it can be clearly observed that with the increasing level of Mo substituting, the color of the pellets gradually darkens from the initial white (shown in Figure 33). The main reason for the color darkening is the enhanced light absorption ability of the samples, which may be attributed to three possible factors. The primary reason is that Mo substitution introduces additional oxygen ions ($O_8 \rightarrow O_{8+x/2}$) to compensate for the charge imbalance caused by Mo^{6+}. However, the excess oxygen may not be fully incorporated into the lattice, resulting in local charge imbalance in the crystal structure. In such cases, the system may tend to induce the reduction of B-site cations, i.e., $V^{5+} \rightarrow V^{4+}$ or $Mo^{6+} \rightarrow Mo^{5+}$, to neutralize the extra positive charge brought by Mo^{6+}[94]. This process leads to d0–d1 charge transfer transitions, introducing new absorption in the visible light range, which macroscopically appears as a deepening of color [95]. This phenomenon can be verified by XPS to check whether Mo^{5+} or V^{4+} species are present in the crystal. The other two reasons are less common. Firstly, Mo substitution may locally alter the density of states (DOS); if defect levels or Mo 4d states merge into the bottom of the conduction band, it can result in an effective bandgap narrowing or red-shift of the absorption edge [96]. This can be verified by UV-Vis measurements of Eg to see if there is a trend of bandgap narrowing [97]. Secondly, higher substitution levels are often accompanied by suppressed crystal growth and increased defects, which may reduce surface scattering and increase light absorption, making the color appear darker, but this is considered only a secondary reason [98].

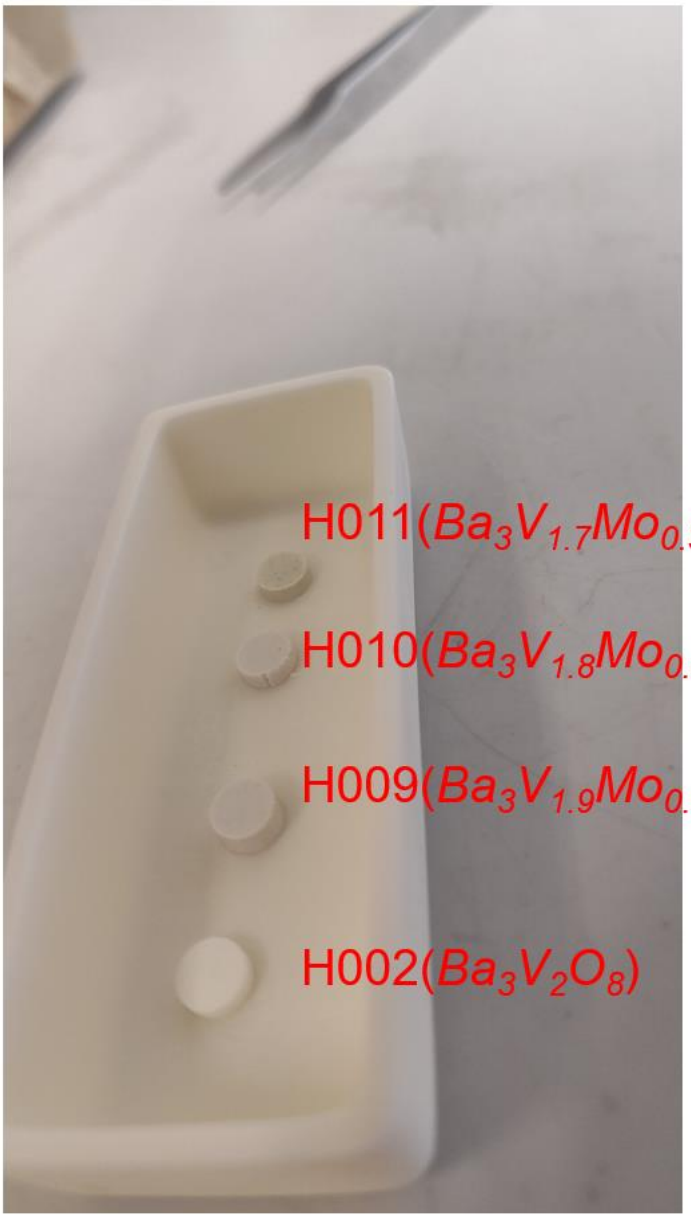

Figure 33. The Pellets after sintering gradually become darker as the degree of substitution increases.

In the oxygen/proton conductor system, the density of the sample has a decisive influence on the measurement of the true conductivity, especially when there are many pores at the grain boundaries. The poor contact between the grains will introduce additional grain boundary resistance, masking the intrinsic conduction behavior. The traditional high-temperature and long-time sintering currently used can promote grain growth to a certain extent, but it is also easy to cause uneven grain boundaries and incomplete pore closure, and high temperature and long time may induce excessive lattice rearrangement or secondary phase precipitation. As an advanced rapid densification technology, Spark Plasma Sintering (SPS) combines external pulse current, mechanical pressure and rapid heating. It can achieve ceramic preparation with a near-theoretical density at a relatively low temperature and in a very short time, while effectively controlling the grain size and avoiding abnormal growth and the formation of irregular grain boundary structure.

Subsequently, the SPS conditions (such as sintering pressure, current density, heating rate and holding time) can be systematically designed, and the changes in grain size, porosity and phase composition of the materials before and after SPS can be compared and analyzed by combining XRD and SEM characterization.

Here, in order to improve the densification of the pellets, we used the SPS to fabricate the pellets. Apart from the technique, the set up for the fabrication was also different: due to the limit of the machine, the minimum diameter of the pellets are limited to 10mm, also, because the minimum force that the machine can apply is 5kN, so the thickness of the pellets were not suggested lower than 5mm. However, 5mm is not acceptable for the conductivity test as the excessive thickness will lead to an increase in voids within the structure, thereby causing the results of the resistance test to deteriorate. Finally, we conducted three attempts using the H015 sample ($Ba_3V_2O_8$), since the pressure was much higher than the original method, temperature was reduced to 1100℃. The experiment parameters and results of the experiment are shown in Table 7. The test of densification was still done by the Archimedes method.

Thickness	Heating/Cooling Time	Holding Time	Results
2mm	5mins/5mins	20 mins	Cracked
2.5mm	10mins/10mins	20 mins	Cracked
3mm	15mins/15mins	20 mins	99.39% (partially cracked)

Table 7. Test Results of SPS

Though the densification of the last test was good enough for the pellets, the main problem was that it left a main part with an irregular shape, which was hard for applying the Pt sputtering on the surface. In the end, the pellets that have been sintered in Figure 32 were selected for the further conductivity test.

5 Conclusion

In this study, the effect of introducing Mo into $A_3V_2O_8$ (with A = Sr or Ba) on its crystal structure is explored by the us. By preparing a series of Mo-substituted samples using solid-state synthesis their structures are studied with X-ray and neutron diffraction, supported by Le Bail and Rietveld refinement. Even with a small amount of Mo added, the structure started to change. The lattice became slightly wider in the a-direction and a bit shorter along c, suggesting that the substitution introduced some uneven stress into the crystal. This is probably related to the difference in size and charge between Mo and V, and how the average structure adjusts to that.

More detailed refinements showed that Mo does not simply replace V in a one-to-one fashion. In the Ba-based compounds, Mo tends to occupy a second B-site (M2) at higher concentrations, and by replacing the V with Mo, both the tetrahedral VO_4 and Octahedral MoO_6 are observed at M1 site. This kind of structural adjustment is not observed in the Sr-based samples, likely because the smaller Sr ion leads to a more constrained framework that limits the flexibility of the lattice. The difference between the two A-site systems highlights how the chemical environment plays a role in determining site preference and structural response to substitution.

Interestingly, neutron diffraction measurements at elevated temperatures showed that the octahedral distortions introduced by Mo substitution tend to disappear, and the structure reverts to its original tetrahedral form. This observation suggests that the Mo-induced changes are not permanent and that the material shows a reversion of the hybrid 9R and palmierite units to just the palmierite units at high temperatures, which is an encouraging sign for its long-term structural stability under operating conditions.

Overall, these findings demonstrate that Mo^{6+} substitution can be used to deliberately tune the average geometry and lattice symmetry of palmierite-type oxides. The fact that Mo can occupy multiple sites and influence polyhedral connectivity may also have implications for ionic transport, though this remains to be explored further. This study provides a structural basis for future work on the functional properties of these materials and may support their development for applications in solid-state ion conductors or energy devices.

6 Outlook

This study focuses on the 9R hexagonal perovskite derivative $A_3V_2O_8$ (A = Sr, Ba) system, and achieves the regulation of the material's crystal structure through Mo substitution. Combining multiple characterization techniques such as XRD, ND and ICP-MS. However, to advance this system from basic research to more efficient, controllable and applicable ion conductors, it is still necessary to specifically solve key problems such as insufficient preparation density, insufficient average structural information, and insufficient matching between macroscopic performance and microscopic mechanisms. In order to further deepen the understanding of the mechanism of this type of layered isolated tetrahedral oxides and improve the comparability and application feasibility of experimental results, subsequent research can continue to advance from the following aspects.

After completing the characterization of the structure and the preparation of pellets, the next step to be carried out naturally is the test of the material's conductivity. Electrochemical Impedance Spectroscopy (EIS) is an AC electrochemical characterization method based on small-signal perturbation, which can be used to study charge transport, electrode interface behavior, ion migration, and electrochemical reaction kinetics in materials or electrochemical systems. Its basic principle is to apply a small-amplitude (typically 5–50 mV) sinusoidal AC voltage perturbation to the electrochemical system under a certain bias (such as open-circuit potential or a set potential) and then measure the current response of the system to this perturbation. By comparing the amplitude and phase difference between the input voltage and the output current, the magnitude and phase angle of the impedance can be obtained. The impedance is expressed in complex form:

$$\boldsymbol{Z(\omega) = Z'(\omega) + jZ''(\omega)} \quad \textbf{(10)}$$

where Z' is the fundamental part (the resistive component), Z'' is the imaginary part (the capacitive or inductive component), and ω is the angular frequency. In practice, EIS is typically performed by scanning over a wide frequency range (e.g., 10^{-2} Hz to 10^{6} Hz) to record the frequency response of the impedance, which allows different processes to be distinguished across different frequency regions. EIS results are usually presented as Nyquist plots (Cole–Cole plots) or Bode plots. To interpret the experimental results, an equivalent circuit model corresponding to the actual system is usually established. The electrolyte resistance, charge transfer resistance at the interface, interfacial capacitance, and diffusion coefficient can be obtained by fitting experimental data. By controlling the atmosphere and temperature, it is often possible to selectively measure the conductivity for specific ions: for proton conductors, measurements are typically carried out under humid conditions (such as a H_2O/air mixture) or at elevated temperatures to enhance proton transport; for oxide ion conductors, tests are usually performed under conditions with a known oxygen partial pressure (such as dry air or an O_2 atmosphere). To ensure the accuracy of the impedance test results, the tablets were first subjected to Pt sputtering treatment to form a uniform and dense metal film on the tablet surface, significantly reducing the contact resistance between the tablet surface and the electrode fixture and avoiding false contact or high contact impedance caused by rough, oxidized or porous surfaces. Meanwhile, for each pellet, tests should be conducted using oxygen, dry air and moist air respectively to comprehensively evaluate the conductivity of the material. Due to the project time limit, the conductivity test could not be completed and will be continued by subsequent researchers.

XRD and ND can efficiently obtain long-range ordered structural information of materials, but their ability to analyze local defects (such as oxygen vacancy distribution, coordination diversity, light element occupancy and local disorder) is limited, especially for the dynamic rotation behavior of isolated VO_4 tetrahedrons, the local electronic environment after substitution and its direct connection with oxygen/proton migration, there is still a lack of strong experimental evidence. Solid-state Nuclear Magnetic Resonance (NMR) (such as ^{1}H, ^{2}H, ^{17}O, ^{51}V and other nuclides) is sensitive to light elements and local structures. Combined with isotope labeling (such as enriched ^{17}O) and variable temperature testing (VT-NMR), it can quantify the rotational freedom of VO_4 units, the dynamic behavior of vacancies, and the possible occupation positions and diffusion rates of protons. Subsequently, solid-state NMR studies with multiple temperature ranges and time scales can be designed and cross-validated with BVSE/DFT simulation results to analyze the effects of Mo substitution on V–O coordination and the dynamic formation/breaking of O–H bonds, fill the gap in the analysis of local disorder and dynamic processes by diffraction methods, and form a full-scale structural-conduction coupling perspective from long-range order to local disorder.

In order to improve the interpretability of experiments and the predictability of substitution schemes, the coupling of computational methods such as first-principles calculation (DFT), molecular dynamics (AIMD), and bond valence site energy (BVSE) with experimental data can be strengthened in the future. By optimizing the structure through DFT, calculating the oxygen vacancy formation energy and the VO_4 unit rotation barrier, and combining AIMD to simulate the ion diffusion path and diffusion coefficient, the effects of different substitution concentrations and vacancy concentrations on the migration energy barrier can be quantitatively revealed at the atomic scale. Comparing the theoretical results with the experimental measurements of NMR/EIS/ND in a closed-loop data loop can effectively verify the quantitative relationship between structure-diffusion-conductance and provide a theoretical design basis for new substitution schemes and better lattice control paths.

Single Mo substitution has been shown to effectively induce the formation of oxygen vacancies and partially regulate the order of tetrahedral units. However, in the research direction of B-site metal substitution, many metal cations have been shown to significantly optimize the conductivity of oxides: such as Nb^{5+}, Ti^{6+}, W^{6+}, etc. These ions can be tried to be substituted to generate new substances for comparison, or multiple substitution (such as Mo-W, Mo-Nb co-substitution) can be introduced to further increase the vacancy concentration and enhance the rotation/connectivity of the VO_4 tetrahedron, thereby optimizing the migration channel of oxygen ions or protons. In addition, A-site or double-site co-substitution (such as the introduction of rare earth ions with smaller radius at the Sr/Ba site) can be explored to adjust the lattice tension and the arrangement of isolated VO_4 tetrahedrons, promote the formation of ion hopping paths with lower potential barriers, and combine ICP-MS to accurately determine the actual substitution content and valence distribution to verify the defect chemistry regulation effect.

Acknowledgments

Two years have passed in a flash. From the moment I first stepped into the Netherlands, this land interwoven with windmills and tulips, to now nearing the completion of my master's studies, the journey has been filled with hardships, growth, and countless warm memories and gratitude to cherish. As I near the completion of this thesis, I am filled with appreciation and extend my sincere thanks to everyone who has supported and helped me along this journey.

First of all, I sincerely thank my daily advisors, Dr. Pedro Braga Groszewicz and Abdulkadir Olatunbosun Biffo. Throughout the graduation project, you set a shining example for me with your rigorous scientific attitude and open guidance style. From determining the research direction, designing the experimental plan, to data analysis and refining the thesis, you have given me immense patience, trust, and encouragement. Through our interactions, I not only improved my research skills, but also deeply understood the critical thinking spirit and dedication that should accompany research.

I also wholeheartedly thank my joint advisor, Dr. Yan Ma. At key stages of the project, you actively coordinated experimental resources, helped me contact various facilities within the Materials Science and Engineering department, and continuously provided constructive and profound suggestions that strengthened and completed my research. I am grateful for every bit of assistance and guidance you provided despite your busy schedule.

In addition, I would like to express special thanks to the TU Delft Reactor Institute for providing valuable platforms and resources, enabling me to complete this project in a conducive research environment. The rigorous academic atmosphere and diverse communication opportunities here have provided solid support for my growth.

Thank you to every friend I encountered during these two years of study and life. Your companionship has made my days studying abroad far from lonely, encouraging each other in times of difficulties and sharing laughter together. I also thank my family back home for their unwavering support and understanding, which has been my strongest backing. Although separated by mountains and seas, your concern has always been as warm as ever, serving as the deepest source of strength on my journey forward.

This chapter of my academic journey is ending, but the knowledge, growth, and emotions I have gained will remain etched in my heart as I move towards a broader future. This writing is dedicated to all fellow travelers; I am grateful for your presence.

Bibliography

[1] Minh, N. Q. (2004). Solid oxide fuel cell technology—features and applications. *Solid State Ionics, 174*(1), 271-277. doi:https://doi.org/10.1016/j.ssi.2004.07.042

[2] Singhal, S. C. (2000). Advances in solid oxide fuel cell technology. *Solid State Ionics, 135*(1), 305-313. doi:https://doi.org/10.1016/S0167-2738(00)00452-5

[3] Steele, B. C. H., & Heinzel, A. (2001). Materials for fuel-cell technologies. *Nature, 414*(6861), 345-352. doi:10.1038/35104620

[4] Corigliano, O., Pagnotta, L., & Fragiacomo, P. (2022). On the Technology of Solid Oxide Fuel Cell (SOFC) Energy Systems for Stationary Power Generation: A Review. *14*(22), 15276.

[5] Stern, A. G. (2018). A new sustainable hydrogen clean energy paradigm. *International Journal of Hydrogen Energy, 43*(9), 4244-4255. doi:https://doi.org/10.1016/j.ijhydene.2017.12.180

[6] Ormerod, R. M. (2003). Solid oxide fuel cells. *Chemical Society Reviews, 32*(1), 17-28. doi:10.1039/B105764M

[7] Fergus, J. W. (2006). Electrolytes for solid oxide fuel cells. *Journal of Power Sources, 162*(1), 30-40. doi:https://doi.org/10.1016/j.jpowsour.2006.06.062

[8] Hoffrogge, P. W., Schneider, D., Wankmüller, F., Meffert, M., Gerthsen, D., Weber, A., . . . Wieler, M. (2023). Performance estimation by multiphase-field simulations and transmission-line modeling of nickel coarsening in FIB-SEM reconstructed Ni-YSZ SOFC anodes I: Influence of wetting angle. *Journal of Power Sources, 570*, 233031. doi:https://doi.org/10.1016/j.jpowsour.2023.233031

[9] Kim, G., Lee, S., Shin, J. Y., Corre, G., Irvine, J. T. S., Vohs, J. M., & Gorte, R. J. (2009). Investigation of the Structural and Catalytic Requirements for High-Performance SOFC Anodes Formed by Infiltration of LSCM. *Electrochemical and Solid-State Letters, 12*(3), B48. doi:10.1149/1.3065971

[10] Ruiz-Morales, J. C., Marrero-López, D., Gálvez-Sánchez, M., Canales-Vázquez, J., Savaniu, C., & Savvin, S. N. (2010). Engineering of materials for solid oxide fuel cells and other energy and environmental applications. *Energy & Environmental Science, 3*(11), 1670-1681. doi:10.1039/C0EE00166J

[11] Zhang, Q., Hou, Y., Chen, L., Wang, L., & Chou, K. (2022). Enhancement of electrochemical performance for proton conductive solid oxide fuel cell by 30%GDC-LSCF cathode. *Ceramics International, 48*(12), 17816-17827. doi:https://doi.org/10.1016/j.ceramint.2022.03.052

[12] Alvarado Flores, J. J., Ávalos Rodríguez, M. L., Alcaraz Vera, J. V., Rutiaga Quiñones, J. G., Guevara Martínez, S. J., & Zarraga, R. A. (2021). Advances in the knowledge of the double perovskites derived from the conformation and substitution of the material Sr2MgMoO6-δ as anode with potential application in SOFC cell. *International Journal of Hydrogen Energy, 46*(51), 26152-26162. doi:https://doi.org/10.1016/j.ijhydene.2021.03.030

[13] Ur Rehman, H. S., Coppola, N., Singh, A., Polverino, P., Carapella, G., Montinaro, D., . . . Maritato, L. (2025). Gadolinium-Doped Ceria Room-Temperature Sputtered Thin Barrier Layers in Large-Area Solid Oxide Fuel Cells: Influence of Their Thickness and Thickness Gradient on the Cathodic Processes. *ACS Applied Energy Materials, 8*(7), 4281-4287. doi:10.1021/acsaem.4c03180

[14] Nisar, J., Giddey, S., Kaur, G., Kulkarni, A. P., Biswas, S., Jones, L. A., & Bhargava, S. K. (2024). The effect of gadolinium-doped ceria interlayer on the oxygen reduction reaction in a LSCF cathode-ScSZ electrolyte supported IT-SOFCs. *Ionics, 30*(9), 5481-5494. doi:10.1007/s11581-024-05651-w

[15] Kuterbekov, K. A., Kabyshev, A. M., Bekmyrza, K. Z., Kubenova, M. M., Kabdrakhimova, G., Abdullayeva, I., & Ayalew, A. T. (2025). Advancements in electrolyte materials and hybrid integration for enhanced solid oxide fuel cell performance. *International Journal of Low-Carbon Technologies, 20*, 353-367. doi:10.1093/ijlct/ctaf007

[16] Goodenough, J. B. (2000). Oxide-ion conductors by design. *Nature, 404*(6780), 821-823. doi:10.1038/35009177

[17] Gu, Y.-Q., Jin, Z., Zhang, H., Xu, R.-J., Zheng, M.-J., Guo, Y.-M., . . . Jia, C.-J. (2015). Transition metal nanoparticles dispersed in an alumina matrix as active and stable catalysts for COx-free hydrogen production from ammonia. *Journal of Materials Chemistry A, 3*(33), 17172-17180. doi:10.1039/C5TA04179A

[18] Ghaemi, N., Sharifianjazi, F., Irandoost, M., Esmaeilkhanian, A., & Amini Horri, B. (2024). Electrical and microstructural characteristics of GDC electrolyte synthesised by benzoate coprecipitation for solid oxide fuel cells. *Ceramics International, 50*(21, Part A), 41780-41791. doi:https://doi.org/10.1016/j.ceramint.2024.08.031

[19] Mohammadi, A., Smirnova, A. L., & Sammes, N. M. (2008). *Mechanical Properties of LSGM as an Electrolyte for Solid Oxide Fuel Cells*. https://doi.org/10.1115/FuelCell2008-65151

[20] Ahmed, H., Adebayo, P., Ahmed, M., & Arbab, A. (2023). Hydrogen Fuel Cell Technology: Benefits, Challenges, and Future Potential. *Journal of Energy Technologies and Policy, Vol 13, No 1 (2023)*, 48-56. doi:10.7176/JETP/13-1-06

[21] Roy, D., Samanta, S., Roy, S., Smallbone, A., & Roskilly, A. P. (2024). Techno-economic analysis of solid oxide fuel cell-based energy systems for decarbonising residential power and heat in the United Kingdom. *Green Chemistry, 26*(7), 3979-3994. doi:10.1039/D3GC02645K

[22] Toonssen, R., Sollai, S., Aravind, P. V., Woudstra, N., & Verkooijen, A. H. M. (2011). Alternative system designs of biomass gasification SOFC/GT hybrid systems. *International Journal of Hydrogen Energy, 36*(16), 10414-10425. doi:https://doi.org/10.1016/j.ijhydene.2010.06.069

[23] Zhou, J., Wang, Z., Han, M., Sun, Z., & Sun, K. (2022). Optimization of a 30 kW SOFC combined heat and power system with different cycles and hydrocarbon fuels. *International Journal of Hydrogen Energy, 47*(6), 4109-4119. doi:https://doi.org/10.1016/j.ijhydene.2021.11.049

[24] Mehran, M. T., Khan, M. Z., Song, R.-H., Lim, T.-H., Naqvi, M., Raza, R., . . . Hanif, M. B. (2023). A comprehensive review on durability improvement of solid oxide fuel cells for commercial stationary power generation systems. *Applied Energy, 352*, 121864. doi:https://doi.org/10.1016/j.apenergy.2023.121864

[25] Tejuca, L. G., Fierro, J. L. G., & Tascón, J. M. D. (1989). Structure and Reactivity of Perovskite-Type Oxides. In D. D. Eley, H. Pines, & P. B. Weisz (Eds.), *Advances in Catalysis* (Vol. 36, pp. 237-328): Academic Press.

[26] Bennett, J. W., Grinberg, I., & Rappe, A. M. (2009). Effect of substituting of S for O: The sulfide perovskite ${\text{BaZrS}}_{3}$ investigated with density functional theory. *Physical Review B, 79*(23), 235115. doi:10.1103/PhysRevB.79.235115

[27] Mera, A., & Rehman, M. A. (2024). First-principles investigation for the hydrogen storage properties of AeSiH3 (Ae = Li, K, Na, Mg) perovskite-type hydrides. *International Journal of Hydrogen Energy, 50*, 1435-1447. doi:https://doi.org/10.1016/j.ijhydene.2023.09.286

[28] Bi, J., Yang, S., Zhong, S., Wang, J.-Q., Fan, C., Chen, X., & Liu, Y. (2017). An insight into the effects of B-site transition metals on the activity, activation effect and stability of perovskite oxygen electrodes for solid oxide electrolysis cells. *Journal of Power Sources, 363*, 470-479. doi:https://doi.org/10.1016/j.jpowsour.2017.07.118

[29] Devi, C. S., J., O., Rajani, M. A., S., K. G., & and Prasad, G. (2020). Influence of distortions and tolerance factor on the structure of ABO3 type perovskites and complex perovskites. *Ferroelectrics, 554*(1), 172-186. doi:10.1080/00150193.2019.1684759

[30] Bhalla, A. S., Ruyan, G., & and Roy, R. (2000). The perovskite structure—a review of its role in ceramic science and technology. *Materials Research Innovations, 4*(1), 3-26. doi:10.1007/s100190000062

[31] Roy, P., Ghosh, A., Barclay, F., Khare, A., & Cuce, E. (2022). Perovskite Solar Cells: A Review of the Recent Advances. *Coatings, 12*(8). doi:10.3390/coatings12081089

[32] Lehmann, F., Franz, A., Többens, Daniel M., Levcenco, S., Unold, T., Taubert, A., & Schorr, S. (2019). The phase diagram of a mixed halide (Br, I) hybrid perovskite obtained by synchrotron X-ray diffraction. *RSC Advances, 9*(20), 11151-11159. doi:10.1039/C8RA09398A

[33] Wang, X., Ling, Y., Lian, X., Xin, Y., Dhungana, K. B., Perez-Orive, F., . . . Gao, H. (2019). Suppressed phase separation of mixed-halide perovskites confined in endotaxial matrices. *Nature Communications, 10*(1), 695. doi:10.1038/s41467-019-08610-6

[34] Lang, L., Yang, J.-H., Liu, H.-R., Xiang, H. J., & Gong, X. G. (2014). First-principles study on the electronic and optical properties of cubic ABX3 halide perovskites. *Physics Letters A, 378*(3), 290-293. doi:https://doi.org/10.1016/j.physleta.2013.11.018

[35] Stranks, S. D., & Snaith, H. J. (2015). Metal-halide perovskites for photovoltaic and light-emitting devices. *Nature Nanotechnology, 10*(5), 391-402. doi:10.1038/nnano.2015.90

[36] Herz, L. M. (2016). Charge-Carrier Dynamics in Organic-Inorganic Metal Halide Perovskites. *67*(Volume 67, 2016), 65-89. doi:https://doi.org/10.1146/annurev-physchem-040215-112222

[37] Dong, Q., Fang, Y., Shao, Y., Mulligan, P., Qiu, J., Cao, L., & Huang, J. (2015). Electron-hole diffusion lengths > 175 μm in solution-grown CH₃NH₃PbI₃ single crystals. *347*(6225), 967-970. doi:doi:10.1126/science.aaa5760

[38] Xing, G., Mathews, N., Sun, S., Lim, S. S., Lam, Y. M., Grätzel, M., . . . Sum, T. C. (2013). Long-Range Balanced Electron- and Hole-Transport Lengths in Organic-Inorganic CH₃NH₃PbI₃. *342*(6156), 344-347. doi:doi:10.1126/science.1243167

[39] Tsurusawa, H., Russo, J., Leocmach, M., & Tanaka, H. (2017). Formation of porous crystals via viscoelastic phase separation. *Nature Materials, 16*(10), 1022-1028. doi:10.1038/nmat4945

[40] Shi, D., Adinolfi, V., Comin, R., Yuan, M., Alarousu, E., Buin, A., . . . Bakr, O. M. (2015). Low trap-state density and long carrier diffusion in organolead trihalide perovskite single crystals. *347*(6221), 519-522. doi:doi:10.1126/science.aaa2725

[41] Yin, W.-J., Shi, T., & Yan, Y. (2014). Unique Properties of Halide Perovskites as Possible Origins of the Superior Solar Cell Performance. *26*(27), 4653-4658. doi:https://doi.org/10.1002/adma.201306281

[42] Mahato, N., Banerjee, A., Gupta, A., Omar, S., & Balani, K. (2015). Progress in material selection for solid oxide fuel cell technology: A review. *Progress in Materials Science, 72*, 141-337. doi:https://doi.org/10.1016/j.pmatsci.2015.01.001

[43] Hussain, S., & Yangping, L. (2020). Review of solid oxide fuel cell materials: cathode, anode, and electrolyte. *Energy Transitions, 4*(2), 113-126. doi:10.1007/s41825-020-00029-8

[44] Ni, M., Leung, M. K. H., Leung, D. Y. C., & Sumathy, K. (2007). A review and recent developments in photocatalytic water-splitting using TiO2 for hydrogen production. *Renewable and Sustainable Energy Reviews, 11*(3), 401-425. doi:https://doi.org/10.1016/j.rser.2005.01.009

[45] Adler, S. B. (2004). Factors Governing Oxygen Reduction in Solid Oxide Fuel Cell Cathodes. *Chemical Reviews, 104*(10), 4791-4844. doi:10.1021/cr020724o

[46] Gao, Z., Mogni, L. V., Miller, E. C., Railsback, J. G., & Barnett, S. A. (2016). A perspective on low-temperature solid oxide fuel cells. *Energy & Environmental Science, 9*(5), 1602-1644. doi:10.1039/C5EE03858H

[47] Yashima, M., Tsujiguchi, T., Sakuda, Y., Yasui, Y., Zhou, Y., Fujii, K., . . . Skinner, S. J. (2021). High oxide-ion conductivity through the interstitial oxygen site in Ba7Nb4MoO20-based hexagonal perovskite related oxides. *Nature Communications, 12*(1), 556. doi:10.1038/s41467-020-20859-w

[48] Andreev, R. D., & Animitsa, I. E. (2025). Hydration Processes of the Proton-Conducting Hexagonal Perovskites Ba7In6–xYxAl2O19. *The Journal of Physical Chemistry C, 129*(1), 744-753. doi:10.1021/acs.jpcc.4c06688

[49] Haavik, C., Ottesen, E. M., Nomura, K., Kilner, J. A., & Norby, T. (2004). Temperature dependence of oxygen ion transport in Sr+Mg-substituted LaGaO3 (LSGM) with varying grain sizes. *Solid State Ionics, 174*(1), 233-243. doi:https://doi.org/10.1016/j.ssi.2004.07.033

[50] Shi, H., Su, C., Ran, R., Cao, J., & Shao, Z. (2020). Electrolyte materials for intermediate-temperature solid oxide fuel cells. *Progress in Natural Science: Materials International, 30*(6), 764-774. doi:https://doi.org/10.1016/j.pnsc.2020.09.003

[51] Fop, S., Dawson, J. A., Tawse, D. N., Skellern, M. G., Skakle, J. M. S., & McLaughlin, A. C. (2022). Proton and Oxide Ion Conductivity in Palmierite Oxides. *Chemistry of Materials, 34*(18), 8190-8197. doi:10.1021/acs.chemmater.2c01218

[52] Glazer, A. (1972). The classification of tilted octahedra in perovskites. *Acta Crystallographica Section B, 28*(11), 3384-3392. doi:doi:10.1107/S0567740872007976

[53] Haertling, G. H. (1999). Ferroelectric Ceramics: History and Technology. *Journal of the American Ceramic Society, 82*(4), 797-818. doi:https://doi.org/10.1111/j.1151-2916.1999.tb01840.x

[54] Cascos, V., Troncoso, L., Alonso, J. A., & Fernández-Díaz, M. T. (2017). Design of new Ga-doped SrMoO3 perovskites performing as anode materials in SOFC. *Renewable Energy, 111*, 476-483. doi:https://doi.org/10.1016/j.renene.2017.04.023

[55] Woodward, P. (1997). Octahedral Tilting in Perovskites. I. Geometrical Considerations. *Acta Crystallographica Section B, 53*(1), 32-43. doi:doi:10.1107/S0108768196010713

[56] Wang, M., Hu, H., Lin, S., Yang, P., & Yang, D. (2023). *Prediction of perovskite structures and thermodynamic stabilities from structural factors*.

[57] King, G., & Woodward, P. M. (2010). Cation ordering in perovskites. *Journal of Materials Chemistry, 20*(28), 5785-5796. doi:10.1039/B926757C

[58] Saxena, P., & Mishra, A. (2021). Structural and electrical properties of YMnO3 manganites: Influence of Cr ion doping. *Journal of Solid State Chemistry, 301*, 122364. doi:https://doi.org/10.1016/j.jssc.2021.122364

[59] Andreev, R., & Animitsa, I. (2023). Transport Properties of Intergrowth Structures Ba5In2Al2ZrO13 and Ba7In6Al2O19. *Applied Sciences, 13*(6). doi:10.3390/app13063978

[60] Fop, S., Dawson, J. A., Fortes, A. D., Ritter, C., & McLaughlin, A. C. (2021). Hydration and Ionic Conduction Mechanisms of Hexagonal Perovskite Derivatives. *Chemistry of Materials, 33*(12), 4651-4660. doi:10.1021/acs.chemmater.1c01141

[61] Nguyen, L. T., & Cava, R. J. (2021). Hexagonal Perovskites as Quantum Materials. *Chemical Reviews, 121*(5), 2935-2965. doi:10.1021/acs.chemrev.0c00622

[62] Andreev, R., Korona, D., Anokhina, I., & Animitsa, I. (2022). Proton and Oxygen-Ion Conductivities of Hexagonal Perovskite Ba5In2Al2ZrO13. *Materials, 15*(11). doi:10.3390/ma15113944

[63] Van Aken, B., Palstra, T., Filippetti, A., & Spaldin, N. (2004). The Origin of Ferroelectricity in Magnetoelectric YMnO3. *Nature materials, 3*, 164-170. doi:10.1038/nmat1080

[64] Ishihara, T., Matsuda, H., & Takita, Y. J. J. o. t. A. c. s. (1994). Doped LaGaO3 perovskite type oxide as a new oxide ionic conductor. *116*(9), 3801-3803.

[65] Kreuer, K. D. (2003). Proton-Conducting Oxides. *33*(Volume 33, 2003), 333-359. doi:https://doi.org/10.1146/annurev.matsci.33.022802.091825

[66] Zahra, T., Bashir, S., Pershaanaa, M., Prasankumar, T., Hina, M., Ramesh, S., & Ramesh, K. (2025). Perovskite oxides for energy storage: A review on synthesis, properties and supercapacitor performance. *Journal of Energy Storage, 120*, 116434. doi:https://doi.org/10.1016/j.est.2025.116434

[67] Jia, Y. Q. (1991). Crystal radii and effective ionic radii of the rare earth ions. *Journal of Solid State Chemistry, 95*(1), 184-187. doi:https://doi.org/10.1016/0022-4596(91)90388-X

[68] Shannon, R. D. (1976). Revised effective ionic radii and systematic studies of interatomic distances in halides and chalcogenides. *Acta Crystallographica Section A, 32*(5), 751-767. doi:https://doi.org/10.1107/S0567739476001551

[69] Lee, E., Harris, R. A., Terblans, J. J., Coetsee, E., Kumar, V., & Swart, H. C. (2024). Preparation of SrVO3 by annealing of Sr2V2O7 in a reducing atmosphere. *Chemical Physics Impact, 9*, 100715. doi:https://doi.org/10.1016/j.chphi.2024.100715

[70] Hu, P., Hu, P., Vu, T. D., Li, M., Wang, S., Ke, Y., . . . Long, Y. (2023). Vanadium Oxide: Phase Diagrams, Structures, Synthesis, and Applications. *Chemical Reviews, 123*(8), 4353-4415. doi:10.1021/acs.chemrev.2c00546

[71] Enneti, R. K., & Wolfe, T. A. (2012). Agglomeration during reduction of MoO3. *International Journal of Refractory Metals and Hard Materials, 31*, 47-50. doi:https://doi.org/10.1016/j.ijrmhm.2011.09.004

[72] Wirtz, G. P., Sis, L. B., & Wheeler, J. S. (1975). Sublimation of MoO3 from WO3 MoO3 catalysts during the oxidation of toluene. *Journal of Catalysis, 38*(1), 196-205. doi:https://doi.org/10.1016/0021-9517(75)90078-0

[73] Jalil, M., Khan, M., Mandal, S., Chowdhury, F. U. Z., Hossain, M. M., Jana, D., . . . Uddin, M. (2022). *Impact of reaction temperatures on the particle size of V2O5 synthesized by facile hydrothermal technique and their auspicious photocatalytic performance in dye degradation*.

[74] Chen, Y., Chen, C., Chen, W., Liu, H., & Zhu, J. (2015). Influence of thermal-decomposition temperatures on structures and properties of V2O5 as cathode materials for lithium ion battery. *Progress in Natural Science: Materials International, 25*(1), 42-46. doi:https://doi.org/10.1016/j.pnsc.2015.01.015

[75] Chen, X., de Boer, R. M., Kosari, A., van Gog, H., & van Huis, M. A. (2023). Thermal Reduction of MoO3 Particles and Formation of MoO2 Nanosheets Monitored by In Situ Transmission Electron Microscopy. *The Journal of Physical Chemistry C, 127*(43), 21387-21398. doi:10.1021/acs.jpcc.3c05159

[76] Font, F., Protas, B., Richardson, G., & Foster, J. M. (2018). Binder migration during drying of lithium-ion battery electrodes: Modelling and comparison to experiment. *Journal of Power Sources, 393*, 177-185. doi:https://doi.org/10.1016/j.jpowsour.2018.04.097

[77] Liu, W., Midya, J., Kappl, M., Butt, H. J., & Nikoubashman, A. (2019). Segregation in Drying Binary Colloidal Droplets. *ACS Nano, 13*(5), 4972-4979. doi:10.1021/acsnano.9b00459

[78] Piroird, K., Lazarus, V., Gauthier, G., Lesaine, A., Bonamy, D., & Rountree, C. L. (2016). Role of evaporation rate on the particle organization and crack patterns obtained by drying a colloidal layer. *Europhysics Letters, 113*(3), 38002. doi:10.1209/0295-5075/113/38002

[79] Okamoto, Y., Umeno, S., Arima, Y., Nakai, K., Takahashi, T., Uchikawa, K., . . . Uchijima, T. (1998). A study on the preparation of supported metal oxide catalysts using JRC-reference catalysts. I. Preparation of a molybdena–alumina catalyst. Part 3. Drying process. *Applied Catalysis A: General, 170*(2), 343-357. doi:https://doi.org/10.1016/S0926-860X(98)00066-0

[80] Lotnyk, A., Senz, S., & Hesse, D. (2007). Thin-film solid-state reactions of solid BaCO3 and BaO vapor with (100) rutile substrates. *Acta Materialia, 55*(8), 2671-2681. doi:https://doi.org/10.1016/j.actamat.2006.12.022

[81] Huang, D., Huang, J., Zhang, Y., Fan, Y., & Hu, P. (2023). Short-Process Preparation of High-Purity V2O5 from Shale Acid Leaching Solution via Chlorination. *Processes, 11*(4). doi:10.3390/pr11041270

[82] Grote, R., Zhao, M., Shuller-Nickles, L., Amoroso, J., Gong, W., Lilova, K., . . . Brinkman, K. S. (2019). Compositional control of tunnel features in hollandite-based ceramics: structure and stability of (Ba,Cs)1.33(Zn,Ti)8O16. *Journal of Materials Science, 54*(2), 1112-1125. doi:10.1007/s10853-018-2904-1

[83] Wenda, E., & Bielański, A. (2008). The phase diagram of V2O5-MoO3-Ag2O system: Part IV. Molybdenum-rich part of the diagram. *Journal of Thermal Analysis and Calorimetry, 92*(3), 931-937. doi:https://doi.org/10.1007/s10973-007-8340-0

[84] Silva, I. F., Klimkiewicz, M., & Eser, S. (1998). An Environmental Scanning Electron Microscopy Study of Activated Charcoal Gasification Catalyzed by MoO3 in Air and in Oxygen and by a Eutectic Alloy of MoO3 and V2O5 in Air. *Energy & Fuels, 12*(3), 554-562. doi:10.1021/ef970174a

[85] Xia, L., Xie, J., & Hu, W. (2022). Locally-ordered A-site vacancy assisted photoluminescence enhancement in simply rare-earth doped perovskite oxide. *Materials Advances, 3*(23), 8608-8615. doi:10.1039/D2MA00843B

[86] Liu, X., Cao, D., Yang, T., Li, H., Ge, H., Ramos, M., . . . Wen, X.-D. (2017). Insight into the structure and energy of Mo27SxOy clusters. *RSC Advances, 7*(16), 9513-9520. doi:10.1039/C6RA26264C

[87] Meng, J. (2025). *Understanding and Design of Interstitial Oxygen Conductors*.

[88] Ou, S., Li, Z., You, Y., Wang, L., Xu, J., & Yuan, M. (2024). Effect of Mo6+ doping on the structure and electrochemical properties of spinel-type LiMn2O4 cathode materials. *Particuology, 94*, 146-157. doi:https://doi.org/10.1016/j.partic.2024.07.020

[89] Chimitova, O., Atuchin, V., Bazarov, B., Molokeev, M., & Bazarova, Z. (2013). The Formation and Structural Parameters of new Double Molybdates RbLn(MoO4)2 (Ln = Pr, Nd, Sm, Eu). *Proceedings of SPIE - The International Society for Optical Engineering*, 87711A-87711A. doi:10.1117/12.2017816

[90] Murugan, C., Soundarya Mary, A., Murugan, P., & Pandikumar, A. (2023). Enhanced Photoelectrocatalytic Water Splitting in Bi2Mo1–xWxO6 Solid Solutions: Understanding the Atomic Level Mechanism from the Experimental and First-Principles Approach. *ACS Applied Energy Materials, 6*(16), 8410-8421. doi:10.1021/acsaem.3c01151

[91] Frenking, G., Wichmann, K., Fröhlich, N., Loschen, C., Lein, M., Frunzke, J., & Rayón, V. c. M. (2003). Towards a rigorously defined quantum chemical analysis of the chemical bond in donor–acceptor complexes. *Coordination Chemistry Reviews, 238-239*, 55-82. doi:https://doi.org/10.1016/S0010-8545(02)00285-0

[92] Alam, M. H., Chowdhury, S., Roy, A., Wu, X., Ge, R., Rodder, M. A., . . . Akinwande, D. (2022). Wafer-Scalable Single-Layer Amorphous Molybdenum Trioxide. *ACS Nano, 16*(3), 3756-3767. doi:10.1021/acsnano.1c07705

[93] Glastrup, J. (1996). Degradation of polyethylene glycol. A study of the reaction mechanism in a model molecule: Tetraethylene glycol. *Polymer Degradation and Stability, 52*(3), 217-222. doi:https://doi.org/10.1016/0141-3910(95)00225-1

[94] Zhang, M., Wu, J., Hou, J., & Yang, J. (2013). Molybdenum and Nitrogen Co-Doped Titanium Dioxide Nanotube Arrays with Enhanced Visible Light Photocatalytic Activity. *Science of Advanced Materials, 5*(6), 535-541. doi:10.1166/sam.2013.1488

[95] He, T., & Yao, J. (2006). Photochromism in composite and hybrid materials based on transition-metal oxides and polyoxometalates. *Progress in Materials Science, 51*(6), 810-879. doi:https://doi.org/10.1016/j.pmatsci.2005.12.001

[96] Ansari, S. M., Taha, I., Han, X., Anjum, D. H., Mohammad, B., Amrane, N., . . . Aldosari, H. M. (2023). Influence of molybdenum doping on the structural, electrical, and optical properties of germanium telluride thin films. *Journal of Materials Research and Technology, 24*, 2538-2549. doi:https://doi.org/10.1016/j.jmrt.2023.03.172

[97] Khan, M., Xu, J., Chen, N., & Cao, W. (2012). Electronic and optical properties of pure and Mo doped anatase TiO2 using GGA and GGA+U calculations. *Physica B: Condensed Matter, 407*, 3610–3616. doi:10.1016/j.physb.2012.05.037

[98] Nazim, M., & Kim, J. H. (2020). Controlled Size Growth of Thermally Stable Organometallic Halide Perovskite Microrods: Synergistic Effect of Dual-Doping, Lattice Strain Engineering, Antisolvent Crystallization, and Band Gap Tuning Properties. *ACS Omega, 5*(26), 16106-16119. doi:10.1021/acsomega.0c01667

Appendix A

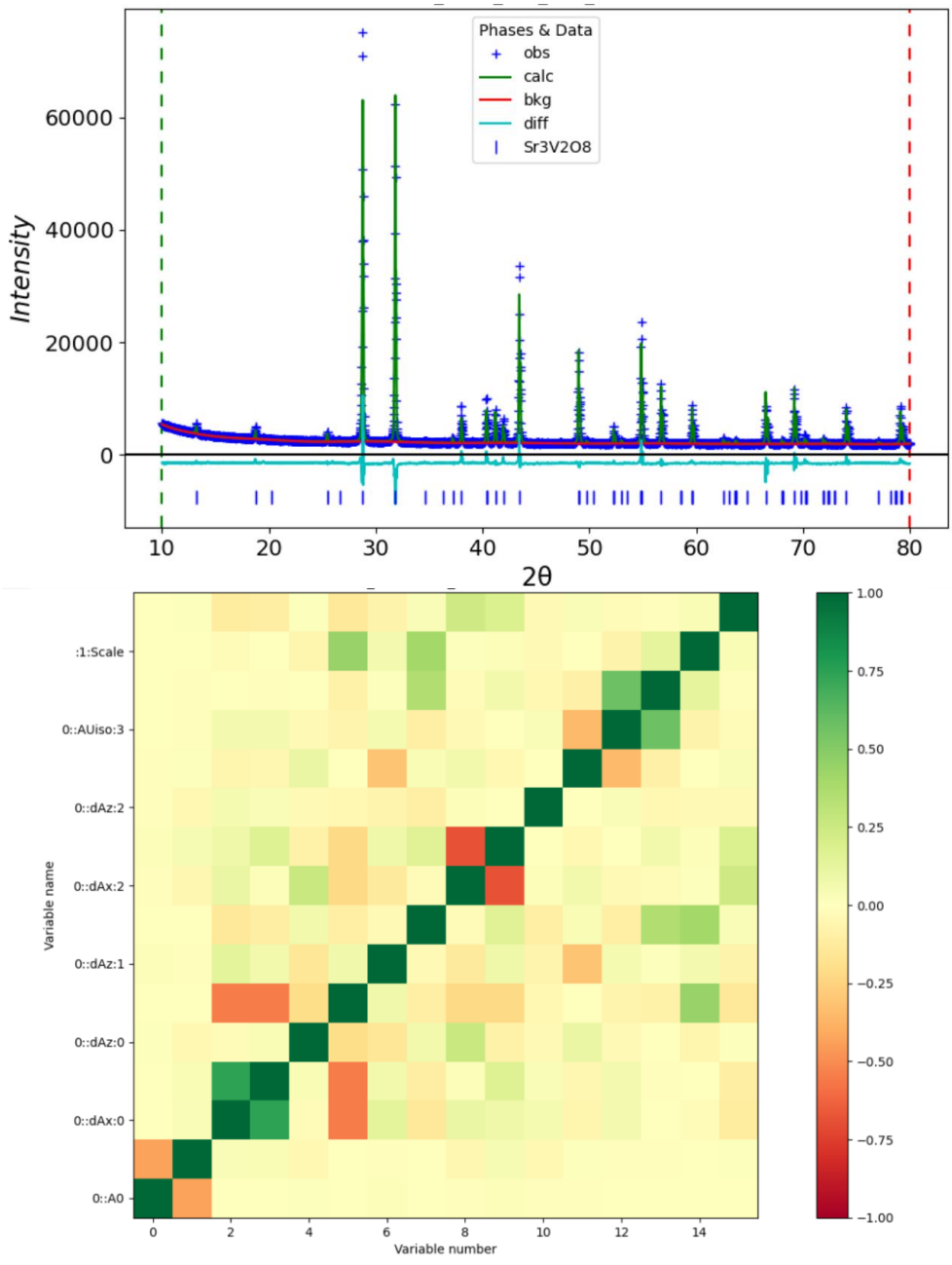

Phase $Sr_3V_2O_8$ from H001 at Room Temperature	
wR	6.222
GOF	3.81
Reduced chi**2	14.51
Space Group	R-3 m h
Unit Cell parameters	a= 5.61925, c= 20.10498

Appendix A1a. The Combined Refinement Results of H001($Sr_3V_2O_8$) at Room Temperature

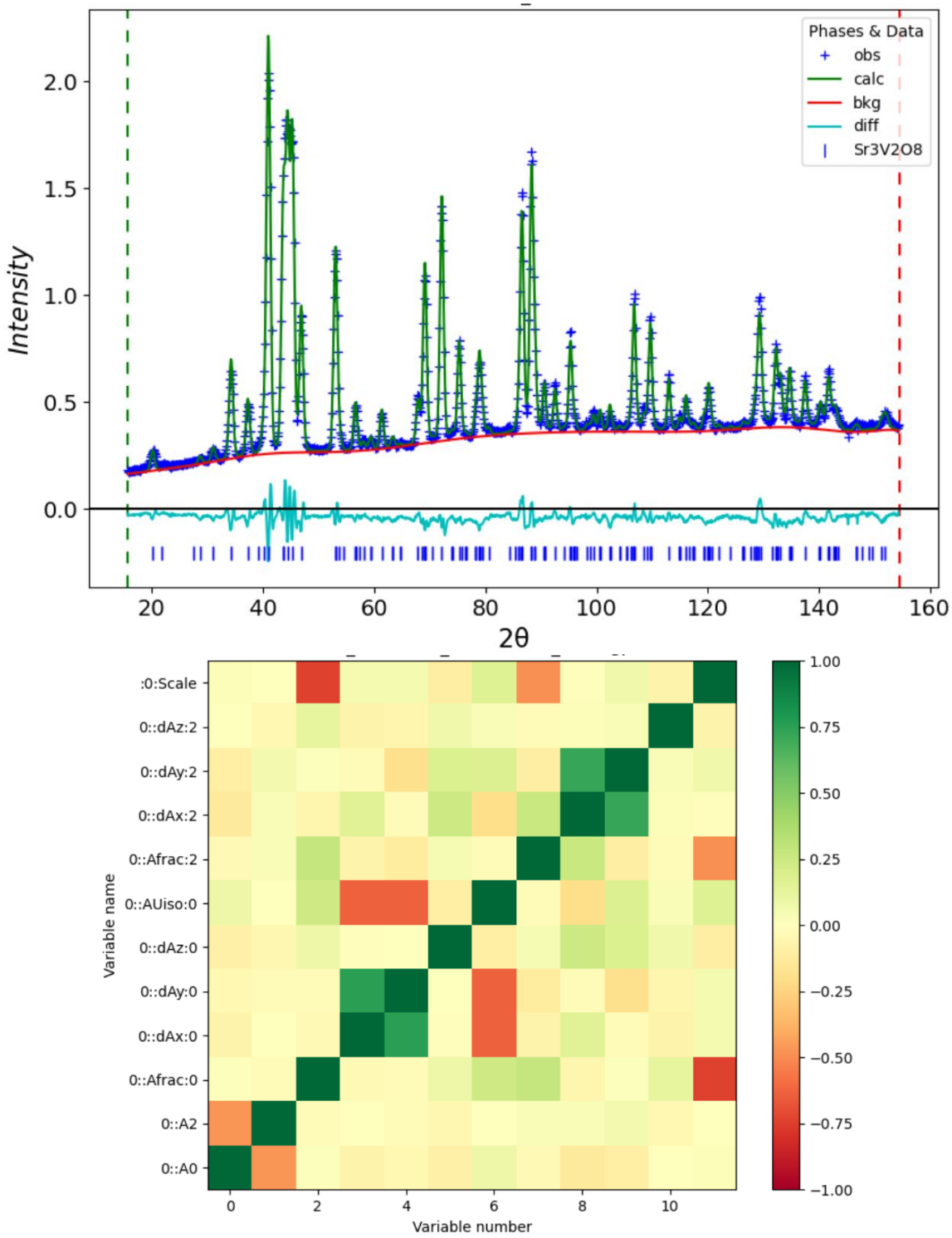

Refined Parameters Refined Parameters of Phase $Sr_3V_2O_8$ from H001 at 780K	
wR	4.450
GOF	4.31
Reduced chi**2	18.55
Space Group	R-3 m h
Unit Cell parameters	a= 5.66468, c= 20.18835

Appendix A1b. The Neutron Refinement Results of H001($Sr_3V_2O_8$) at 780K

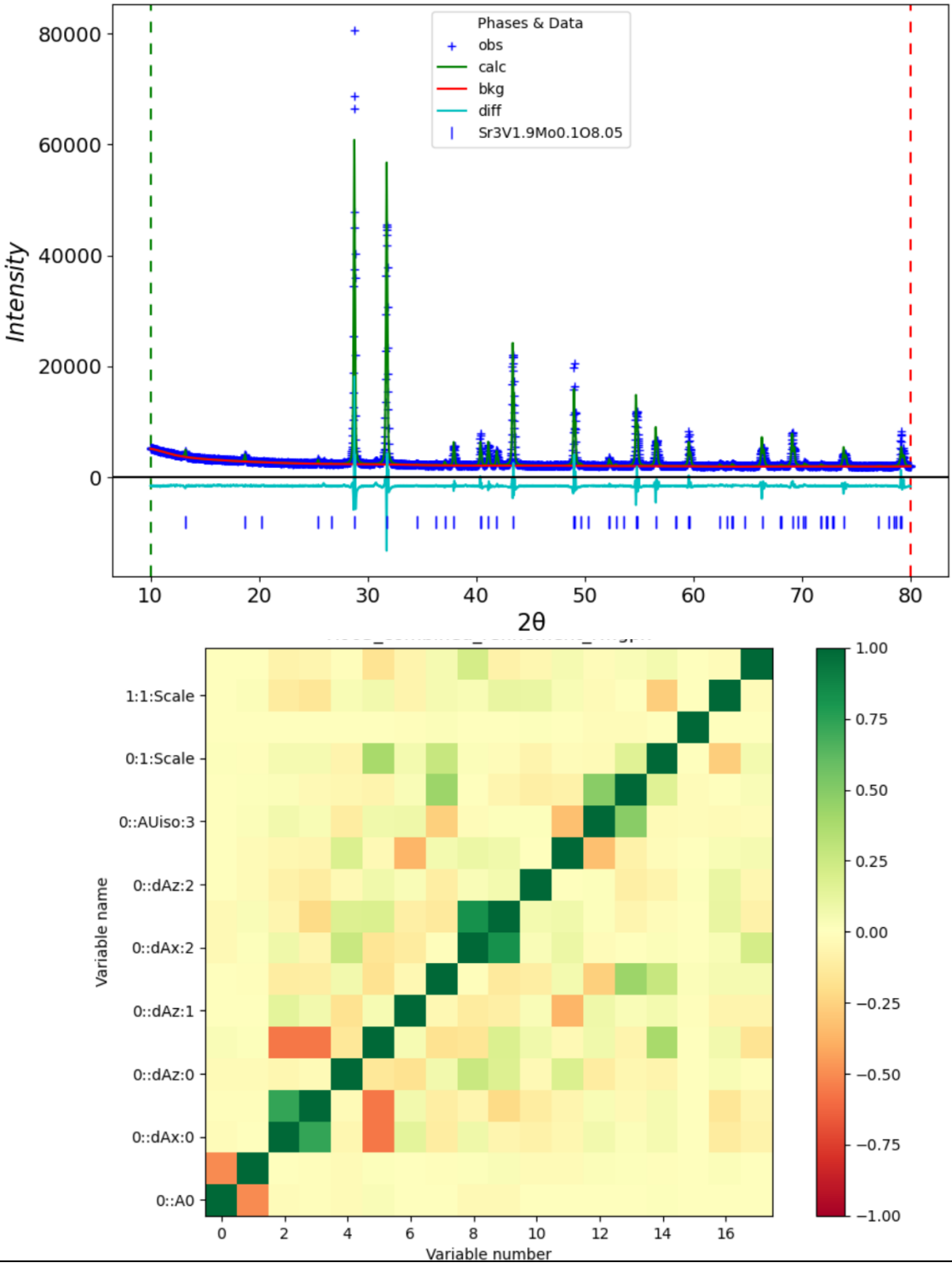

Refined Parameters Refined Parameters of Phase $Sr_3V_{1.9}Mo_{0.1}O_{8.05}$ from H003 at Room Temperature	
wR	**8.351**
GOF	**4.48**
Reduced chi2**	**18.04**
Space Group	**R-3 m h**
Unit Cell parameters	**a= 5.63498, c= 20.08599**

Appendix A2a. The Combined Refinement Results of H003($Sr_3V_{1.9}Mo_{0.1}O_{8.05}$) at Room Temperature

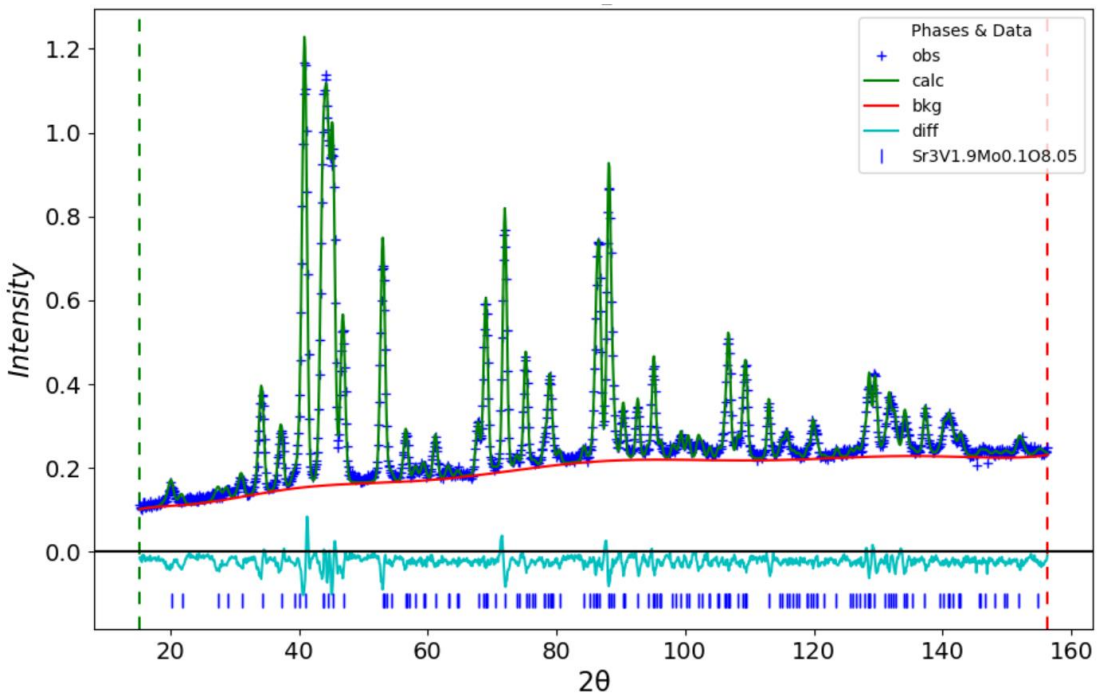

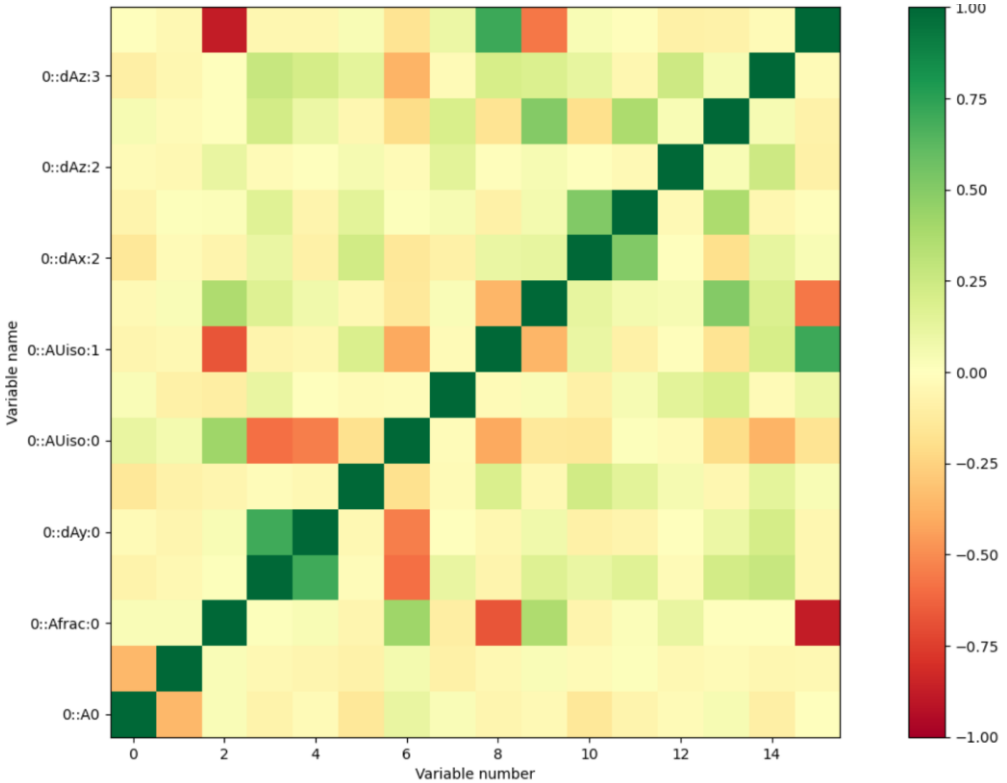

Refined Parameters Refined Parameters of Phase $Sr_3V_{1.9}Mo_{0.1}O_{8.05}$ from H003 at 780K	
wR	4.398
GOF	2.51
Reduced chi**2	6.28
Space Group	R-3 m h
Unit Cell parameters	a= 5.68195, c= 20.187

Appendix A2b. The Neutron Refinement Results of H003($Sr_3V_{1.9}Mo_{0.1}O_{8.05}$) at 780K

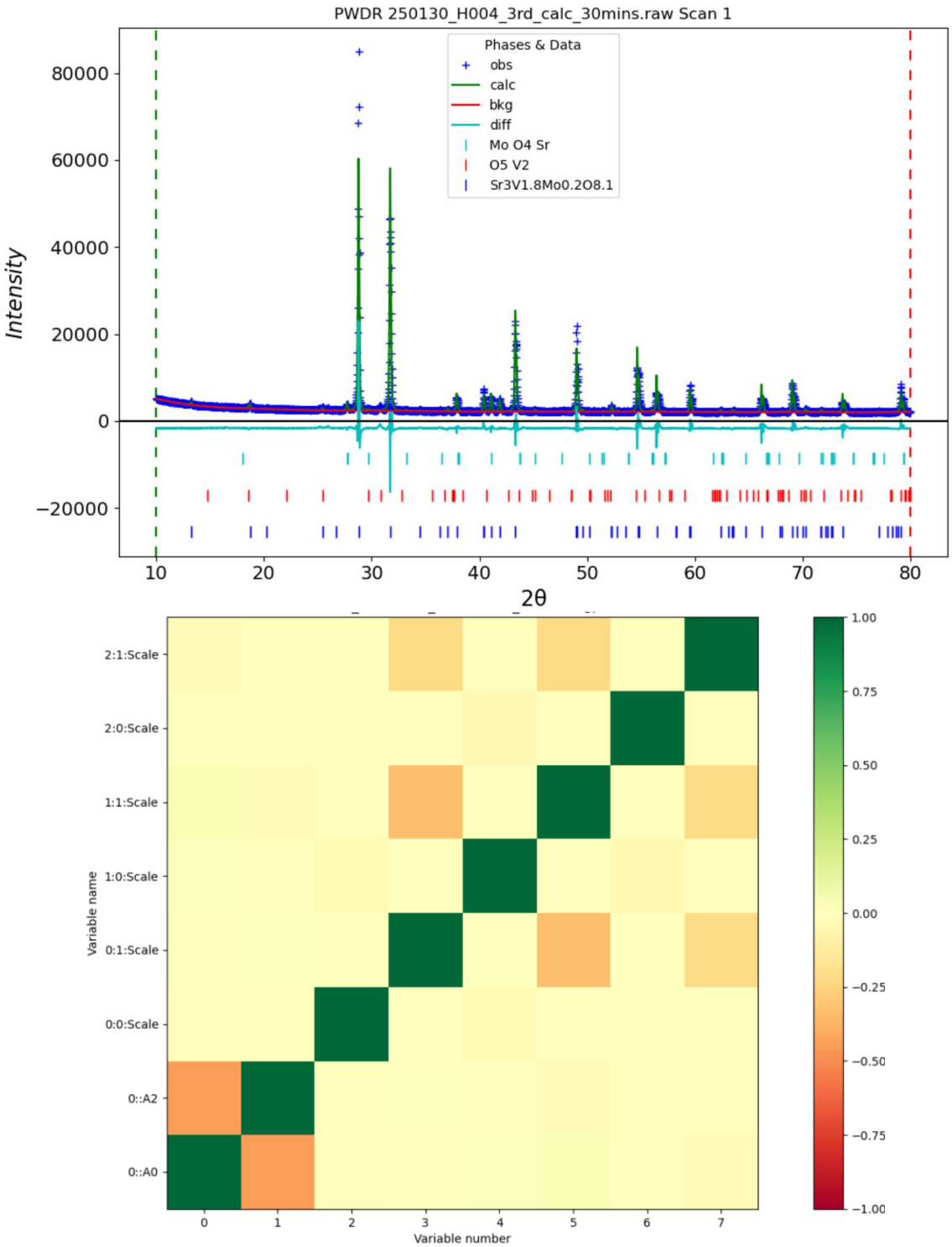

Refined Parameters Refined Parameters of Phase $Sr_3V_{1.8}Mo_{0.2}O_{8.1}$ from H004 at Room Temperature	
wR	**8.353**
GOF	**2.59**
Reduced chi2**	**28.01**
Space Group	**R-3 m h**
Unit Cell parameters	**a= 5.64377, c= 20.08223**

Appendix A3a. The Combined Refinement Results of H004($Sr_3V_{1.8}Mo_{0.2}O_8$) at Room Temperature

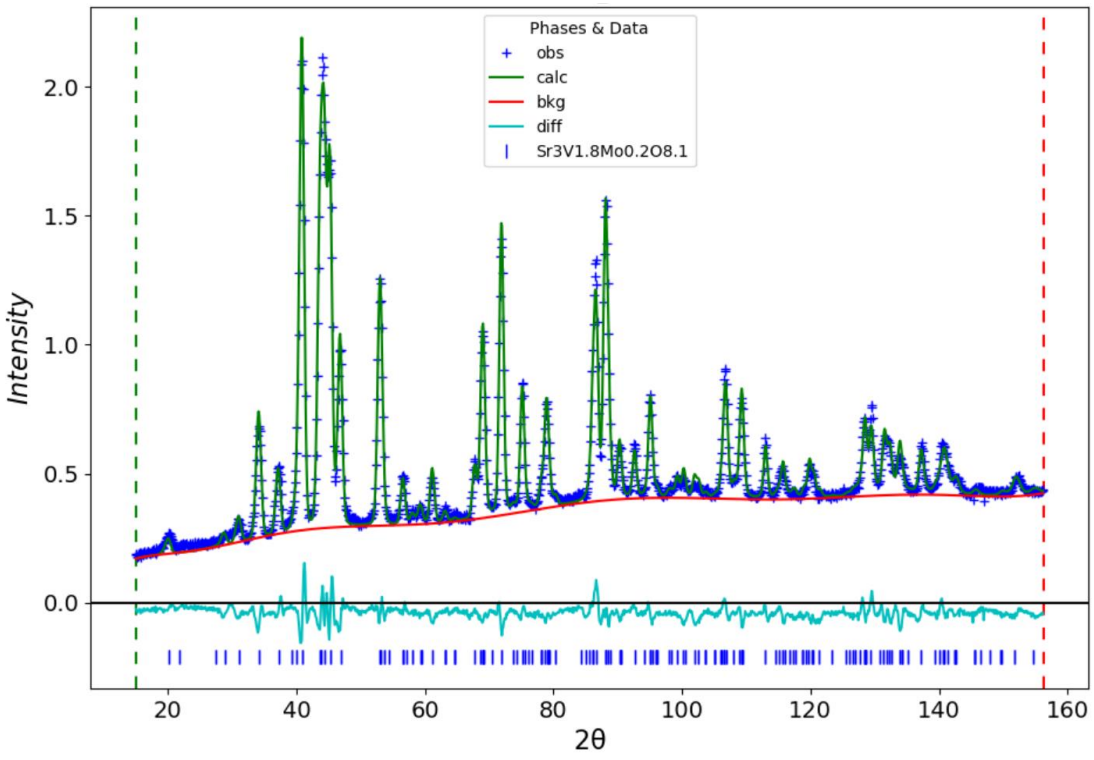

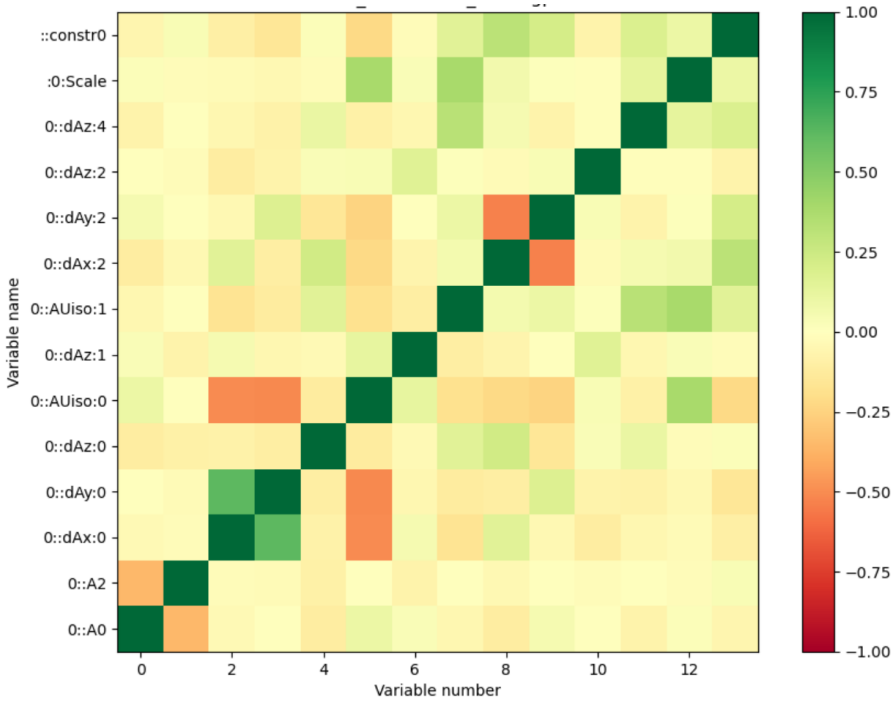

Refined Parameters Refined Parameters of Phase $Sr_3V_{1.8}Mo_{0.2}O_{8.1}$ from H004 at 780K	
wR	4.359
GOF	3.38
Reduced chi**2	11.42
Space Group	R-3 m h
Unit Cell parameters	a= 5.68599, c= 20.18697

Appendix A3b. The Neutron Refinement Results of H004($Sr_3V_{1.8}Mo_{0.2}O_8$) at 780K

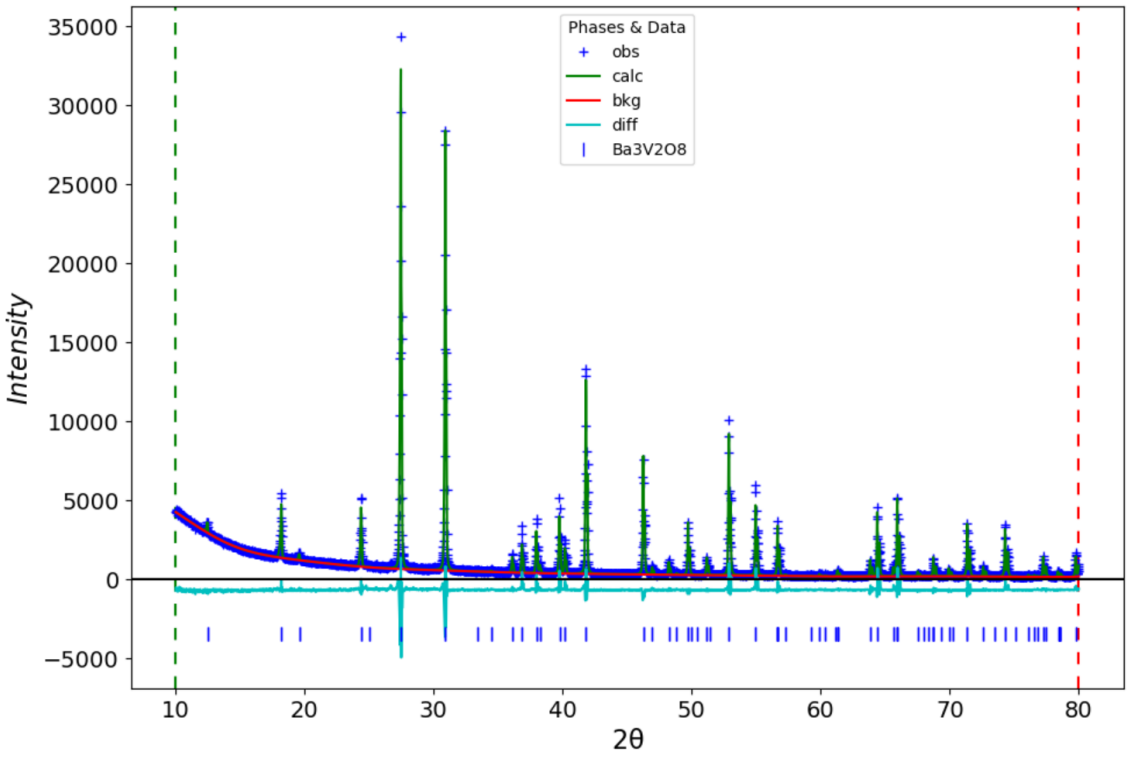

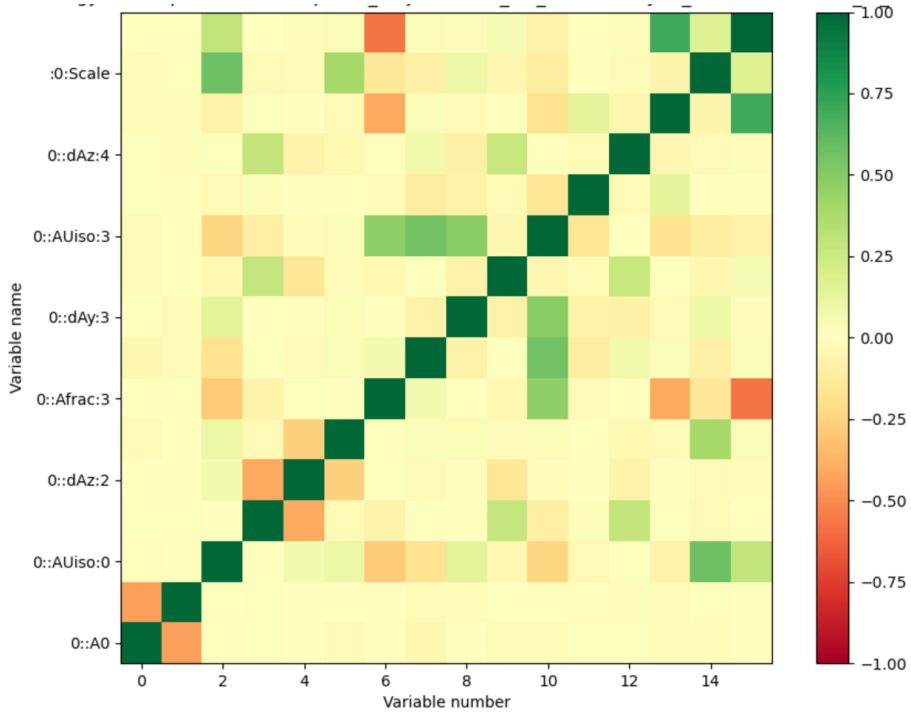

Refined Parameters Phase $Ba_3V_2O_8$ from H002 at Room Temperature	
wR	9.998
GOF	4.09
Reduced chi**2	16.74
Space Group	R-3 m
Unit Cell parameters	a= 5.78364, c= 21.32384

Appendix A4a. The Combined Refinement Results of H002($Ba_3V_2O_8$) at Room Temperature

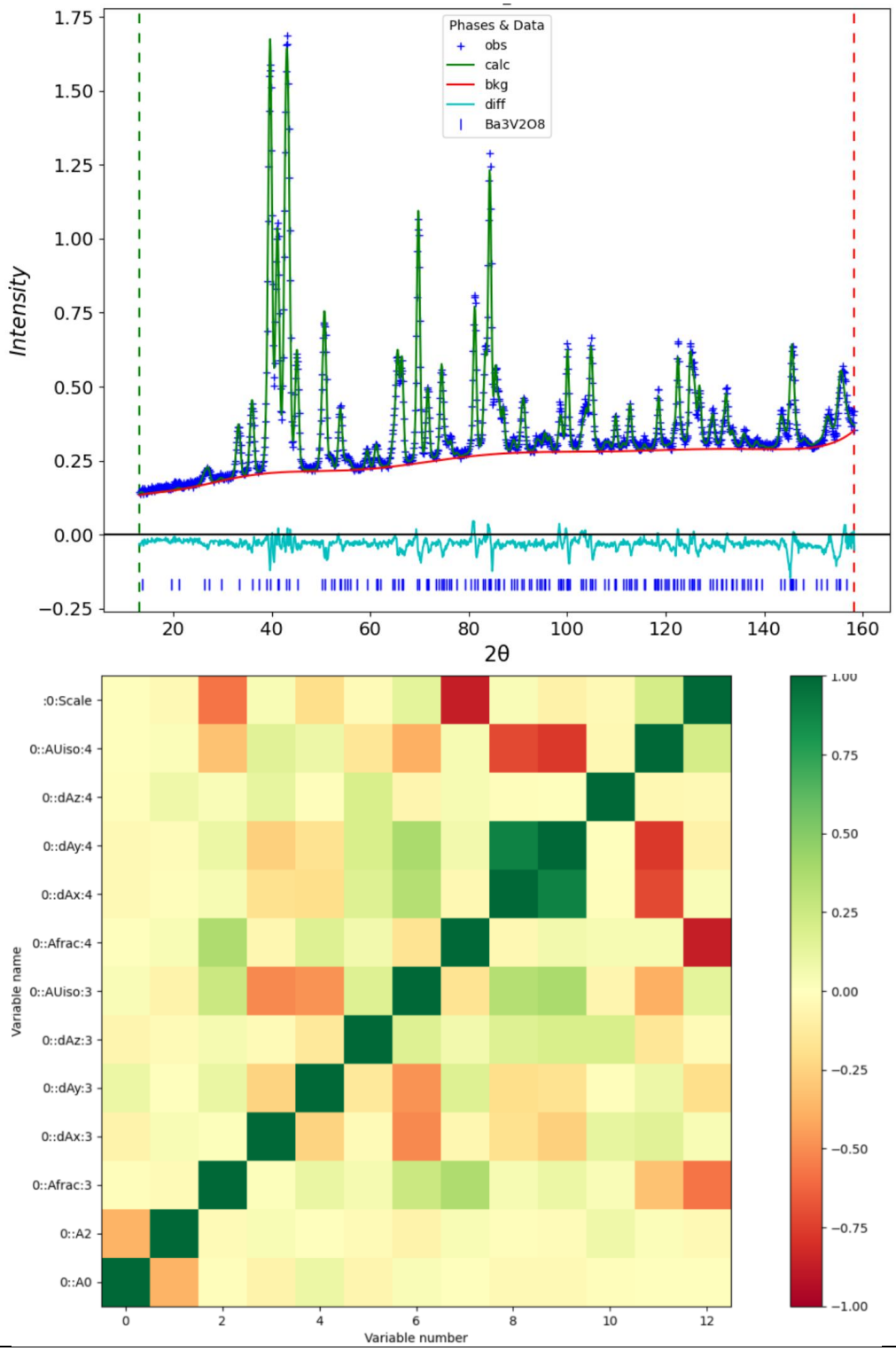

Refined Parameters Phase $Ba_3V_2O_8$ from H002 at 780K	
wR	4.953
GOF	2.91
Reduced chi**2	8.63
Space Group	R-3 m
Unit Cell parameters	a= 5.84337, c= 21.42281

Appendix A4b. The Neutron Refinement Results of H002($(Ba_3V_2O_8)$) at 780K

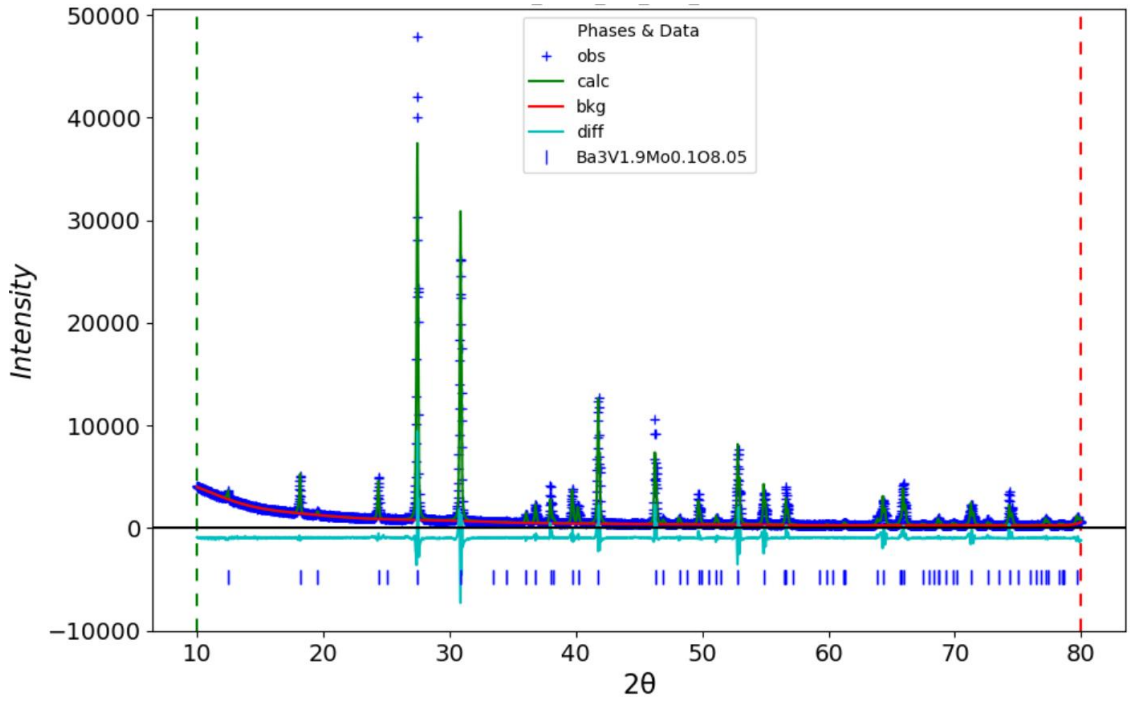

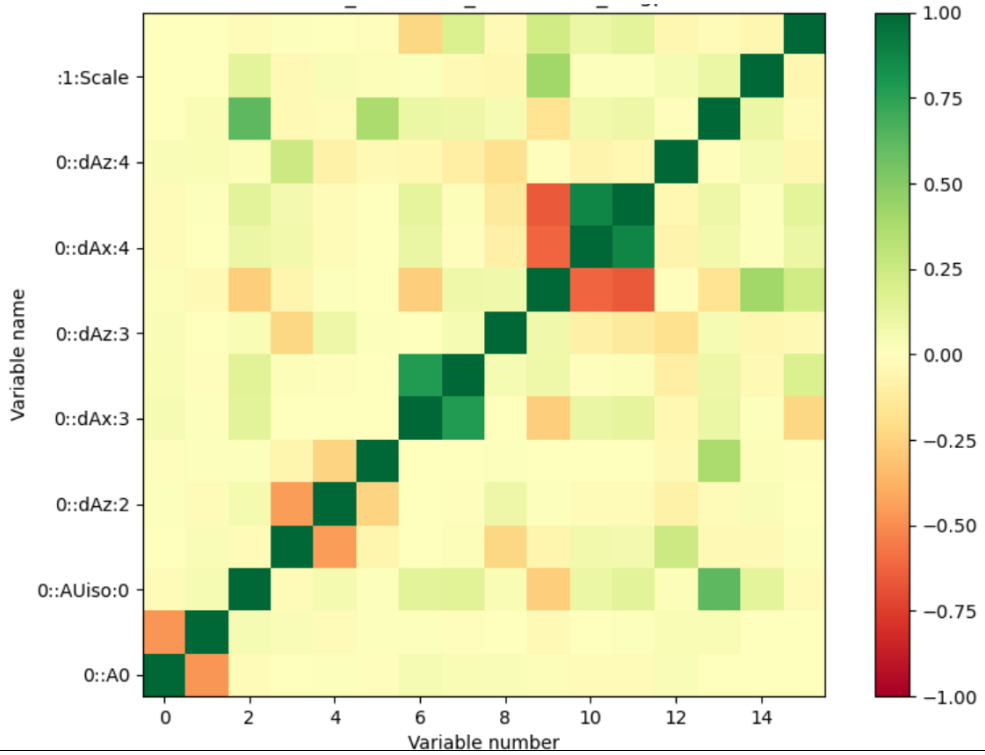

Refined Parameters Phase $Ba_3V_{1.9}Mo_{0.1}O_{8.05}$ from H009 at Room Temperature	
wR	**10.309**
GOF	**4.42**
Reduced chi2**	**19.54**
Space Group	**R-3 m**
Unit Cell parameters	**a= 5.79126, c= 21.31191**

Appendix A5a. The Combined Refinement Results of H009($Ba_3V_{1.9}Mo_{0.1}O_{8.05}$) at Room Temperature

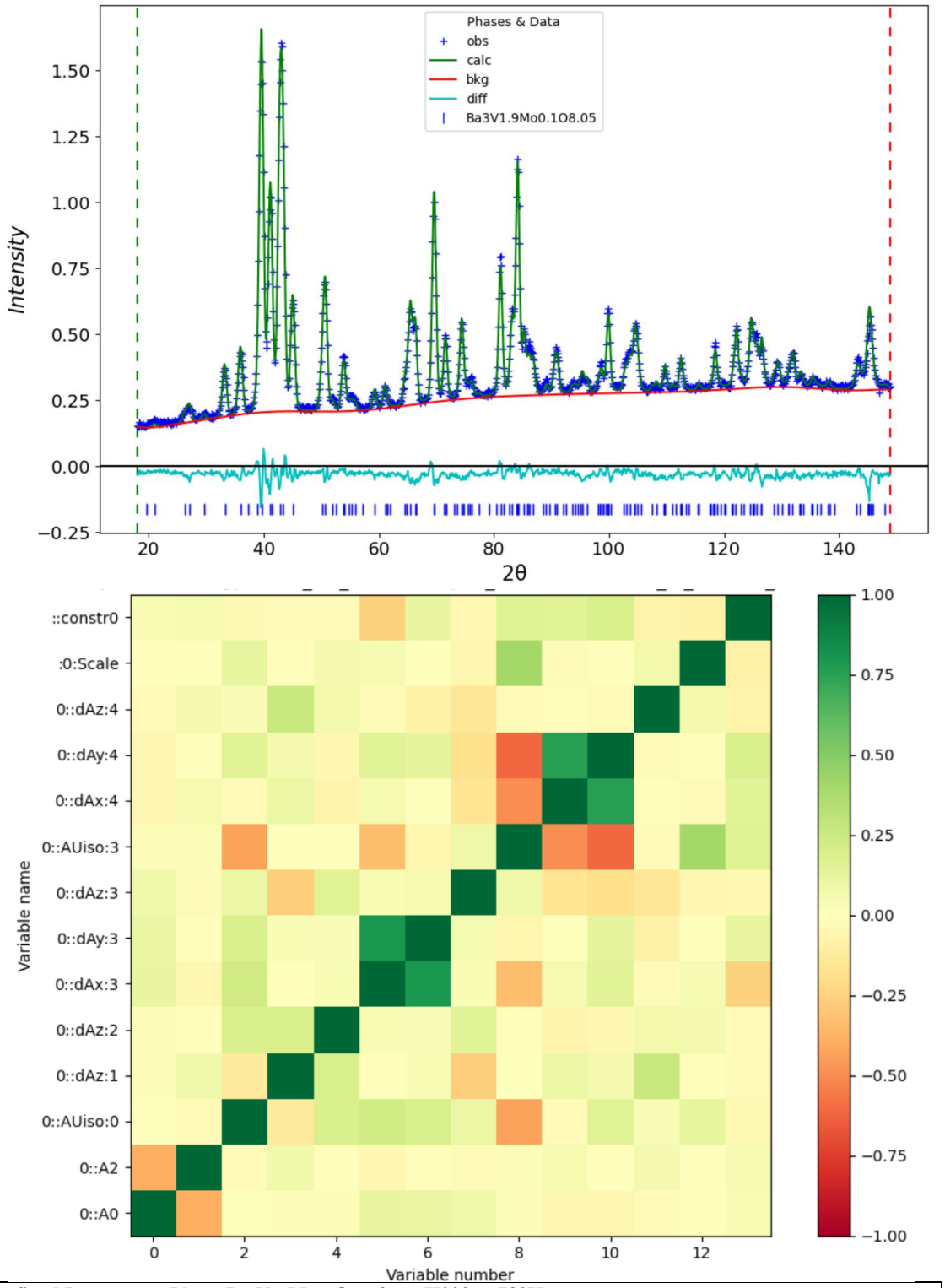

Refined Parameters Phase $Ba_3V_{1.9}Mo_{0.1}O_{8.05}$ from H009 at 780K	
wR	**4.087**
GOF	**2.68**
Reduced chi2**	**7.21**
Space Group	**R-3 m**
Unit Cell parameters	**a= 5.85012, c= 21.41635**

Appendix A5b. The Neutron Refinement Results of H009($Ba_3V_{1.9}Mo_{0.1}O_{8.05}$) at 780K

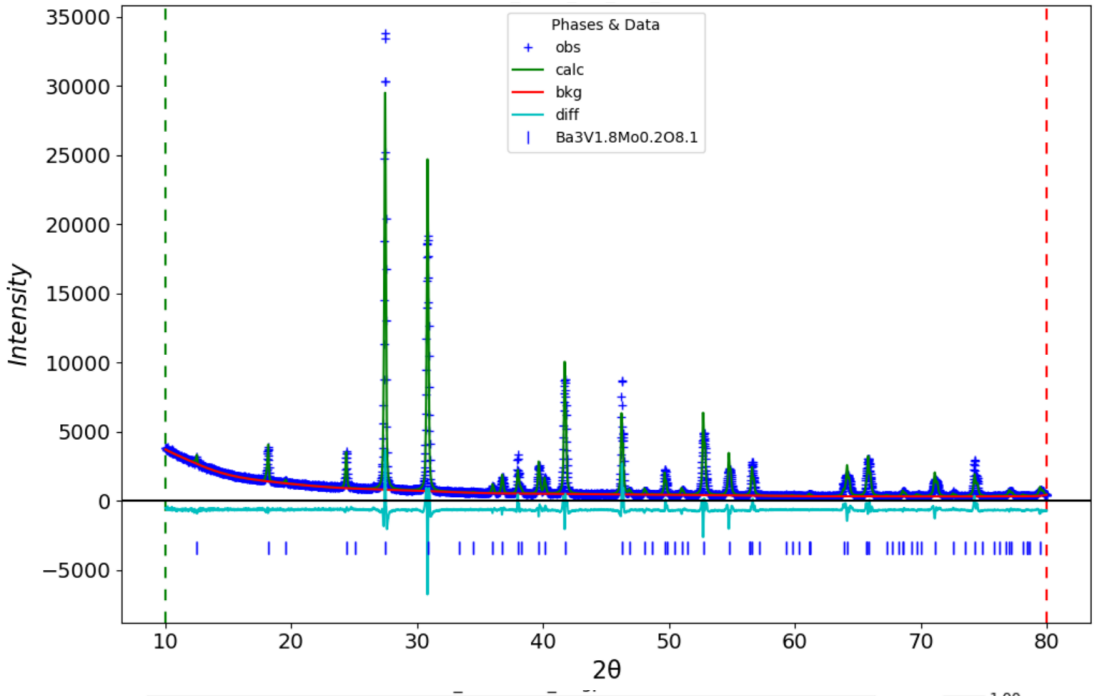

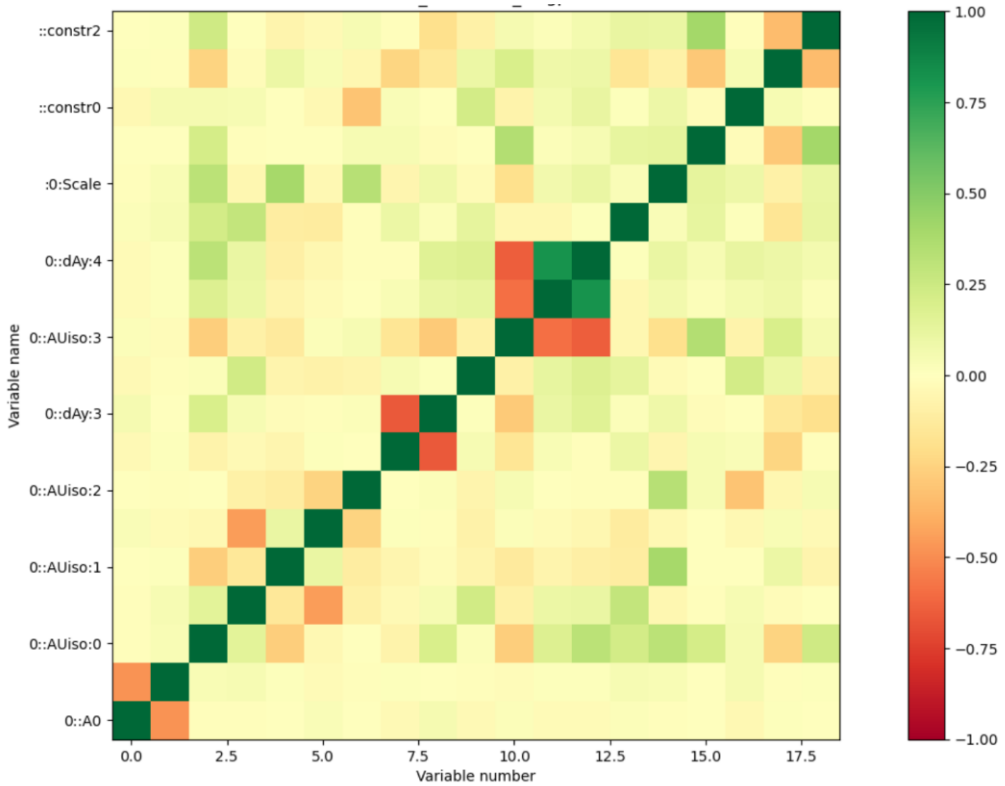

Refined Parameters Phase $Ba_3V_{1.8}Mo_{0.2}O_{8.1}$ from H010 at Room Temperature	
wR	**8.846**
GOF	**3.85**
Reduced chi2**	**14.80**
Space Group	**R-3 m**
Unit Cell parameters	**a= 5.80382, c= 21.2952**

Appendix A6a. The Combined Refinement Results of H010($Ba_3V_{1.8}Mo_{0.2}O_{8.1}$) at Room Temperature

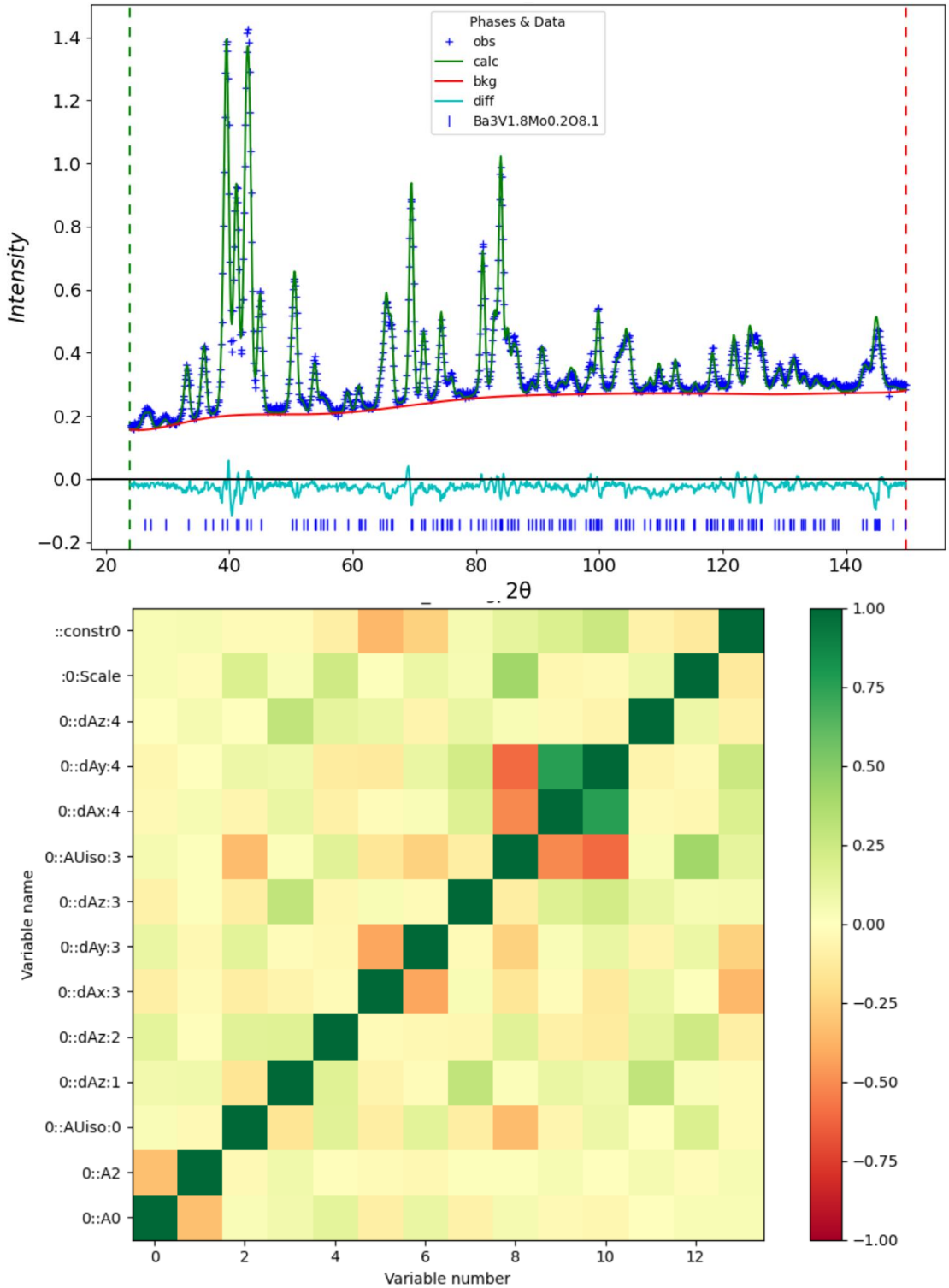

Refined Parameters Phase $Ba_3V_{1.8}Mo_{0.2}O_{8.1}$ from H010 at 780K	
wR	4.533
GOF	2.80
Reduced chi**2	7.85
Space Group	R-3 m
Unit Cell parameters	a= 5.86021, c= 21.41089

Appendix A6b. The Neutron Refinement Results of H010($Ba_3V_{1.8}Mo_{0.2}O_{8.1}$) at 780K

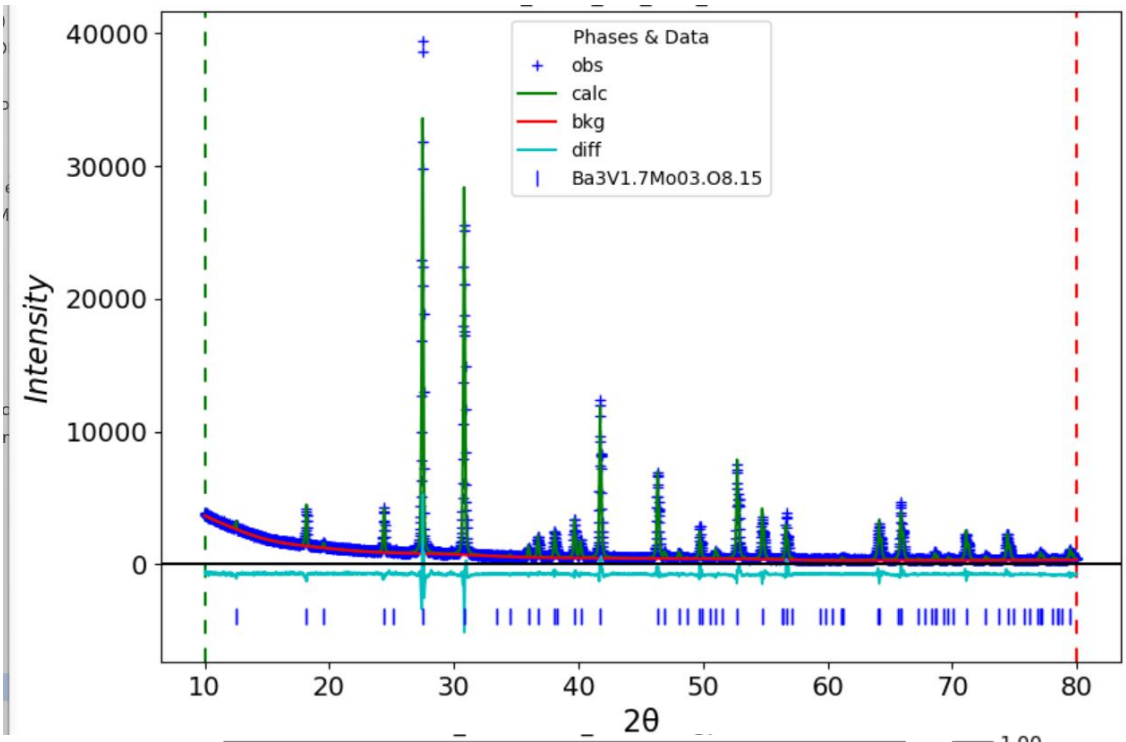

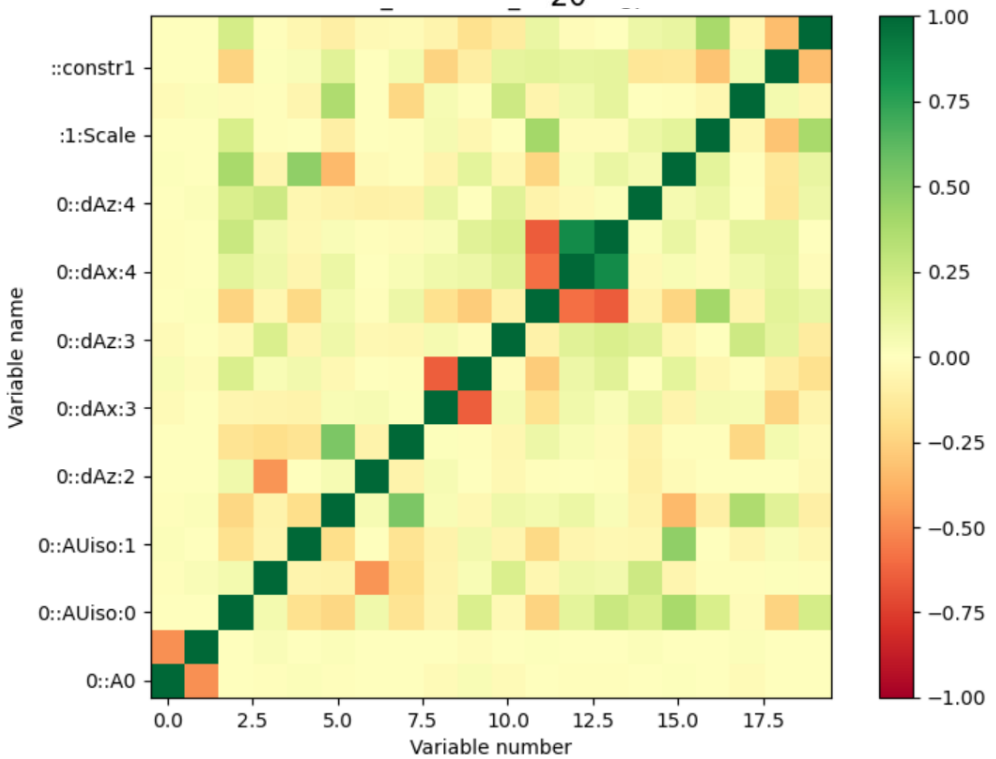

Refined Parameters Phase $Ba_3V_{1.7}Mo_{0.3}O_{8.15}$ from H011 at Room Temperature	
wR	8.618
GOF	3.47
Reduced chi**2	12.02
Space Group	R-3 m
Unit Cell parameters	a= 5.80734, c= 21.27681

Appendix A7a. The Combined Refinement Results of H011($Ba_3V_{1.7}Mo_{0.3}O_{8.15}$) at Room Temperature

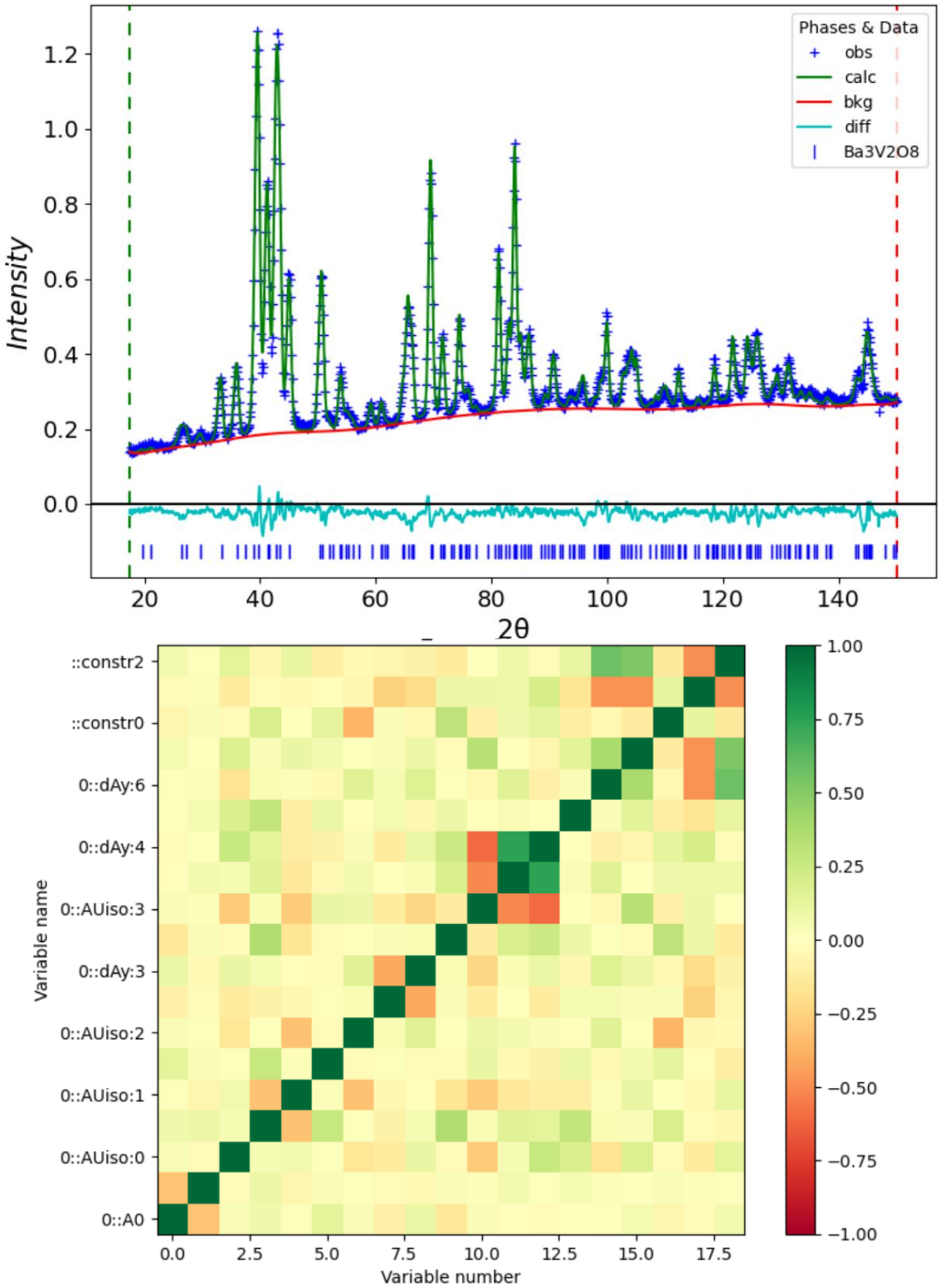

Refined Parameters Phase $Ba_3V_{1.7}Mo_{0.3}O_{8.15}$ from H011 at 780K	
wR	3.830
GOF	2.57
Reduced chi**2	6.58
Space Group	R-3 m
Unit Cell parameters	a= 5.86632, c= 21.40452

Appendix A7b. The Neutron Refinement Results of H0011($Ba_3V_{1.7}Mo_{0.3}O_{8.15}$) at 780K

Appendix B

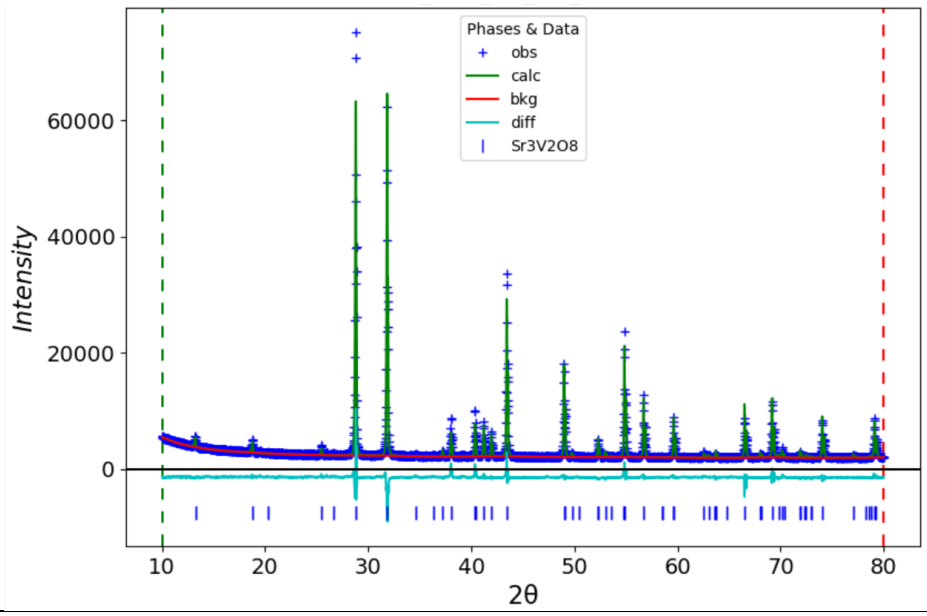

Phase $Sr_3V_2O_8$ from H019 at Room Temperature	
Space Group	**R-3 m h**
Unit Cell parameters	**a= 5.6204, c= 20.11327**

Appendix B1. The Le Bail Refinement Results of H019($Sr_3V_2O_8$) at Room Temperature

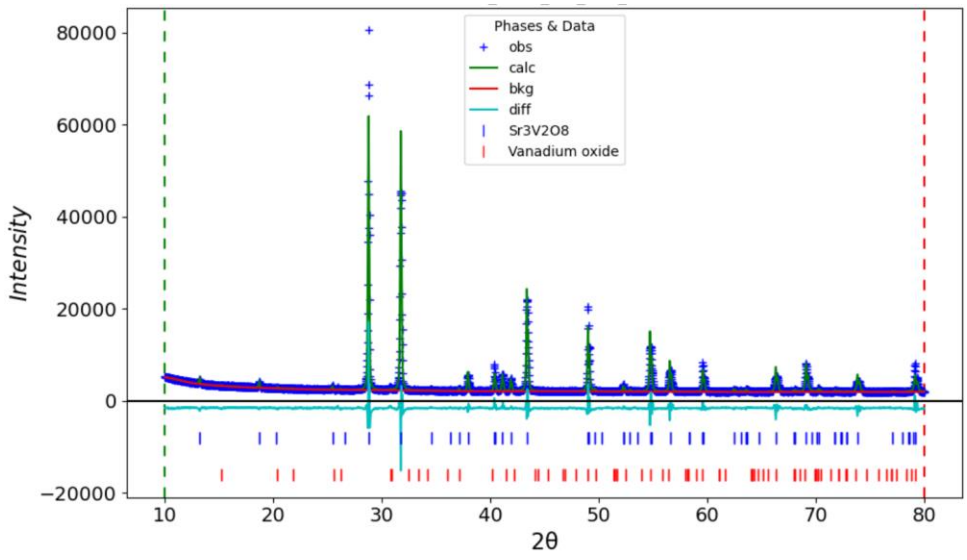

Phase $Sr_3V_2O_8$ from H020 at Room Temperature	
Space Group	**R-3 m h**
Unit Cell parameters	**a= 5.63582, c= 20.08327**

Appendix B2. The Le Bail Refinement Results of H020($Sr_3V_{1.9}Mo_{0.1}O_{8.05}$) at Room Temperature

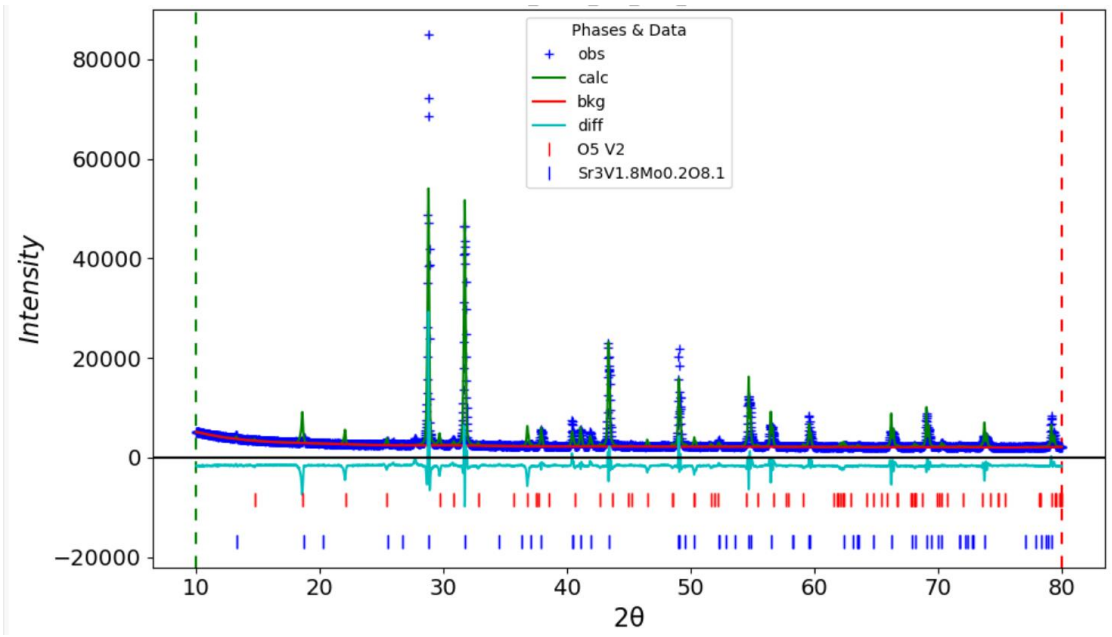

Phase $Sr_3V_2O_8$ from H021 at Room Temperature	
Space Group	**R-3 m h**
Unit Cell parameters	**a= 5.6435, c= 20.0805**

Appendix B3. The Le Bail Refinement Results of H021($Sr_3V_{1.8}Mo_{0.2}O_{8.1}$) at Room Temperature

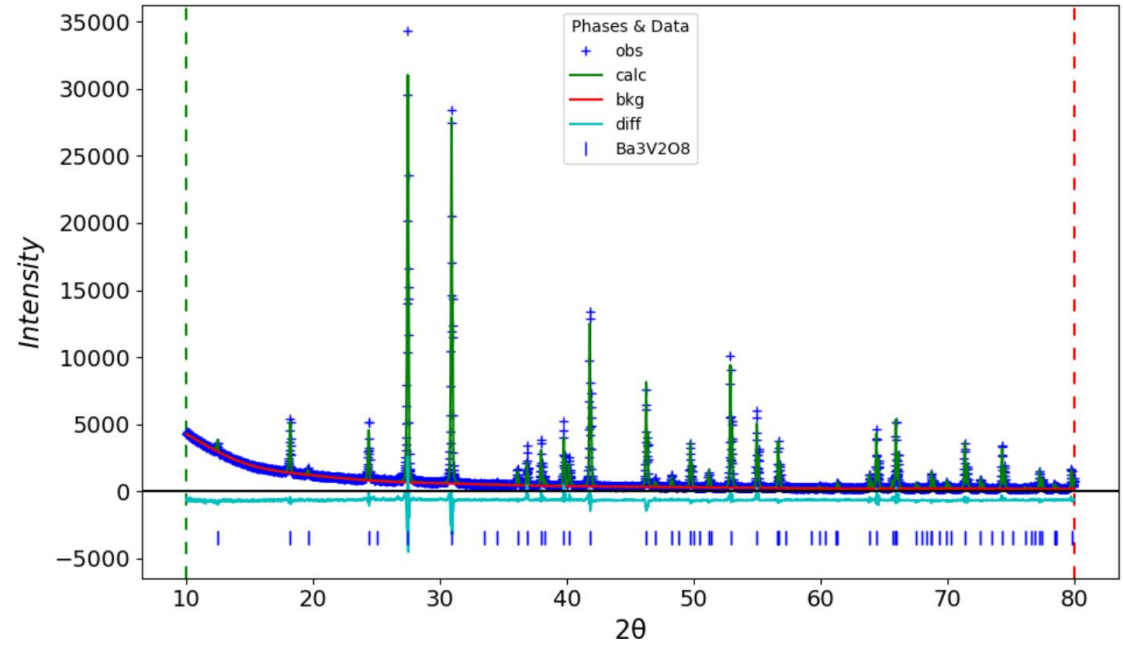

Phase $Ba_3V_2O_8$ from H015 at Room Temperature	
Space Group	R-3 m
Unit Cell parameters	a= 5.7742, c= 21.3327

Appendix B4. The Le Bail Refinement Results of H015($Ba_3V_2O_8$) at Room Temperature

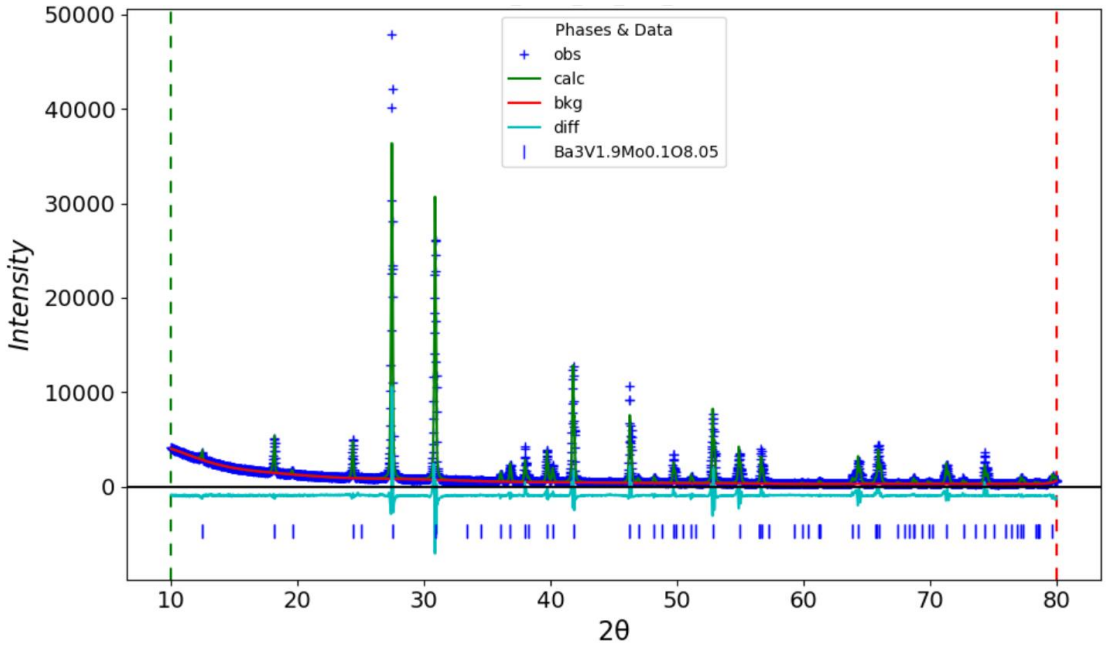

Phase $Ba_3V_2O_8$ from H016 at Room Temperature	
Space Group	R-3 m
Unit Cell parameters	a= 5.7841, c= 21.3241

Appendix B5. The Le Bail Refinement Results of H016($Ba_3V_{1.9}Mo_{0.1}O_{8.05}$) at Room Temperature

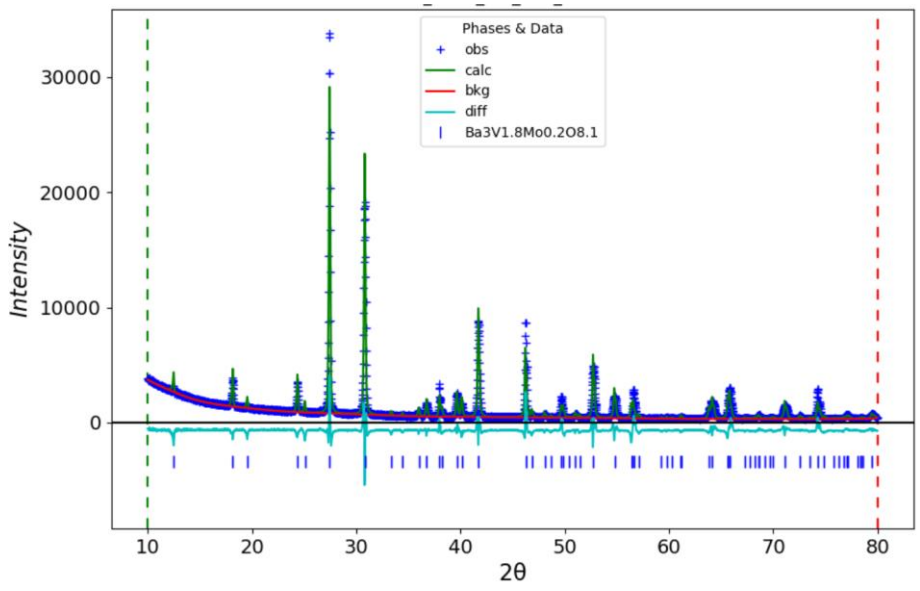

Phase $Ba_3V_2O_8$ from H017 at Room Temperature	
Space Group	R-3 m

Unit Cell parameters	a= 5.7991, c= 21.2921

Appendix B6. The Le Bail Refinement Results of H017($Ba_3V_{1.8}Mo_{0.2}O_{8.1}$) at Room Temperature

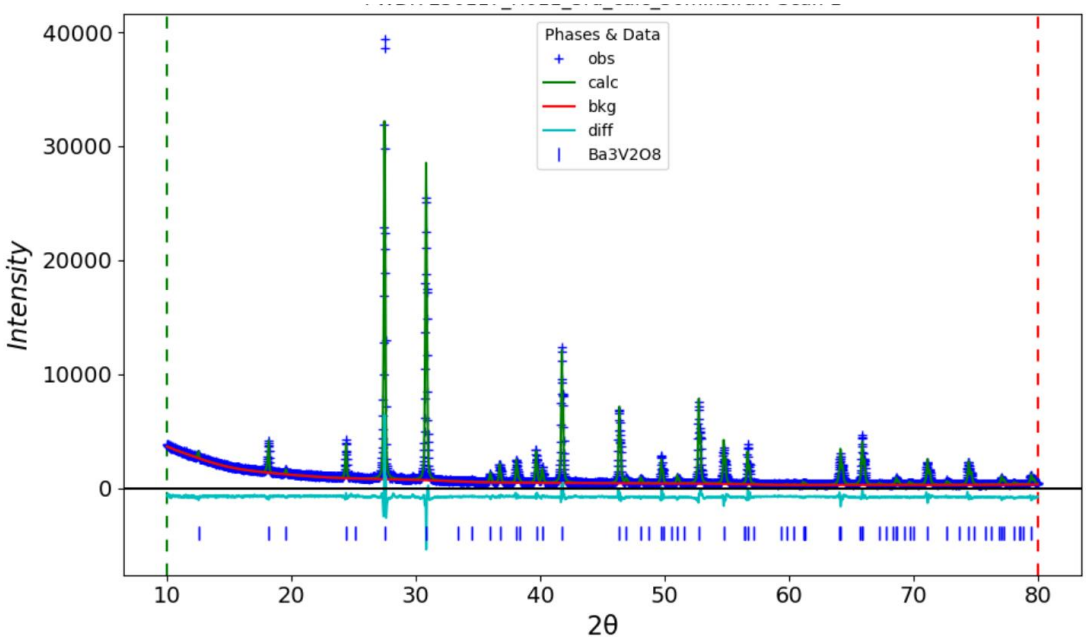

Phase $Ba_3V_2O_8$ from H018 at Room Temperature	
Space Group	R-3 m
Unit Cell parameters	a= 5.8051, c= 21.2835

Appendix B7. The Le Bail Refinement Results of H018($Ba_3V_{1.7}Mo_{0.3}O_{8.15}$) at Room Temperature